The e-TidalGCs Project

Modeling the extra-tidal features generated by Galactic globular clusters

Salvatore Ferrone[1], Paola Di Matteo[1], Alessandra Mastrobuono-Battisti[1], Misha Haywood [1], Owain N. Snaith[1], Marco Montuori[2], Sergey Khoperskov[3,1], David Valls-Gabaud[4]

1 GEPI, Observatoire de Paris, PSL Research University, CNRS, Place Jules Janssen, 92195 Meudon Cedex, France
  e-mail: `salvatore.ferrone@obspm.fr`
2 SMC-ISC-CNR and Dipartimento di Fisica, Sapienza University, P.le Aldo Moro 2, 00185, Rome, Italy
3 Leibniz-Institut für Astrophysik Potsdam (AIP), An der Sternwarte 16, 14482 Potsdam, Germany
4 LERMA, CNRS UMR 8122, Observatoire de Paris, PSL, 61 Avenue de l'Observatoire, 75014 Paris, France

ABSTRACT

We present the e-TidalGCs Project which aims at modeling and predicting the extra-tidal features surrounding all Galactic globular clusters for which 6D phase space information, masses and sizes are available (currently 159 globular clusters). We focus the analysis and presentation of the results on the distribution of extra-tidal material on the sky, and on the different structures found at different heliocentric distances. We emphasize the wide variety of morphologies found: beyond the canonical tidal tails, our models reveal that the extra-tidal features generated by globular clusters take a wide variety of shapes, from thin and elongated shapes, to thick, and complex halo-like structures. We also compare some of the most well studied stellar streams found around Galactic globular clusters to our model predictions, namely those associated to the clusters NGC 3201, NGC 4590, NGC 5466 and Pal 5. Additionally, we investigate how the distribution and extension in the sky of the simulated streams vary with the Galactic potential by making use of three different models, containing or not a central spheroid, or a stellar bar. Overall, our models predict that the mass lost by the current globular cluster population in the field from the last 5 Gyrs is between $0.3 - 2.1 \times 10^7 M_\odot$, an amount comparable between 7–55% of current mass. Most of this lost mass is found in the inner Galaxy, with the half-mass radius of this population being between 4–6 kpc. The outputs of the simulations will be publicly available, at a time when the ESA Gaia mission and complementary spectroscopic surveys are delivering exquisite data to which these models can be compared.

Key words. Galaxy: structure; Galaxy: kinematics and dynamics; (Galaxy:) globular clusters: general; Galaxy: evolution; Methods: numerical

1. Introduction

Globular clusters are the oldest, gravitationally-bound stellar systems in the Galaxy (Meylan & Heggie 1997). About 170 are currently known in the Milky Way (Vasiliev & Baumgardt 2021), and this census is possibly still incomplete, especially in the inner regions of the bulge and disk of our Galaxy, where dust extinction and high stellar number density limit detections. It is indeed in these regions that new globular cluster candidates have been recently discovered, thanks in particular to the analysis of near-infrared surveys (Minniti et al. 2011; Moni Bidin et al. 2011; Minniti et al. 2017a,b, 2018; Gran et al. 2019; Garro et al. 2020; Garro et al. 2022a,b; Garro et al. 2021; Minniti et al. 2021b,a; Gran et al. 2022). The current population of globular clusters possibly represents only the left-over of an initially more numerous and more massive one, depopulated by many disruptive processes (Gnedin & Ostriker 1997; Murali & Weinberg 1997a,b; Vesperini & Heggie 1997; Fall & Zhang 2001). One of the main processes affecting the globular cluster population, its evolution in number, mass and size, is tidal stripping.

As all stellar systems having a finite size and orbiting the Galaxy, globular clusters are subject to tidal effects, which arise because the opposite sides of these systems experience a different gravitational acceleration. The long-term effect of this process strips the system of its most loosely-bound stars, which

redistribute themselves onto orbits similar to that of their progenitor, forming so-called "tidal tails" or streams around it (see Grillmair et al. 1995; Leon et al. 2000, for some of the earliest studies). Some spectacular tails have been discovered and studied over the past twenty years around Milky Way globular clusters: from the roughly 30° degree long tails departing from the Palomar 5 cluster (Odenkirchen et al. 2001, 2003; Grillmair & Dionatos 2006a; Odenkirchen et al. 2009; Thomas et al. 2016; Starkman et al. 2020; Ibata et al. 2021) to those of NGC 5466 (Belokurov et al. 2006), Palomar 14 (Sollima et al. 2011) and to the GD-1 stream, whose parent cluster has still to be discovered (or it has been already completely destroyed, and the stream is the only vestige of its past existence, see Grillmair & Dionatos 2006b; Webb & Bovy 2019; Bonaca et al. 2020a). These studies have been boosted in the last few years thanks to the publication of the ESA Gaia mission catalogues (Gaia Collaboration et al. 2016, 2018, 2021a,b) which—by delivering parallaxes, proper motions and magnitudes for about 1.4 billion stars, and radial velocity for several million—is allowing for searches of stars with coherent distances and motions in the Galaxy, revealing the existence of a number of new and spectacular streams, as well as rediscovering already known ones (Navarrete et al. 2017; Malhan et al. 2018b,a; Ibata et al. 2018; Piatti 2018; Shipp et al. 2018; Ibata et al. 2019a,b; Kaderali et al. 2019; Bianchini

et al. 2019; Malhan et al. 2019; Malhan & Ibata 2019; Palau & Miralda-Escudé 2019; Piatti & Carballo-Bello 2019; Caldwell et al. 2020; Ibata et al. 2020; Piatti & Fernández-Trincado 2020; Piatti & Carballo-Bello 2020; Piatti et al. 2020; Shipp et al. 2020; Thomas et al. 2020; Boldrini & Vitral 2021; Ibata et al. 2021; Malhan et al. 2021; Jensen et al. 2021; Palau & Miralda-Escudé 2021; Piatti et al. 2021; Piatti 2021; Yuan et al. 2022; Zhang et al. 2022; Nie et al. 2022; Piatti 2022). Mateu (2022) provides a recent compilation of known stellar streams.

All these studies are unraveling a very complex and rich set of stellar structures in the Milky Way, mainly distributed in the halo, where their identification is the easiest because of the low density of the background stellar field.

From the numerical and theoretical point of view, many studies have been focused over the years on the formation and evolution of tidal streams around globular clusters (Keenan & Innanen 1975; Oh & Lin 1992; Oh et al. 1992; Grillmair 1998; Combes et al. 1999; Ibata et al. 2002; Johnston et al. 2002; Yim & Lee 2002; Capuzzo Dolcetta et al. 2005; Di Matteo et al. 2005; Montuori et al. 2007; Siegal-Gaskins & Valluri 2008; Küpper et al. 2010; Lane et al. 2010; Küpper et al. 2012; Mastrobuono-Battisti et al. 2012; Sanders & Binney 2013; Bovy 2014; Amorisco et al. 2016; Erkal et al. 2016; Sanders et al. 2016; Pearson et al. 2017; Carlberg 2018; Thomas et al. 2018; Carlberg 2020; Vitral & Boldrini 2022). These studies have contributed to understanding how these structures form and evolve, to what extent they trace the globular cluster orbit and how their shape, extension and morphology depend on the orbital phase, characteristics of the Galactic potential or on the tidal shocks experienced by the cluster itself when it crosses the Galactic disk.

Some works have presented models and simulations for specific streams (Dehnen et al. 2004; Mastrobuono-Battisti et al. 2012; Banik & Bovy 2019; Bonaca et al. 2019; Banik et al. 2021a; Mirabal & Bonaca 2021), contributing to understanding their morphology, density variations and extent. From these works, it is clear that the tidal loss of stars from globular clusters and the formation of related structures are important for several aspects: (1) quantifying to what extent globular clusters have contributed to the field stellar populations—from the halo to the disk to the bulge—and to what extent they still do, (2) reconstructing the properties (in terms of numbers and masses) of the early Galactic globular clusters, through their current mass loss, and, last but not least, (3) using globular cluster streams as a probe of the Galactic potential and—more generally—of the physical laws governing gravity (see for example Thomas et al. 2018; Bianchini et al. 2019; Naik et al. 2020; Banik et al. 2021a,b).

In this paper, we wish to contribute to the current studies on this matter by presenting the first complete catalogue of simulated extra-tidal features around globular clusters. We emphasize that we talk generically about features and not specifically about tails, or streams, because the latter are but one of the morphologies that extra-tidal material can reveal, as we will show. This project is motivated, on the one hand, by the aforementioned discoveries of many numerous new streams and tails in the Galaxy, and on the other hand, by the availability of the full 6D phase information and internal parameters (masses and sizes) for more than 150 Galactic globular clusters (Baumgardt & Hilker 2018; Baumgardt & Vasiliev 2021; Vasiliev & Baumgardt 2021). The aims of this project are manyfold: (1) to have a complete view of the expected distribution of globular clusters tidal structures in the sky; (2) to help the interpretation of recent and future discoveries; (3) to support the search for new extra-tidal features in the data; (4) to offer the community a repository of all these models

to be compared to other theoretical and numerical predictions, which adopt different Galactic potentials and/or gravity laws.

2. Numerical method

To model the formation and evolution of extra-tidal features around Galactic globular clusters, we use a set of codes, called GCsTT (Globular Clusters' Tidal Tails), developed by our group. GCsTT comprises two python codes, for the backward and forward integration of a stellar system, made of N test-particles (see Sect. 2.1). These codes are separated for data organization and management, the computationally most expensive part—the calculation of the accelerations acting on the N particles and the orbits integration—is realized by means of a Fortran module written by our group. This module is interfaced to python by means of f2py directives from NumPy. The use of test-particle methods for modeling the tidal stripping process is widespread in the literature, where these methods are usually applied to one or few clusters at a time (see, for example, Lane et al. 2012; Mastrobuono-Battisti et al. 2012; Palau & Miralda-Escudé 2019; Piatti et al. 2021; Grillmair 2022). In this work, we apply a test-particle methodology to the whole set (159) of Galactic globular clusters for which this is currently possible, taking also into account, for each cluster, errors on astrometry, line-of-sight velocities[1] and distances. In the following of this section, we describe the two main steps of the procedure used by GCsTT to simulate the tidal stripping process (Sect. 2.1), the initial conditions adopted for the clusters' parameters and their mass distribution (Sect. 2.2), as well as the Galactic potentials (Sect. 2.3).

2.1. Simulations of the tidal stripping process: a two-step procedure

To model the formation and evolution of extra-tidal features around Galactic globular clusters, and predict their current properties, we proceed as follows:

(i) *Backward integration—Reconstructing the globular cluster orbit in the last 5 Gyr.*
First, for each Galactic globular cluster for which distances from the Sun, proper motions, line-of-sight velocities, and structural parameters are available (see Sect. 2.2), we determine their current positions and velocities in a Galactocentric reference frame, in which the Sun is at $(x_\odot, y_\odot, z_\odot) = (-8.34, 0., 0.027)$ kpc (Chen et al. 2001; Reid et al. 2014), a velocity for the local standard of rest, $v_{LSR} = 240$ km/s (Reid et al. 2014), and a peculiar velocity of the Sun with respect to the LSR, $(U_\odot, V_\odot, W_\odot) = (11.1, 12.24, 7.25)$ km/s (Schönrich et al. 2010). We then integrate the orbit of a single point mass, representing the cluster barycenter, backwards in time for 5 Gyr, and in this way we retrieve its position and velocity at that time in the chosen Galactic potential (see Sect. 2.3). We notice that other choices for the Sun's position or velocity with respect to the Galactocentric frame would have been possible. For example, Piatti et al. (2021) adopt the same values as ours for the

---

[1] Note that the term "line-of-sight velocities" adopted in this paper corresponds to the term "radial velocities" often used in the literature, as well as in the Gaia catalogues. We prefer the use of the first term, since the second is usually used also to indicate the (Galactocentric) radial velocities and can induce to some ambiguity, especially when different coordinate systems are used. We emphasize that the choice to use the term "line-of-sight velocity" is not new (see, for example Vasiliev & Baumgardt 2021).

v_{LSR} and for the peculiar velocity of the Sun, but a different distance to the Galactic center (8.1 kpc in their work, see GRAVITY Collaboration et al. 2018). The difference in the adopted position of the Sun is, however, in general smaller than the uncertainties affecting our knowledge of the distance of Galactic globular clusters to the Sun. For this reason we do not to explore the dependency of the results presented in this paper on these choices.

(ii) *Forward integration—Test-particle streams from the past to the present day.*

Once the positions and velocities of the barycenter of each cluster, 5 Gyr ago, are determined, we build the corresponding N-body system, with N = 100 000 particles. The phase-space coordinates of these particles are generated following a Plummer distribution, with total mass and half-mass radius as described in Sect. 2.2. The barycenter of this N-body cluster is then assigned initial positions and velocities in the Galactic model, as those retrieved at step (i) and the cluster is then integrated forward in time, until the present day. Particles in this N-body system are modeled as test-particles, that is they experience the gravitational field exerted by the globular cluster itself (see Sect. 2.2) and by the Galaxy (see Sect. 2.3), but not generate any gravitational field themselves. This allows us to maintain a computational time which scales as $O(N)$ and not as $O(N^2)$, as it would be the case for a direct N-body self-consistent computation.

In the following, we refer to these simulations, made by using the most probable values on distances, proper motions and line-of-sight velocities, as the "reference simulations". In addition, for each globular cluster, we also take into account the errors on its distance, proper motions, and line-of-sight velocity, assuming Gaussian distributions of the errors, treated as independent, and by generating 50 random realizations of these parameters. For each of these realizations, we repeat the steps described above, that is: (i) we determine the associated current positions and velocities in the chosen Galactocentric reference frame, we integrate the orbit of the single-point mass (representing the cluster barycenter) backwards in time, retrieving the corresponding values 5 Gyr ago, (ii) we build a N-body cluster containing N= 100 000 particles, with total mass and half-mass radius as those used for the reference simulation, and then we integrate the N-body cluster forwards in time until the present day position.

To summarize, for a given Galactic potential, we run 159 × (50 + 1) = 8109 simulations, where 159 is the total number of clusters for which we currently have both 6D phase-space information and structural parameters. As we will discuss in the following section, the whole set of globular clusters has been evolved in three different Galactic potentials, which implies that a total of 24 327 simulations has been run.

For the orbit integration, a leap-frog algorithm is used, with a fixed time-step, Δt, and a total number of steps, N_{steps}, such that the total simulated time is $\Delta t \times N_{steps}$ = 5 Gyr. The choice of the value of Δt adopted to simulate each cluster in the Galactic potential has been based on the energy conservation of the corresponding cluster evolved in isolation (that is without the effect of the Galactic gravitational field for 5 Gyr). For the majority of the clusters (109/159) this value has been set to $\Delta t = 10^5$ yr (for a corresponding value of $N_{steps} = 50\,000$), for the remaining clusters (50/159) a $\Delta t = 10^4$ yr (for a corresponding value of $N_{steps} = 500\,000$) has been used. We refer the reader to Appendix B, and in particular to Table B.1, for additional details

on the choice of Δt for the whole set of clusters. As for the total simulated time, while globular clusters are much older than 5 Gyr, we chose this time limit because the longer back in time we could go, the less certain we would be of the Galactic environment. In addition, the last significant mergers in the Galaxy happened between 9 and 11 Gyr ago (see Belokurov et al. 2018; Helmi et al. 2018; Di Matteo et al. 2019; Gallart et al. 2019; Kruijssen et al. 2020), thus well before the time interval simulated in this study. Other more recent interactions, such as the accretion of Sagittarius and of the Magellanic Clouds, may perturb the Galactic potential as well (see, for example, Vasiliev et al. 2021) and we plan to investigate their impact on the properties of globular cluster streams in the future.

For each realization, we generate an output file in an hdf5 format[2] containing right ascension (α), declination (δ), distance from the Sun (D); the components for proper motion in the equatorial coordinate system ($\mu_\alpha \cos(\delta)$ and μ_δ), the line-of-sight velocity ($v_{\ell os}$), longitude (ℓ), latitude (b); the components for proper motion in the Galactic coordinate system ($\mu_\ell \cos(b)$ and μ_b), and the Galactocentric positions (x, y, z), velocities (v_x, v_y, v_z) and energy, E, of each particle in the simulated system. We used Astropy (Astropy Collaboration et al. 2013, 2018) to convert the Galactocentric positions and velocities in the equatorial and Galactic quantities $\alpha, \delta, D, \mu_\alpha \cos(\delta), \mu_\delta, v_{\ell os}, \ell, b, \mu_\ell \cos(b)$ and μ_b.

For each particle, we also save its escape time t_{esc}, defined as the time at which the particle escapes from the cluster, that is the time t at which the particle satisfies the relation[3]:

$$E_{GC} = 0.5 \times \left((v_x - v_{x,GC})^2 + (v_y - v_{y,GC})^2 + (v_z - v_{z,GC})^2 \right) + \Phi_{GC} > 0$$

(1)

E_{GC} being the total specific energy of the particle relative to the cluster, that is the sum of the potential energy, Φ_{GC}, due to the gravitational field of the cluster (see Eq. 2), and of the kinetic energy, relative to the cluster barycenter, $T_{GC} = 0.5 \times \left((v_x - v_{x,GC})^2 + (v_y - v_{y,GC})^2 + (v_z - v_{z,GC})^2 \right)$, where $v_x, v_y,$ and v_z are its velocity components at time t, and $v_{x,GC}, v_{y,GC}$ and $v_{z,GC}$ those of the cluster barycenter at the same time. A positive value of E_{GC} implies that the particle is no longer gravitationally bound to the cluster, and hence it is lost in the field.

Overall, the total volume of the whole set of 24 327 simulations, saved in hdf5 format, amounts to about 370 Gb.

2.2. Simulations of the tidal stripping process: Globular clusters' current and initial conditions and their gravitational potential

To be executed, steps (i) and (ii) described in the previous section require some input conditions. The current distances from the Sun, proper motions, and line-of-sight velocities, and the related uncertainties, of all 159 globular clusters considered in this study are taken respectively from Baumgardt & Vasiliev (2021) and Vasiliev & Baumgardt (2021). These values are then converted into Galactocentric positions and velocities by making use of Astropy, and used as initial conditions to execute step (i).

---

[2] https://www.hdfgroup.org/solutions/hdf5/
[3] If the particle is gravitationally bound to the cluster until the end of the simulation, t_{esc} is set equal to −9999.

Step (*ii*) requires generating an *N*-body system, representing the globular cluster, whose initial total mass and half-mass radius are assigned on the basis of their current values, as given by Baumgardt & Hilker (2018)[4] and reported in Table A.1. As anticipated at step (*ii*) in Sect. 2.1, the phase-space coordinates of each *N*-body cluster are generated by assuming a Plummer distribution of total mass M_{GC} and half-mass radius r_h, for which the corresponding potential is:

$$\Phi_{GC}(r) = -\frac{GM_{GC}}{\sqrt{r^2 + r_c^2}}, \tag{2}$$

where r_c is the cluster scale radius, and is related to the half-mass radius r_h through $r_h \simeq 1.305 r_c$ (Heggie & Hut 2003). The variable r here indicates the distance of the test particle from the center of the cluster. For each cluster, the same Plummer distribution used to generate the *N*-body system is also used to calculate the accelerations exerted on each particle as the system moves through time. The Plummer sphere, representing the cluster potential, moves indeed through the Galaxy along the orbit retrieved at step (i), traveling this time in the opposite direction, from 5 Gyr ago to the present day.

The reader might note that this implies that the globular cluster density profile and its internal parameters (total mass and characteristic radius) are constant in time in these models. This is of course a crude approximation, because in reality both the internal parameters and the density profile itself can change over time. We consider these assumptions to be acceptable within the scope of our work given that we are primarily interested in the distribution of extra-tidal stars, which once escaped from the cluster have dynamics primarily dictated by the Galactic potential rather than the globular cluster itself. Of course, the density of stars along the extra-tidal structures, as well as the total mass lost, depend on these assumptions (that is, if the mass of the cluster was not assumed constant in time, but could decrease, the gravitational attraction exerted by the cluster itself on its stars would be weaker, and this would lead to an increasing mass loss and density along the tails). We could have proceeded diminishing the mass over time, based on some assumptions on the temporal behavior of this relation, but we did not find this approach satisfying. In this way we would have taken into account a temporal evolution of the mass, but not of the size of the cluster, adding supplementary hypothesis to the problem. For these reasons, we decided to maintain the simplest approach. We emphasize that other groups followed the same methodology, maintaining masses and sizes constant with time (see, for example, Palau & Miralda-Escudé 2019).

The summary tables giving both the current internal parameters of the clusters (total mass and half-mass radius), their astrometric quantities of relevance for this study and the line-of-sight velocities are publicly available[5]. We have made use of these tables for our work, and we report them in a unique table in our paper for completeness and self-consistency of the data used (see Table A.1).

2.3. Simulations of the tidal stripping process: Galactic potentials

As for the Galactic mass distribution, we make use of the two axisymmetric Galactic mass models presented in Pouliasis et al. (2017), and of an asymmetric mass model, containing a central stellar bar, that we present here for the first time. We recall below the main properties of the two models of Pouliasis et al. (2017), and we describe in more detail the asymmetric Galactic mass model, which is presented here for the first time.

2.3.1. Model I by Pouliasis et al. (2017): an axisymmetric mass model for the Galaxy including a spherical bulge

Model I by Pouliasis et al. (2017) (abbreviated name: PI) consists of four components: two disks (thin and thick) both described by Miyamoto & Nagai potentials, a dark matter halo, and a central bulge. Its total potential is:

$$\Phi_{tot}(R, z) = \Phi_{thin}(R, z) + \Phi_{thick}(R, z) + \Phi_{halo}(r) + \Phi_{bulge}(r) \tag{3}$$

with $r = \sqrt{R^2 + z^2}$,

$$\Phi_{thin}(R, z) = \frac{-GM_{thin}}{\left(R^2 + \left[a_{thin} + \sqrt{z^2 + b_{thin}^2}\right]^2\right)^{1/2}} \tag{4}$$

$$\Phi_{thick}(R, z) = \frac{-GM_{thick}}{\left(R^2 + \left[a_{thick} + \sqrt{z^2 + b_{thick}^2}\right]^2\right)^{1/2}} \tag{5}$$

$$\Phi_{halo}(r) = \frac{-GM_{halo}}{r} - \frac{M_{halo}}{1.02 a_{halo}} \times$$
$$\left[\frac{-1.02}{1 + \left(\frac{r}{a_{halo}}\right)^{1.02}} + ln(1 + \left(\frac{r}{a_{halo}}\right)^{1.02})\right]_R^{100}, \tag{6}$$

and

$$\Phi_{bulge}(r) = -\frac{GM_{bulge}}{\sqrt{r^2 + b_{bulge}^2}}, \tag{7}$$

where $M_{thin}, M_{thick}, M_{halo}$, and M_{bulge} are the masses of the disks, halo and bulge and: $a_{thin}, b_{thin}, a_{thick}, b_{thick}, a_{halo}, b_{bulge}$ are the characteristic scale lengths of the thin and thick disks, the halo and the central bulge, respectively (see Table 1).

This model is a modification of the classical Allen & Santillan (1991) model, made to include also the presence of a thick disk. As it has been discussed in detail by Pouliasis et al. (2017), the choice to include a massive spheroid in this model—as well as in the original Allen & Santillan (1991) model—is dictated by the need to reproduce CO/HI-based velocity curves, as those provided by Sofue (2012), which show a rise and then a sudden decrease of the velocity curve in the inner Galactic regions ($R \leq 2 - 3$ kpc). In an axisymmetric model, such rise can be reproduced only if a central spheroidal component, with a typical mass greater than 10% of that of the disk(s), is added. However, as shown by Chemin et al. (2015), the central rise observed in

Table 1: The parameters of the Galactic mass models adopted in this work. Masses are in units of $2.32 \times 10^7 M_\odot$, distances in units of kpc.

Parameters	M_{bulge}	M_{bar}	M_{thin}	M_{thick}	M_{halo}	b_{bulge}	a_{bar}	b_{bar}	c_{bar}	a_{thin}	b_{thin}	a_{thick}	b_{thick}	a_{halo}
PI	460.0	0.0	1700.0	1700.0	6000.0	0.3	–	–	–	5.3000	0.25	2.6	0.8	14.0
PII	0.0	0.0	1600.0	1700.0	9000.0	–	–	–	–	4.8000	0.25	2.0	0.8	14.0
PII-0.3-SLOW	0	990.0	1120.0	1190.0	9000.0	–	4.0	1.	0.5	4.8000	0.25	2.0	0.8	14.0

the rotation of the molecular gas in the inner Galaxy may be an effect of non circular motions generated by large scale asymmetries like the bar. Moreover, this feature is not reported in all the observational studies (see, for example Reid et al. 2014, on which model PII is based). In other words, if we do not assume that the mass distribution of the inner Galaxy is axisymmetric, the need for a massive spheroidal component to reproduce velocity curves such as those by Sofue (2012) no longer persists. In addition to that, in the last decade, a number of works have shown that if a spheroidal bulge exists in the central regions of our Galaxy, it has to be small (few percents of the mass of the disk at the most, see among others Shen et al. 2010; Kunder et al. 2012; Di Matteo et al. 2015; Gómez et al. 2018). All these arguments suggest to employ this model (as well as all models including a massive central spheroid; see, for example, Irrgang et al. 2013), with care when dealing with the central parts of the Galaxy. Since models with a massive central spheroid, however, are still used in the literature, we have included model PI here, as a term of comparison.

2.3.2. Model II by Pouliasis et al. (2017): an axisymmetric, bulge-less, mass model for the Galaxy

Model II by Pouliasis et al. (2017) (abbreviated name: PII) consists of a spherical dark matter halo, with the same functional form adopted in the Allen & Santillan (1991) model, and of two disk components (a thin and a thick disk) with same functional form as PI. This model does not include any central spheroid (i.e. it is a bulge-less model) and thus its total potential is the sum of three components only:

$$\Phi_{tot}(R, z) = \Phi_{thin}(R, z) + \Phi_{thick}(R, z) + \Phi_{halo}(r) \qquad (8)$$

with the thin, thick disks and dark matter halo having the same functional forms adopted in PI.

As it has been shown in Pouliasis et al. (2017), this model satisfies a number of observational constraints, such as the stellar density at the solar vicinity, thin and thick disc scale lengths and heights, the rotation curve as provided by Reid et al. (2014), and the absolute value of the perpendicular force K_z as a function of distance to the Galactic centre (see Sect. 2.5 in Pouliasis et al. 2017). Being however, an axisymmetric model, it fails describing accurately the inner few kpc of the Galaxy, where the stellar mass distribution has been shown to be asymmetric.

2.3.3. Model II with a massive, slowly rotating, stellar bar

The third mass model (abbreviated name: PII-0.3-SLOW) that we use in this paper is a version of PII by Pouliasis et al. (2017) modified to include a rotating stellar bar, whose mass has been assigned to be 30% of the (thin+thick) disk mass of PII. We assume that the bar rotates with a constant pattern speed of $\Omega_{bar} = 38$ km s^{-1}kpc^{-1}, and that it is currently inclined of 25° with respect to the Sun-Galactic center direction (see Bland-Hawthorn & Gerhard 2016). We model it as a triaxial distribution, whose gravitational potential is given by Long & Murali

(1992):

$$\Phi_{bar}(x, y, z) = \frac{GM_{bar}}{2a_{bar}} ln \left(\frac{x - a_{bar} + T_-}{x + a_{bar} + T_+} \right) \qquad (9)$$

with $T_\pm = \left[(a_{bar} \pm x)^2 + y^2 + (b_{bar} + \sqrt{c_{bar}^2 + z^2})^2 \right]^{1/2}$ and $a_{bar}, b_{bar}, c_{bar}$ the characteristic bar parameters. The total gravitational potential generated by this model has thus the form:

$$\Phi_{tot}(x, y, z) = \Phi_{thin}(R, z) + \Phi_{thick}(R, z) + \Phi_{halo}(r) + \Phi_{bar}(x, y, z) \quad (10)$$

(see Table 1 for all characteristic values). Practically, to include the bar we have reduced the mass of the disks in such a way to maintain the total stellar mass of this model as that of PII. Long & Murali (1992) provide the formulas of the accelerations generated by this triaxial distribution in the reference frame of the bar. To calculate and add them to the accelerations generated by the disks and dark matter halo, at each time step we convert the positions of all particles in the rotating, non-inertial, reference frame of the bar, compute the corresponding accelerations on each particle, and then transform these accelerations back in the inertial reference frame described in Sect. 2.1. In this way, the accelerations due to the bar are added to those generated by the other terms of the Galactic mass distribution.

We emphasize that we do not consider this model as the best possible representation of the Galactic mass distribution, especially in the central region. It can, however, provide a first indication on how the inclusion of a rotating asymmetric component in the inner Galaxy can affect the globular cluster streams, near and far from the Galactic center.

Moreover, since the exact characteristics of the Milky Way bar are still subject to debate (see, for example, Bland-Hawthorn & Gerhard 2016), it is important to explore how varying the parameters adopted in this paper, such as the pattern speed, the mass or the length of the bar, can affect the characteristics of the whole set of streams. More complex shapes for the bar can also be explored, for example substituting the inner parts of the triaxial bar with a boxy/peanut-shaped morphology, which has been shown to characterize the inner Milky Way (see, for example Wegg & Gerhard 2013; Wegg et al. 2015). These topics are, however, beyond the scope of the present paper. In sum, given the uncertainties on the bar's physical extent and how it can change over the time span investigated here, its affect on the streams presented here are purely indicative.

3. Results

A few premises Given the large number of simulations carried out and the wealth of information contained in them, it is not possible to exhaust all possible applications of this simulation database in this paper. We have therefore chosen to proceed as follows.

In Section 3.1 we present an overview of the distribution of all streams in Galactic coordinates. This coordinate space will be the one used in the remainder of the entire article. This first section allows us to show qualitatively how the global distribution of streams varies, depending on the Galactic potential used.
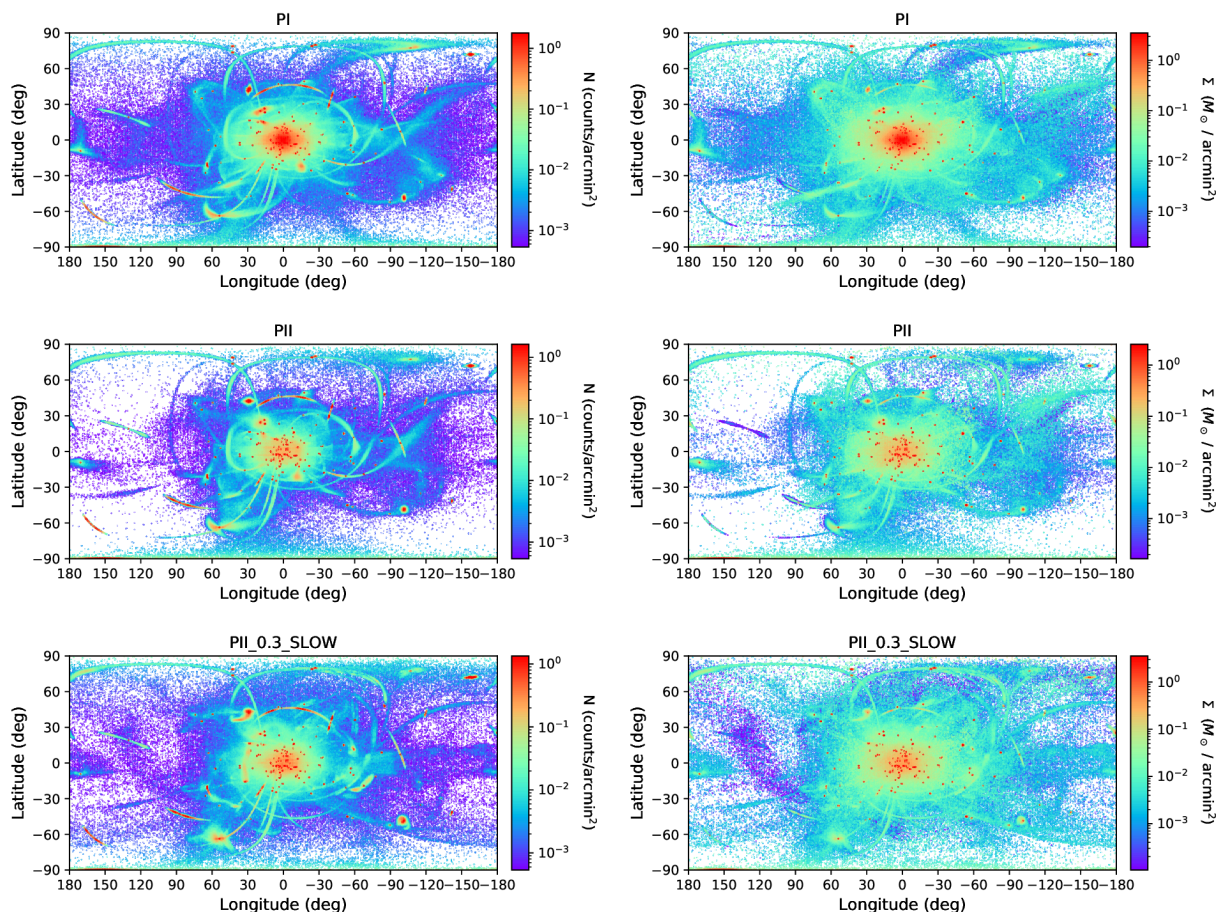
Fig. 1: (*Top*) *Left*: Surface number density distribution in (ℓ, b) plane of the *ensemble* of extra-tidal features around the entire population of Galactic globular clusters at the current time, as predicted by our models. *Right*: Surface mass density, as predicted by our models. Top row corresponds to model PI, the middle to model PII, and the bottom column to model PII-0.3-SLOW, as indicated. All densities are expressed in a logarithmic scale. The red point-like density maxima correspond to the current positions of the globular clusters. Values of higher density are over-plotted. Thus in the case of mass density, diffuse tidal debris of more massive globular clusters covers the entire (ℓ, b) space and occults delicate tidal features, which are more visible when considering number density counts. In all panels, only the reference simulations are shown, for better clarity.

We then move on (Section 3.2) to present the global system of streams as a function of their distance from the Sun. In this Section, we also show the kinematic properties of the streams, such as proper motions and line-of-sight velocities, that can be directly compared to Gaia data or other astrometric and spectroscopic surveys. This section also allows us to show the variety of morphologies that the stars which escaped from globular clusters can take. In Section 3.3, we explore this issue in more detail, showing how these morphologies depend primarily on the orbital characteristics of the clusters, and their distance from the Galactic center. For the most interesting cases, we compare the tidal structures predicted by our simulations with streams found in observational data. For this purpose, we make use of the *galstreams* library of stellar streams in the Milky Way (Mateu 2022), which constitutes a unique and public database summarizing angular positions, distances, proper motions and line-of-sight velocity tracks for nearly a hundred Galactic stellar streams. Any stream not in this library will not be compared to our simulations, in the context of this paper.

For the interested reader, the tidal features associated with each of the 159 simulated clusters are presented in Appendix C. In order not to make this appendix too long, the above tidal features are presented only in the case of the potential PII. However,

all the data will be made available to the community at a dedicated site[6], and thus, the interested reader will be able to see how the characteristics of these streams change, for any cluster, in the three chosen potentials.

3.1. A sky full of streams

Fig. 1 shows the number and mass density distributions of the whole set of simulated globular clusters and their extra-tidal features in Galactic longitude and latitude, and for the three Galactic potentials.

For all Galactic mass models adopted, a striking characteristics of the plots in Figs. 1 is the variety of features that our models predict, which are reminiscent of the tidal tails, stellar streams, and shells, produced by interacting and merging galaxies in the process of mass assembly (see, for example, Mancillas et al. 2019). Some clusters have very thin and elongated streams, which describe arcs that can extend up to 180° in longitude, or tens of kpc in physical space. In some other cases, extra-tidal features appear shorter (a few up to ten degrees), and sometimes also thicker (about 10° in the sky) than others. Finally, in some

---

[6] `http://etidal-project.obspm.fr/`

cases, clusters are surrounded by extended structures, such as halos, rather than coherent and thin streams.

This variety of properties depends on several factors: the distance of the stream to the Sun (due to projection; i.e. for a given physical thickness, the closer the stream is to the Sun, the more extended it appears in the (ℓ, b) plane), its orbital phase (towards the peri-center or the apo-center of the orbit) and the orbital properties of the parent globular cluster. We also see from these figures that stellar particles stripped from their parent clusters do not only redistribute in coherent structures, but in some cases can also contribute to a more diffuse density distribution.

Because of the large number of simulated clusters, we have chosen not to present the corresponding extra-tidal features one by one in the main part of this paper, but have rather decided to describe these extra-tidal features with a global approach, by first adopting a criterion based on the distance of these features to the Sun (see Sect. 3.2), and then discussing the types of distributions tidal debris can have and how these depend on the cluster orbital parameters (see Sect. 3.3). All the extra-tidal structures generated by the 159 globular clusters simulated in this paper, and their corresponding uncertainties, are reported in Appendix C. Among them, the reader will find clusters with thin and elongated tails—as IC 4499, NGC 3201, NGC 4590, NGC 5024, NGC 5053, Pal 5, to cite only a few—clusters like AM 1, Pal 14, Pal 4, and Pal 15 whose extra-tidal material shows a halo-like configuration, and clusters like NGC 1261, NGC 4147, NGC 6356, UKS 1, whose stripped stars show a remarkable diffuse distribution in the field.

Finally, even if our models are not tailored to accurately reproduce the mass loss from globular clusters—since, as described in Sect. 2.2, we adopt a test-particle approach with a time-constant globular cluster potential—it is however tempting to estimate, to first order, the total mass associated to the tidally stripped population, and compare it to the current mass. By calculating the mass lost in the field in the past 5 Gyr as the sum of the mass of all particles[7] which have escaped the cluster ($t_{\rm esc} > 0$), we find that the PI model sheds $2.1 \times 10^7 M_\odot$, which is 55% of the GC population's current mass. The PII model shed $2.7 \times 10^6 M_\odot$, which is 7% of the current mass. Similarly, PII-0.3-SLOW model lost $3.7 \times 10^6 M_\odot$, which is 10% of the current mass and gives a half mass radius of 6.3 kpc.

This mass roughly constitutes one-hundredth to one-tenth of the total stellar halo mass (Bland-Hawthorn & Gerhard 2016), and it is probably only a lower limit to the mass of escaped stars in the field, since a number of clusters initially in the Galaxy must have been destroyed over time (see Introduction), and thus are not identifiable any longer as globular clusters today. It is also interesting to note that escaped stars are mostly redistributed in the inner Galaxy, the half mass radius of the PI model being 4.0 kpc and that of the PII and PII-0.3-SLOW models being 6.3 kpc.

The total mass lost from the clusters, as well as its spatial distribution, hence depends on the Galactic potential adopted: the variations between the PI model and both the PII and PII-0.3-SLOW models are of course caused by the PI's inclusion of the bulge, which leads to larger tidal forces in the center of the galaxy and subsequently drives larger mass loss.

---

[7] To estimate the mass of particles in each cluster we have quantified the number of particles, N_{bound}, bound to the cluster at the end of the simulation and calculated the corresponding particle mass as $m_p = M_{GC}/N_{bound}$, where M_{GC} is the current mass of a cluster given in Table A.1.

Despite the differences in the modeling approach, it is interesting to compare our results to those of Baumgardt & Sollima (2017). Briefly, our experiments differ in the following ways: they employ N-body simulations while we use our test-particle approach; they have an integration time of 12 Gyrs compared to our 5 Gyrs; and lastly their clusters have circular orbits in a Galactic potential modeled as an isothermal sphere as compared to the more realistic orbits and Galactic potentials considered in this work. Interestingly, the authors find that over 12 Gyrs their population of globular clusters loose 2/3 of their initial mass. This is roughly consistent with our usage of the PI model, whose globular clusters shed 35% of their initial mass in 5 Gyrs, which is roughly half the mass found by Baumgardt & Sollima (2017) in a period that is also about half as long.

3.2. From the nearest to the furthest extra-tidal structures

The analysis presented in this Section, as well as the corresponding Figures 2, 3, 4, and 5, are restricted to the PII model.

In this section we analyze structures located at different distances from the Sun. We identify structures as main or secondary on the basis of the fraction of stars they represent. If, for example, a cluster contributes more than 10% of its stripped stars in a given distance range, we consider the associated structure to be significant and we define it as a main structure in this distance range. If, on the other hand, the fraction of stripped stars from a cluster is between 1% and 10%, we define the structure associated as secondary. Structures which constitute less than 1% of the cluster mass are considered insignificant in that range. Main and secondary structures for each distance bin are reported in Table 2, where they are named by their progenitor cluster. Below we describe the structures encountered at different distances from the Sun, from the closest to the most distant. For the following discussions, we refer to Figs. 2 to 5, where we report the different streams in a given distance range (top row in each figure), the corresponding mass density generated by all the structures found in that bin (second row), the longitudinal and latitudinal proper motions map (third and fourth rows), and the line-of-sight velocities (bottom row).

The [0–2] kpc distance range: Among the 159 simulated clusters, only NGC 6121 is currently at a distance of less than 2 kpc from the Sun. In addition to stars stripped from this cluster within this distance-to-the-Sun range, we have identified very diffuse and low density extra-tidal stars associated to five other clusters, which are currently several kpc away from the Sun, as reported in Table 2. Of these, only UKS 1 and NGC 6121 have a significant fraction of their stripped mass in this distance range. All the others contribute with only a few percent. None of these clusters seem to show well defined, stream-like features in the (ℓ, b) plane. This extra-tidal material appears indeed quite uniformly redistributed, in a latitude range mostly inside $-30°$ to $30°$, and mostly at negative longitudes. Because in this interval range no remarkable extra-tidal structure is found on the sky, we have decided to plot this distance bin together with the [2–5] kpc bin (see Fig. 2, left column).

The [2–5] kpc distance range: As the distance from the Sun increases, many more tidal structures are intercepted. Eleven globular clusters are found at a distance between 2 and 5 kpc from the Sun; and together with structures emanating from these clusters we also find extra-tidal material associated to other 48
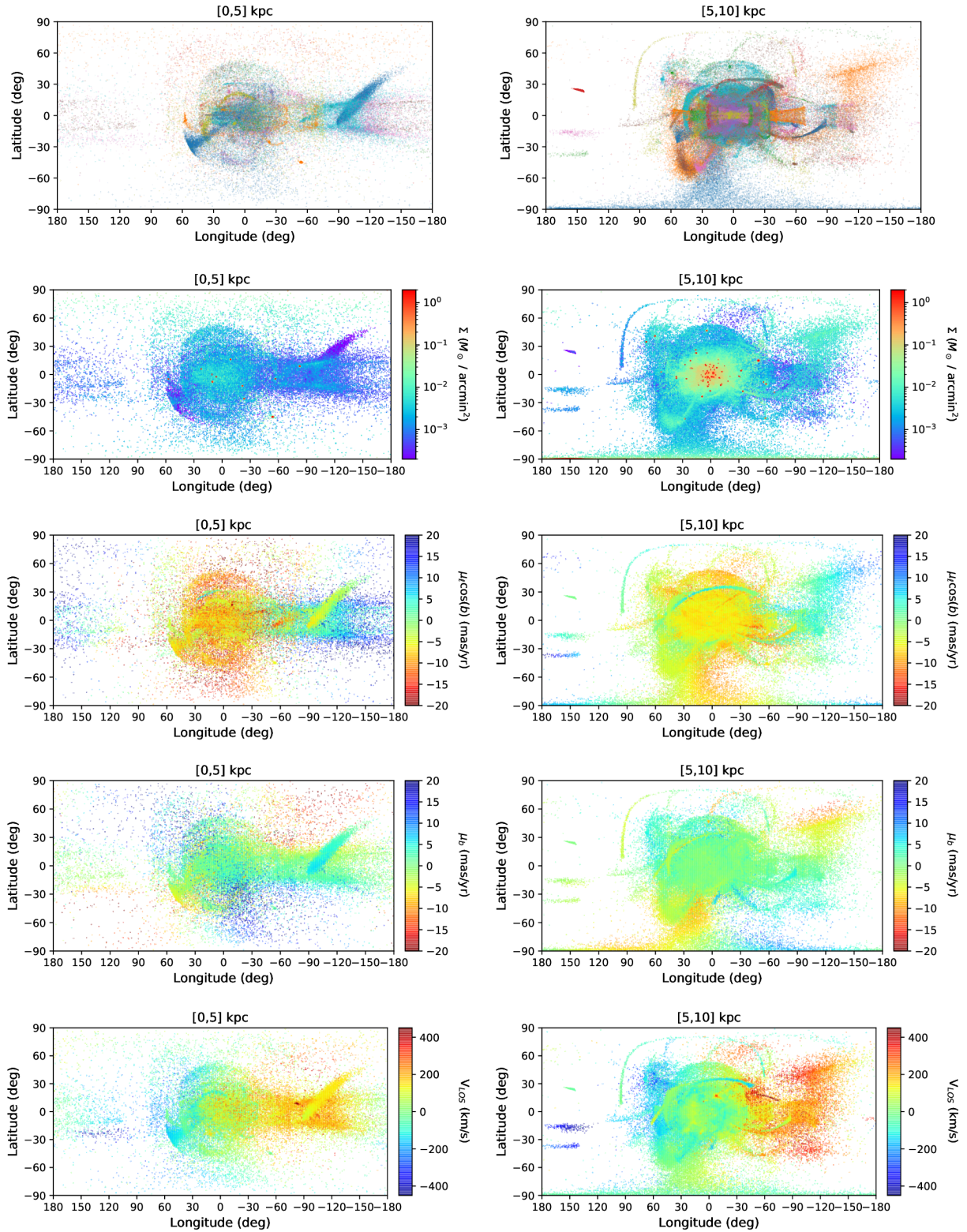
Fig. 2: (*Left column*): Extra-tidal features found at a distance of [0,5] kpc from the Sun and projected in the (ℓ, b) plane. *Top row:* Scatter plot, with different colors indicating different progenitor clusters; *Second row:* Mass density map in logarithmic scale; *Third row:* Map color-coated by proper motions in longitudinal direction; *Fourth row:* Map color-coated by proper motions in latitudinal direction; *Bottom row:* Map color-coded by line-of-sight velocities. (*Right column*): same as left column, but for the tidal features found at a distance of [5, 10] kpc from the Sun. *Note* that the 10 colors used in the top panels are recycled between the 159 clusters. Thus, all particles from the same cluster share one color, but a color is not unique to a cluster. This figure shows streams, and their corresponding properties, as found for model PII only. In all panels, only the reference simulations are shown, for better clarity.
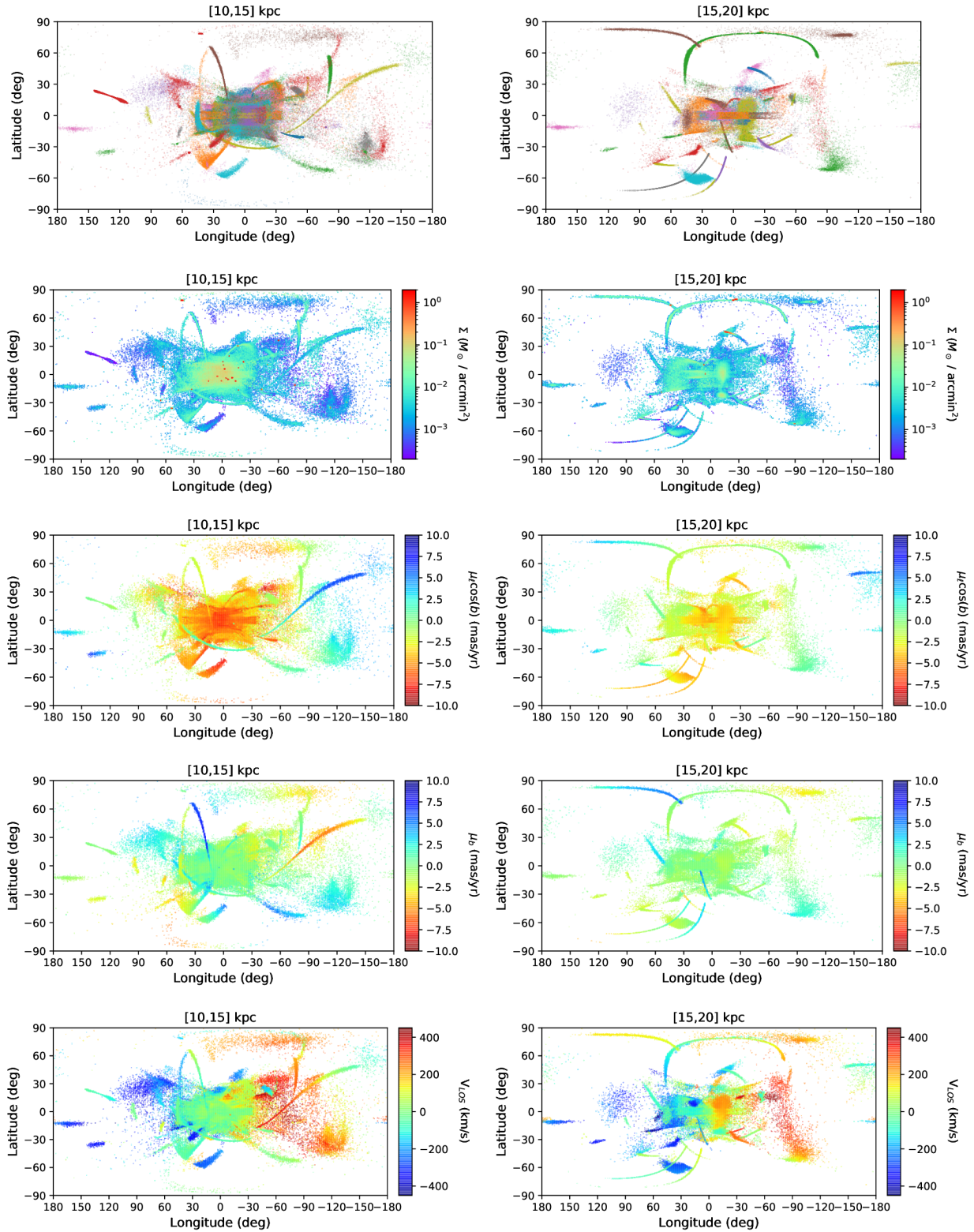
Fig. 3: As for Fig. 2, but for two different distance bins: [10, 15] kpc from the Sun (*left column*) and [15, 20] kpc from the Sun (*right column*). . This figure shows streams, and their corresponding properties, as found for model PII only. In all panels, only the reference simulations are shown, for better clarity.

clusters, 19 of which are significant, as listed in Table 2. Some extra-tidal structures are clearly identifiable, even when over-plotted with all the others: it is the case, for example, of the tidal material associated to the E 3 cluster, which appears as
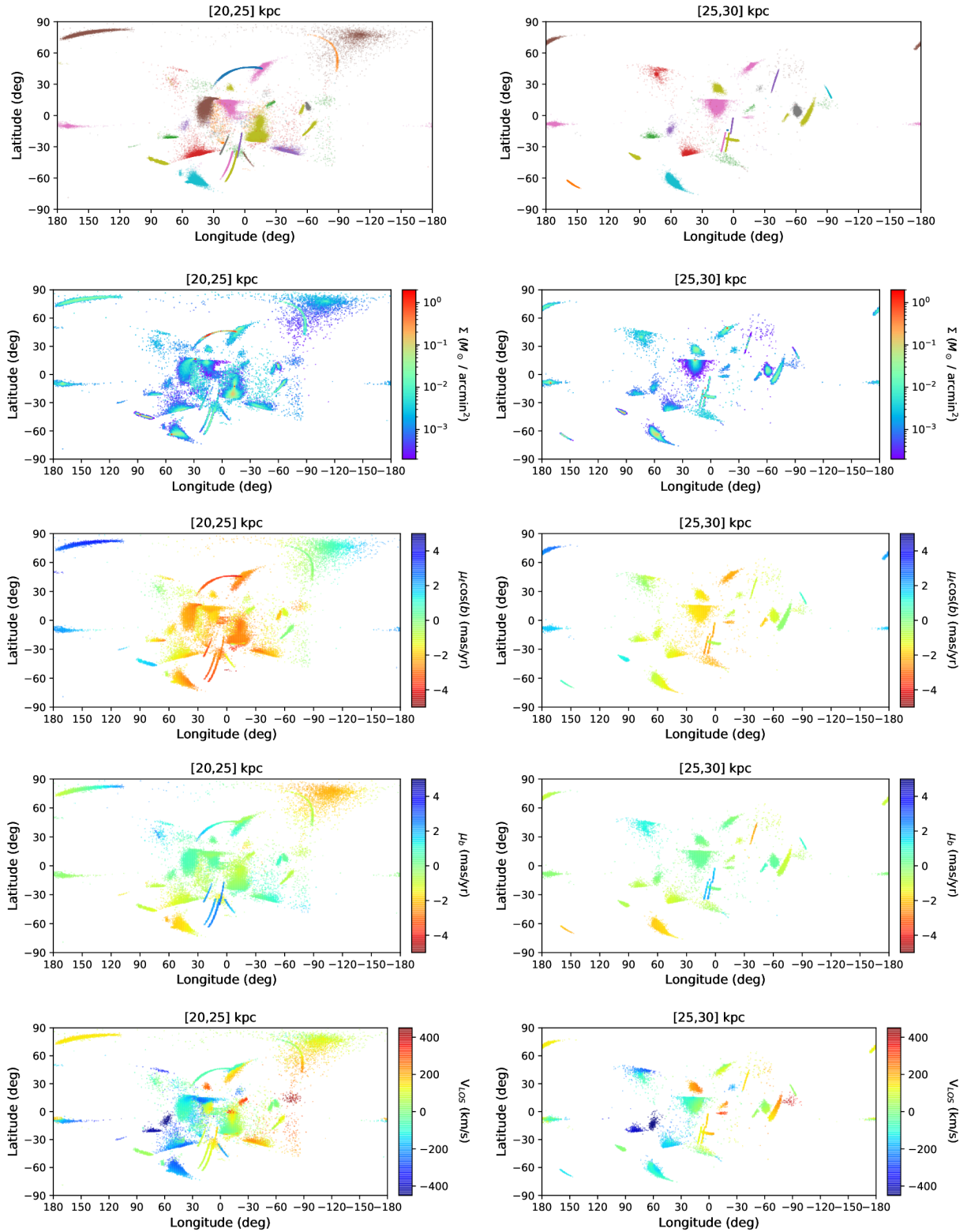
Fig. 4: As for Fig. 2, but for two different distance bins: [20, 25] kpc from the Sun (*left column*) and [25, 30] kpc from the Sun (*right column*). This figure shows streams, and their corresponding properties, as found for model PII only. In all panels, only the reference simulations are shown, for better clarity.

an extended thick stream, as shown of Fig. 2 at approximately −100° longitude; and of the complex tidal structure associated to BH 140, which appears like a ribbon in the sky, with a bifurcation at negative longitudes whose edges extend to about −30°

and 30° latitude. In addition to these, there are a series of circular halos concentric about the Galactic center, with abrupt drop-offs in density tracing the furthest extent of diffuse debris emanating from a variety of clusters. Overall, few streams are immediately
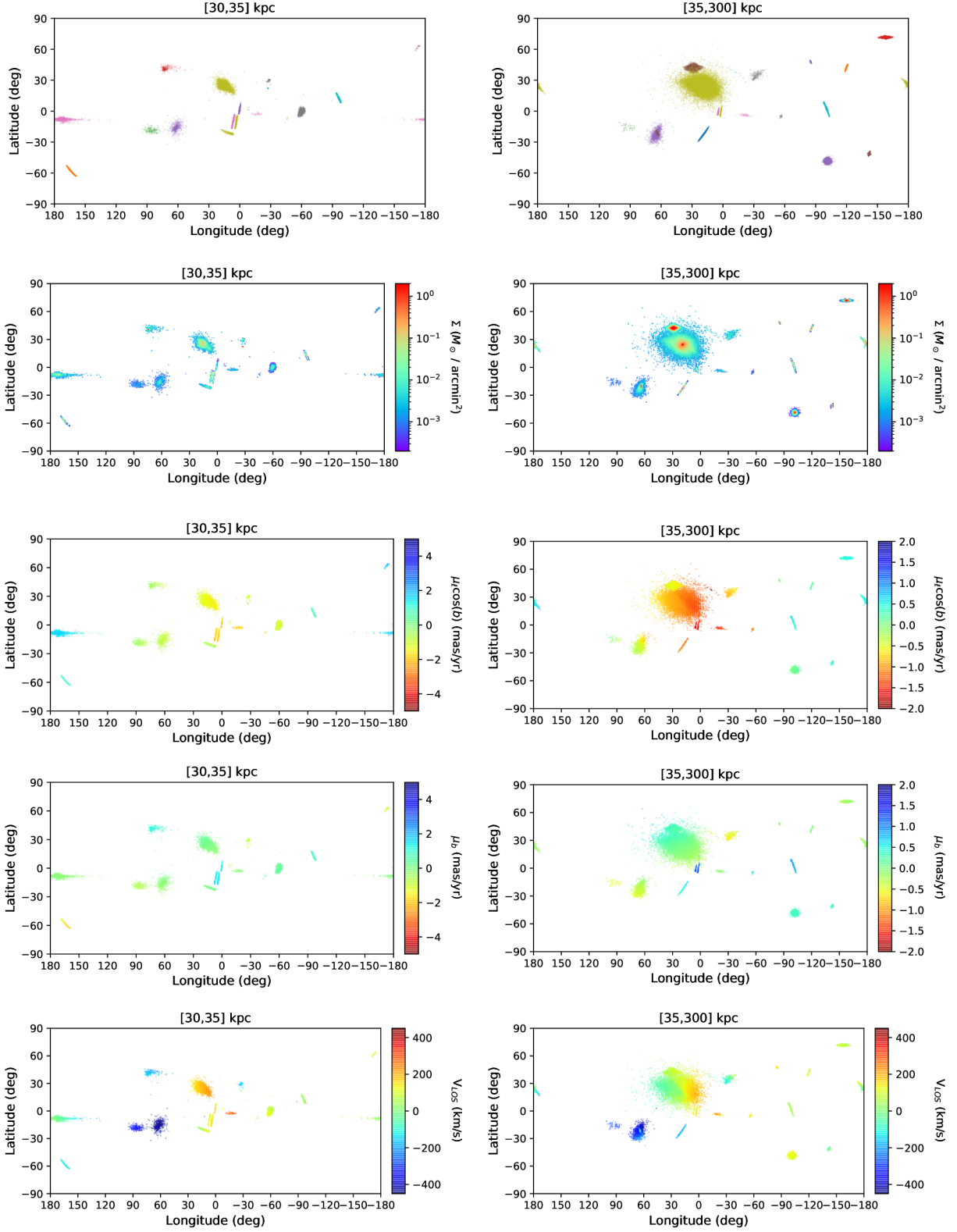
Fig. 5: As for Fig. 2, but for two different distance bins: [30, 35] kpc from the Sun (*left column*) and [35, 300] kpc from the Sun (*right column*). This figure shows streams, and their corresponding properties, as found for model PII only. In all panels, only the reference simulations are shown, for better clarity.

recognizable in this range, though plenty of debris is present. This is expected given that this range samples a bite of the Sunside of the Galactic disk, and that this range has a relatively small volume. In this, as in the following distance ranges, the $v_{\ell os}$ maps show that the tidal material at negative Galactic longitudes has, on average, positive $v_{\ell os}$ while material at positive Galactic lon-

gitudes has, on average, negative v_{los}, which is due to the solar reflex velocity. This is the same trend observed for the whole set of radial (i.e. line-of-sight) velocities in Gaia DR3—for instance see the bottom panel of Fig. 5 from Katz et al. (2022), although less extreme velocities are reported in their plot since their data is dominated by disk stars whereas our maps have a high proportional contribution of halo stars (additionally, they use median values in their bins while we use an average). In order to quantify the net rotation of the system of streams, we calculate the mean angular momentum about the Galactic pole as $\langle L_z \rangle = \sum_i L_{z,i} m_{p,i} / \sum_i m_{p,i}$, where $m_{p,i}$ is the mass of each star particle indexed by i as discussed in footnote 7 and $L_{z,i}$ is the corresponding particle's angular momentum. The mean angular momentum is found to be $\langle L_z \rangle = -300$ kpc km s^{-1}, which shows a slight co-rotation of the system of streams with the disk though there is much dispersion about this value as shown in bottom right panel of Fig. D.1 in the Appendix.

The [5–10] kpc distance range: The [5–10] kpc distance range, which includes the Galactic center, contains much more material. A total of 79 clusters are found in this range, together with tidal structures associated to 131 different progenitors redistributed among main and secondary structures. Some tiny streams are visible in the density maps as well as in proper motions and line-of-sight velocity spaces (see Fig. 2, right column): the trailing portion of the tail of the globular cluster Pal 1, at $(\ell, b) \sim (140°, 25°)$; the most extreme portion of the trailing tail of NGC 3201 at $(\ell, b) \sim (150°, -37°)$; the waterfall-like shape of NGC 288, particularly evident at $b \lesssim -60°$; the thin inverted U-shape of NGC 4590 at positive latitudes spanning a large longitude extent from $\ell \simeq -60°$ to $100°$; the portion of the E 3 tails the closest to the cluster at $(\ell, b) \sim (-75°, -15°)$, which continues from the more easily recognizable portion in the [0–5] kpc bin.

The [10–15] kpc distance range: In the [10–15] kpc range, we find tidal structures associated to 134 progenitors, as listed in Table 2 and reported in Fig. 3 (left column), 27 of which are related to globular clusters that are also found in this distance bin. We note that, at these distances from the Sun, the distribution of tidal features in directions towards the Galactic center, from $-30°$ to $30°$ longitude, appears less fuzzy than the one characterizing the [0–5] and [5–10] kpc distance bins. Tidal features here are beyond the Galactic center, and are mostly associated to disk or halo clusters.

Among the thinnest structures, we find the stream associated to Pal 1, at $(\ell, b) \sim (120°, 15°)$ which is also visible in the distance bin [5–10] kpc (see previous discussion), but which is even more elongated here. NGC 6101 shows the nearest portion of its long thin diagonal tidal tail that spans negative longitudes and ranges from $-15°$ to $45°$ latitude. Additionally this stream is also unique against its counter parts in proper motion space. NGC 5053's nearest portion appears as a vertical tidal tail at $-80°$ longitude. Similarly, NGC 5466 is shown vertically at $25°$ longitude.

Among the thickest structures, we can recognize general diffuse and bow-tie like shapes. There are also spoke-like structures departing radially from the Galactic center. For instance, the extra-tidal material associated to: NGC 7078 at $(\ell, b) \sim (60°, -28°)$; NGC 7089, nearly parallel to the previous structure, but at lower latitudes at $(\ell, b) \sim (50°, -40°)$.

The [15–20] kpc distance range: At larger distances ([15 − −20] kpc range, see Fig. 3), some of the most striking features are associated to the clusters NGC 5024 and NGC 5053, whose long thin tails essentially overlap in this distance, with the latter covering the former, and appearing at high latitudes spanning a longitudinal range from $\ell \sim -90°$ to $\ell \sim 45°$; again, the long thin stream of NGC 5466 appears in this range (as will be the case for the next) and is at high latitudes at roughly $85°$ and positive longitudes; the thicker extended structure of NGC 4147 whose diffuseness emanates from about $(\ell, b) \sim (-100°, 80°)$.

In this distance bin, we find long tidal tails emanating from globular clusters associated to the Sagittarius dwarf galaxy, which are particularly visible at negative longitudes: a long thin stream is associated to Pal 12 at positive longitudes and latitudes $b \leq -15°$, as well as two overlapping structures at $0° \lesssim \ell \lesssim 30°$ longitude, i.e. Ter 7 (and Ter 8 in the next distance bin). A word of caution is needed here: the mass loss from these clusters may be incorrect, since we do not include the presence of the Sagittarius dwarf galaxy itself. The potential well associated to this latter could change the tidal effects experienced by clusters associated to Sagittarius, especially in the case of NGC 6715, which sits at the center of this dwarf galaxy. The inclusion of the Sagittarius dwarf will be the subject of future investigations. Overall, in this distance bins, we find 11 clusters and 61 streams, all listed in Table 2.

The [20–25] and [25–30] kpc distance ranges: In the following distance bins ([20–25] kpc and [25–30], see Fig. 4), globular clusters and extra-tidal structures become less numerous, though some are still visible, for instance Pal 5 at $(\ell, b) \sim (0°, 45°)$. In more detail, in the [20–25] kpc bin we find tidal features associated to 37 different progenitors, 8 of which are associated to globular clusters whose current positions are in the same distance bin; in the [25–30] kpc bin 7 clusters are found, together with tidal features associated to 30 other progenitor clusters which do not lie in this same distance range. In both bins, the streams emanating from globular clusters associated to the Sagittarius dwarf galaxy are still visible, as well as the most extreme portion of the tail associated to NGC 5466.

The [30–35] and [35–300] kpc distance ranges: Finally, in the last distance bins (see Fig. 5), thin streams become rare. Some small streams are visible: Pyxis at $(\ell, b) \sim (-100°, 0°)$; NGC 2419 at $(\ell, b) \sim (-180°, 30°)$; Pal 4 at $(\ell, b) \sim (-160°, 75°)$; Pal 3 at $(\ell, b) \sim (-120°, 45°)$. Many more have a diffuse and halo-like structure. For instance, the blob associated to Pal 15, centered at $(\ell, b) \sim (15°, 20°)$; AM 1 at $(\ell, b) \sim (-100°, -55°)$; Eridanus at $(\ell, b) \sim (-140°, -45°)$; Pal 14 at $(\ell, b) \sim (30°, 45°)$; Laevens 3 at $(\ell, b) \sim (65°, -20°)$, which is completely enveloped by NGC 7006. In total, in these two distance bins we find 4 and 12 clusters, and their associated streams, together with extra-tidal material associated to 14 and 19 progenitors total, respectively.

3.3. Disk, inner and outer halo clusters: a variety of morphologies and shapes for extra-tidal structures

The analysis presented in the previous section allows us to appreciate the variety of morphologies found for extra tidal structures, from padlocks to "Easter eggs", disks, ribbons, and canonical streams. Moreover, some structures are limited in latitude and longitude, while some others fill nearly the entire sky.

Table 2: List of tidal structures found in different intervals of distance to the Sun. The tidal structures are named by their progenitor clusters. If the parent cluster is also in the distance range under consideration, the name of the tidal structure is shown in bold. Second column reports the main structures found in a given distance bin. The third column list secondary structures. The numbers in parenthesis in the second column and third column (numbers with normal font) correspond to the total number of main and secondary structures found in a given distance range. The number of clusters in each distance bin is also reported in the second column (bold numbers in parenthesis).

Distance (kpc)	Main tidal structures	Secondary tidal structures
[0-2]	(**1**,2) **NGC6121**, UKS1	(4) BH140, Djor1, NGC6333, NGC6356
[2-5]	(**11**,30) **NGC6397, NGC6544, NGC3201, BH140, NGC104, NGC6838, NGC6366, NGC6752, IC1276, NGC6656, 2MASS-GC01**, NGC6284, NGC6356, NGC6287, VVV-CL001, NGC6254, NGC5927, E3, NGC6121, VVV-CL001, Djor1, UKS1, Ter10, 2MASS-GC02, Pal10, NGC5139, NGC6333, NGC6441, NGC6541, NGC288	(29) FSR1716, FSR1758, NGC1851, NGC1904, NGC2298, NGC2808, NGC362, NGC4372, NGC4833, NGC5897, NGC5986, NGC6205, NGC6218, NGC6235, NGC6273, NGC6316, NGC6352, NGC6388, NGC6496, NGC6681, NGC6749, NGC6760, NGC6809, NGC6864, NGC7078, Pal2, Pal8, Ter12, Ton2
[5-10]	(**79**,124) **VVV-CL001, NGC7099, NGC6362, Ton2, Djor1, VVV-CL001, NGC6496, Djor2, NGC6535, NGC6528, NGC6539, NGC6540, NGC6553, 2MASS-GC02, Ter12, BH261, Ter9, NGC6712, NGC6717, NGC6723, NGC6749, NGC6760, Pal10, HP1, Ter4, Ter2, Ter3, NGC2298, E3, NGC4372, NGC4833, NGC5904, NGC5927, FSR1716, Lynga7, NGC6144, NGC6171, NGC6352, ESO452-SC11, NGC6218, FSR1735, NGC6254, NGC6256, NGC6287, NGC6293, NGC6304, NGC6355, NGC6809, NGC6637, NGC6402, NGC6325, NGC6341, NGC6342, NGC6380, NGC6401, NGC6440, NGC6517, NGC6522, NGC6541, NGC6558, NGC6624, NGC6626, NGC6638, NGC6642, NGC6652, NGC6681, Pal6, Ter1, Ter5, Ter6, NGC6333, NGC288, NGC362, NGC6273, NGC6266, NGC6205, NGC5139, Liller1, NGC5946**, NGC5897, NGC1904, NGC6752, NGC6656, NGC6121, NGC1851, NGC6864, NGC7078, NGC7089, NGC6316, NGC5272, NGC6779, NGC2808, NGC4590, Rup106, NGC104, NGC4147, NGC3201, Pal11, Pal1, NGC1261, BH140, NGC6235, Ter10, NGC6569, UKS1, NGC6453, NGC6139, NGC6426, NGC6397, NGC6093, NGC6388, FSR1758, IC1276, NGC6838, NGC6366, NGC5986, NGC6441, NGC6356, NGC6584, NGC5286, NGC6544, NGC6284, Pal8, NGC6981	(7) 2MASS-GC01, IC1257, NGC5634, NGC5694, NGC6229, NGC7006, Pal2
[10-15]	(**27**,115) **NGC6453, NGC5272, NGC6584, Pal8, NGC6316, NGC5897, NGC6284, NGC6139, NGC6093, NGC5986, NGC5286, NGC6235, NGC2808, NGC1904, NGC1851, NGC6101, NGC6779, NGC6388, Pal11, Pal1, Ter10, NGC4590, NGC7089, NGC6569, NGC7078, FSR1758, NGC6441**, NGC6304, NGC6254, FSR1735, NGC6426, NGC6397, NGC6362, Ton2, NGC6256, NGC6366, NGC6287, NGC6352, NGC6355, NGC6356, NGC6218, NGC6293, VVV-CL001, NGC6171, NGC5024, NGC1261, NGC2298, E3, NGC3201, NGC4147, NGC4372, Rup106, BH140, NGC4833, NGC5053, Ter3, NGC5466, NGC5634, IC4499, NGC5904, NGC5927, FSR1716, UKS1, NGC6121, NGC6144, Lynga7, NGC6553, VVV-CL001, NGC6496, NGC5946, NGC6205, NGC6266, NGC6273, NGC6333, NGC6341, NGC6342, NGC6401, NGC6402, NGC6517, NGC6541, NGC6544, NGC6558, NGC6626, NGC6652, NGC6656, NGC6681, NGC6864, Pal6, Ter1, Ter5, NGC5139, NGC362, NGC104, Ter12, Djor2, NGC6535, NGC6528, NGC6539, NGC6540, 2MASS-GC01, Ter9, 2MASS-GC02, IC1276, BH261, NGC7099, NGC6712, NGC6723, NGC6749, NGC6752, NGC6760, NGC6809, NGC6838, NGC6934, NGC6981, NGC288	(18) Djor1, ESO280-SC06, ESO452-SC11, HP1, IC1257, NGC5694, NGC5824, NGC6229, NGC6325, NGC6380, NGC6638, NGC6642, NGC6717, NGC7006, NGC7492, Pal10, Pal2, Ter6
[15-20]	(**11**,46) **NGC6356, NGC5466, NGC1261, UKS1, NGC4147, IC4499, NGC5024, NGC5053, Pal12, NGC6981, NGC6934**, NGC6101, NGC5904, Pal5, NGC5824, NGC5634, NGC7089, FSR1758, NGC4833, BH140, NGC4590, Rup106, NGC3201, Pal2, NGC5272, Djor1, NGC6426, NGC7078, NGC6864, NGC6715, NGC6656, NGC6341, NGC6333, NGC5286, NGC362, NGC2808, NGC1851, NGC104, NGC7492, Pal10, Ter7, NGC6779, NGC6584, IC1276, ESO280-SC06	(15) 2MASS-GC02, IC1257, NGC1904, NGC2298, NGC4372, NGC5139, NGC5694, NGC6121, NGC6205, NGC6229, NGC6838, NGC7006, NGC7099, Pal13, Ter8
[20-25]	(**8**,29) **Pal5, NGC7492, Pal13, Rup106, NGC6864, NGC6426, ESO280-SC06, Ter7**, NGC5466, IC4499, NGC5634, NGC7089, NGC5824, NGC5024, NGC4590, NGC4147, NGC3201, NGC5272, IC1257, NGC5904, NGC6101, NGC6584, Arp2, Ter8, NGC6934, NGC6981, Pal12, NGC6229, Pal2	(9) Djor1, FSR1758, NGC1261, NGC1851, NGC1904, NGC2298, NGC2808, NGC5694, NGC7006
[25-30]	(**7**,20) **NGC6715, Pal2, AM4, NGC5634, Ter8, Arp2, IC1257**, NGC5824, Rup106, NGC5694, IC4499, NGC6101, NGC5904, NGC6229, Ter7, NGC6934, NGC6981, Pal13, NGC7492, Whiting1	(10) NGC1851, NGC1904, NGC3201, NGC4147, NGC4590, NGC5466, NGC7006, NGC7089, Pal15, Pyxis
[30-35]	(**4**,11) **NGC6229, NGC5824, NGC5694, Whiting1**, NGC7006, Ter8, Arp2, Ter7, Rup106, Pyxis, Pal2	(3) NGC6101, NGC6934, Pal15
[35-300]	(**12**,15) **Laevens3, NGC7006, SagittariusII, Pal15, Pal14, Crater, Pal4, Pal3, Pyxis, NGC2419, Eridanus, AM1**, NGC6715, NGC5824, NGC5694	(4) Arp2, NGC6934, Pal2, Ter8

To more easily capture the similarity and differences in the morphology of the extra-tidal features surrounding Galactic globular clusters, we can group the latter on the basis of their orbital parameters[8] (see Appendix D for more details), as follows:

1. *disk clusters*: a cluster is classified as a disk cluster if $\arctan(z_{max}/R_{max}) \leq 10°$, where z_{max} and R_{max} are, respectively, the maximum height above or below the Galactic plane reached by its orbit in the last 5 Gyr, and its maximum in-plane distance from the Galactic center.
2. *inner clusters*: all clusters with $r_{max} \leq R_{\odot}$ which are not classified as disk clusters enter this group. Contrary to R_{max}, which is the maximum in-plane distance that a cluster reaches from the Galactic center, r_{max} is the maximum 3D distance, that is $r_{max} = \max(\sqrt{R^2 + z^2})$ with the maximum calculated over the whole cluster orbit.
3. *outer clusters*: all clusters with $r_{max} > R_{\odot}$ which are not classified as disk clusters enter this group.

By using the orbital radius of the Sun as the criterion for inner and outer clusters, debris from outer clusters can span the whole sky while inner clusters must be restricted in longitude and latitude. With these definitions, 21 clusters are disk clusters, 71 are inner clusters, and 67 are outer clusters (see Table D.1 in Appendix D). We emphasize that this classification does not aim to suggest any specific origin for these systems (for example whether they are in-situ or accreted, see Massari et al. 2019), but it is uniquely based on their current orbital characteristics, and helps capturing some of the properties in the extension (projected in to the sky) and shape of their extra-tidal material, as we discuss in the following.

3.3.1. Extra-tidal features originating from disk clusters: ribbons in the Galactic plane

Disk clusters are defined on the basis of the flatness of their orbits (i.e. on their z_{max}/R_{max} ratio). As a result, they typically are restricted to low latitudes, though the exact distribution depends on the relationship of their orbit to the solar radius. To specify, clusters whose R_{max} are interior to the Solar radius generate tidal debris in a limited range in longitude and latitude. For instance, the material associated to clusters as Ter 1, Ter 5, Ter 6, and Ter 9 has a disk-like shape and is completely confined to $|\ell| < 30°$ and $|b| < 10°$. If R_{max} is greater than the solar radius, material can cover the full longitude space, and most of the material will still appear at low latitudes. This is the case, for example, of BH 140, whose escaped stars diffusely occupy all longitudes and most of them are found at $|b| \leq 30°$, Pal 2 and Pal 10 whose extra-tidal stars have a very limited latitudinal extension and appear as ribbons in the sky. In the following, we discuss some of the structures associated to NGC 6121, Pal 2, and Pal 10. We refer the reader to Appendix C for the tidal structures generated by the whole set of disk clusters.

NGC 6121: With a current position at $x = -6.58$, $y = -0.28$ and $z = 0.53$ kpc, NGC 6121 is the closest globular cluster to the Sun in our list. This cluster has a remarkably planar orbit, with a maximal vertical excursion from the Galactic plane of

---

[8] We caution the reader that the classification of disk, inner and outer clusters made in this Section is based on the orbital parameters of the clusters, as found when their orbits are integrated in model PII. This classification may slightly change if model PI or model PII-0.3-SLOW were adopted.
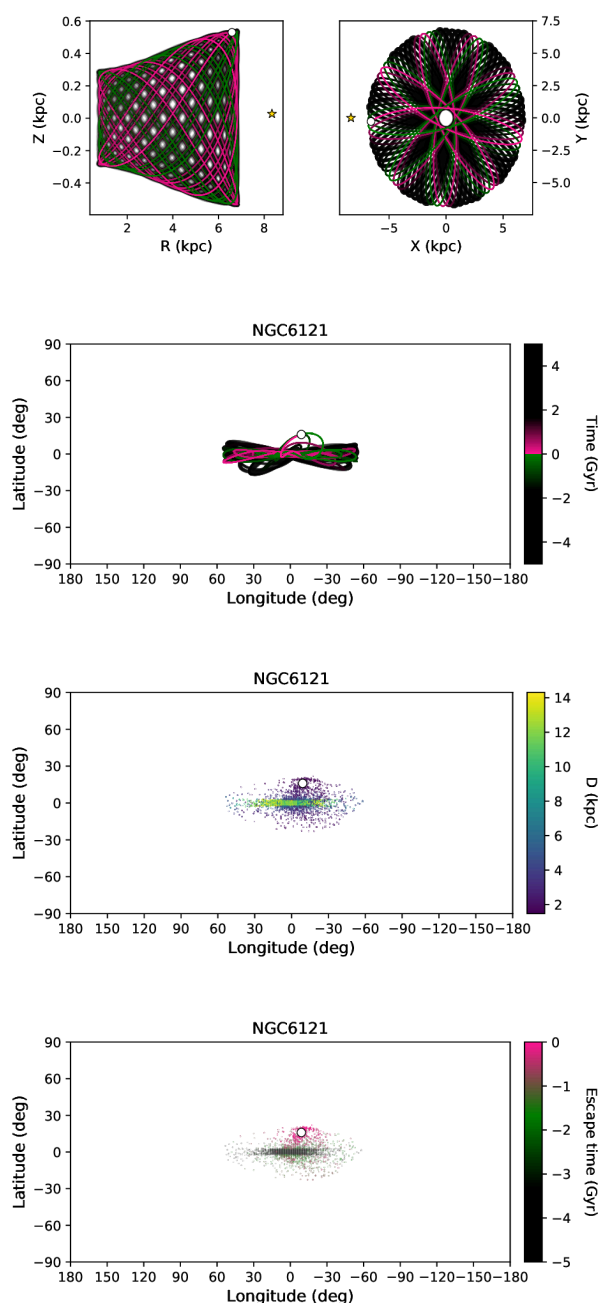
Fig. 6: *(Top-left panel):* Projection of the orbit of NGC 6121 in the meridional $R - z$ plane. Colors trace time, from 5 Gyr ago (negative values) to 5 Gyr forward in time (positive values). *(Top-right panel):* Projection of the orbit of NGC 6121 in the Galactic $x - y$ plane. *(Second row):* Projection of the NGC 6121 orbit for the past and future 5 Gyr, in the longitude-latitude plane. *(Third row):* Projection in the longitude-latitude plane of the extra-tidal material lost by NGC 6121. Colors indicate the average distance of the stripped material from the Sun. *(Bottom panel):* Projection in the longitude-latitude plane of the extra-tidal material lost by NGC 6121. Colors indicate the average time at which stellar particles become gravitationally unbound to the cluster, from 5 Gyr ago (negative time), to the current time (escape time = 0). In the bottom and middle panels, only the reference simulation without errors is shown, for better clarity. In all plots, the current position of the cluster is given by the white circle with a black edge color. The yellow star, when present, indicates the position of the Sun.

only 0.5 kpc (see Fig. 6), and an eccentricity $e = 0.80 \pm 0.01$, which makes it oscillate between an apo-center at $R_{max} = 6.81 \pm 0.02$ kpc and a peri-center at $R_{min} = 0.76 \pm 0.04$ kpc. Because this cluster lies inside the solar circle, its orbit is limited to a longitude interval from $-60°$ to $60°$; because the cluster currently lies very close to the Sun, and is at its highest height above the Galactic plane, the orbit forms a hook-like pattern in longitude-latitude space. This hook-like portion of the orbit, nearest to the cluster, is traced by the recently stripped tidal material (see Fig. 6), with a leading tail oriented mostly in a vertical direction in the (ℓ, b) plane, from the current cluster location, up to approximately $0°$ latitude. This portion of the stripped material lies at less than 2 kpc from the Sun, and it constitutes the nearest stream found in our simulations.

To our knowledge, no extra-tidal structure has been discovered yet around NGC 6121. Recently, Kundu et al. (2019) have used RR-Lyrae stars to trace the extra-tidal material around NGC 6121, without finding any clear evidence of structures. The current position of the cluster in the sky, at a latitude of roughly $20°$ and at a longitude close to $0°$, makes this search difficult due to the strong contamination of field disk stars, despite the fact that this portion of the stream should be very close to the Sun.

Pal 10 and Pal 2: Pal 10 and Pal 2 are two disk clusters whose orbit crosses the solar radius. While for Pal 10, the maximal in-plane distance R_{max} is approximately 12 kpc, in the case of Pal 2, the orbit can reach about 40 kpc from the Galactic center. The fact that both these clusters have a radial excursion of the orbit which is beyond the solar radius implies that their stripped stars can redistribute over the whole longitudinal range, thus also in the anti-center direction. The fact that both clusters have orbits confined close to the disk plane implies that the escaped material redistributes in very thin structures (i.e. confined in a limited latitude interval), which look like typical "ribbons" in the sky. Our models predict that both clusters are surrounded by a long stream of tidal material, which is however probably very difficult to identify because in both cases these extra-tidal stars are confined close to the Galactic plane. No tidal streams emanating from these two clusters, to our knowledge, have been identified in the observational data so far. Because the tidal structures associated to these two clusters have similar properties, in Fig. 7 we report only the case of Pal 10.

3.3.2. Extra-tidal features originating from inner clusters: bow-ties and more complex shapes

We have defined inner globular clusters as systems which are not disk clusters (their orbit is not confined close to the Galactic plane), but which are confined inside the solar radius. Seventy-one clusters are found in this category (see Table D.1). We discuss some of them in the following.

NGC 5946 & NGC 5986: These are inner-non disk clusters whose escaped stars redistribute in a characteristic "bow-tie" shape. These stars are all confined in a relatively narrow longitudinal range (typically within $-30°$ to $30°$). Towards the edges of the longitude interval, the distribution of extra-tidal stars tends to flare, whereas it instead shrinks at zero longitude. These trends can be explained as an effect of the projection of the orbits of these clusters in the (ℓ, b) plane. Moreover, because these clusters always stay in the inner region of the Galaxy, where the dynamical timescales are short, their orbit - and consequently
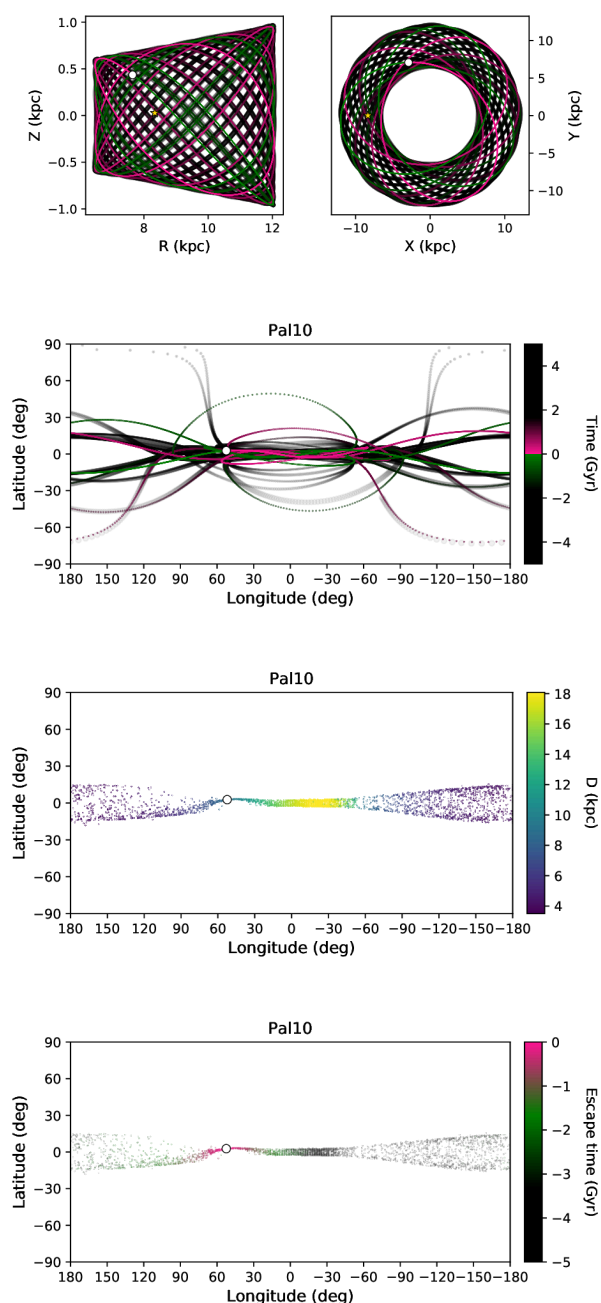
Fig. 7: Same as Fig. 6, but for the cluster Pal 10.

their stripped stars - can experience many disk crossings over the whole duration of the simulation, filling the whole (ℓ, b) space allowed by their orbital parameters. An example of such a distribution is given in Fig. 8 for the extra-tidal material associated to the cluster NGC 5986.

NGC 104: Then there are clusters like NGC 104 (47 Tuc) for which the morphology of the extra-tidal material takes more complex shapes. This cluster has an orbit confined inside the solar radius, but which, at its apocenter, can reach a distance of less than 1 kpc from the Sun (see Fig. 9). The projection of the past and future orbit in the (ℓ, b) plane gives rise to a kind of figure-of-eight shape, with the stars stripped more recently from the cluster tracing the portion of this shape which extends to negative latitudes. Our model of NGC 104 agrees with the conclu-
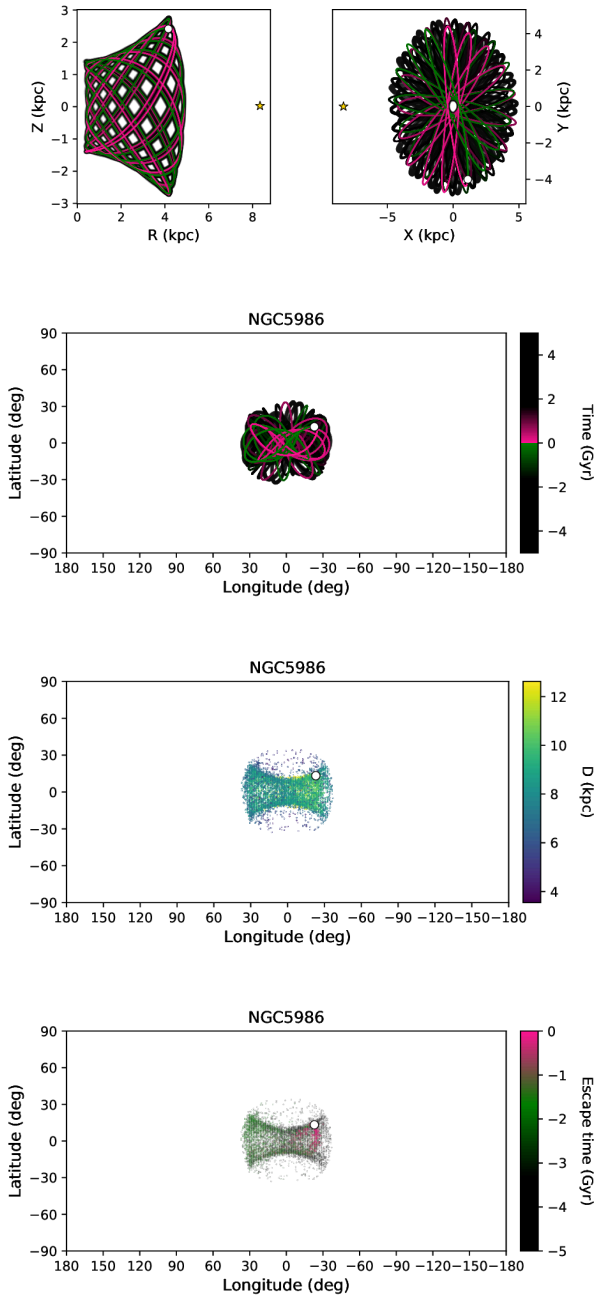
Fig. 8: Same as Fig. 6, but for the cluster NGC 5986.
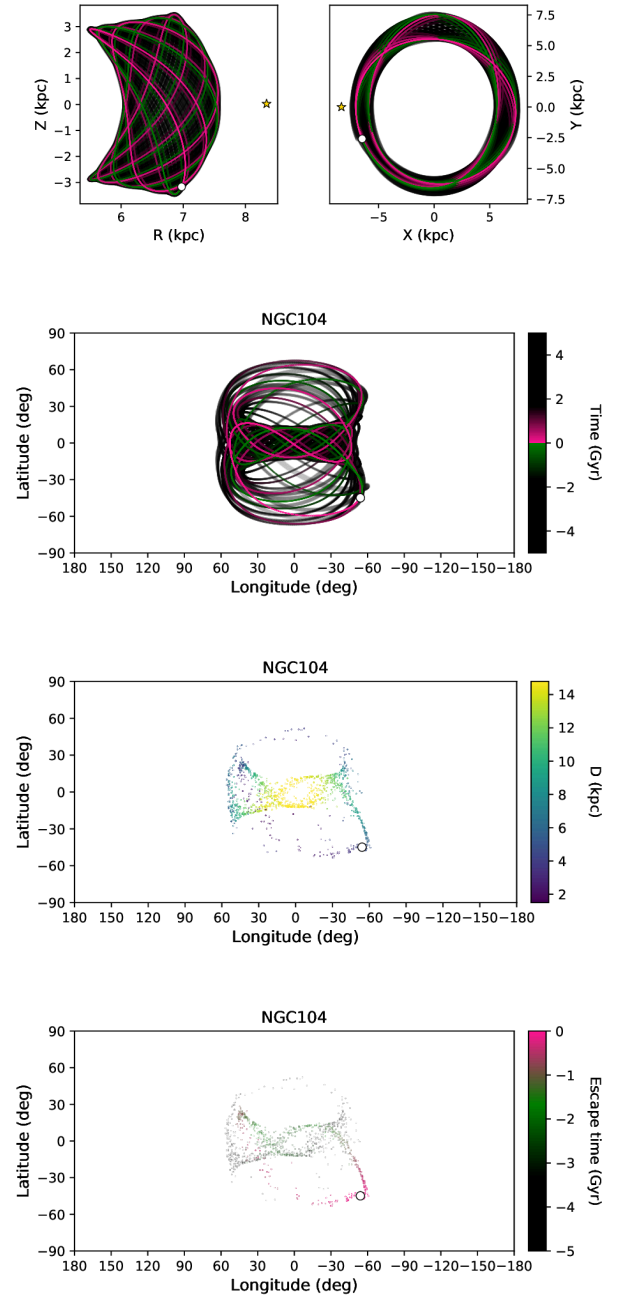
Fig. 9: Same as Fig. 6, but for the cluster NGC 104.

sions reached by Lane et al. (2012) who suggested that two clear tidal tails should emanate from this cluster, however, the orientation of these tails in the (ℓ, b) plane differs slightly in the two works. Lane et al. (2012)'s models suggest indeed that the leading tail of NGC 104 should extend a bit beyond $\ell < -70°$ (see Fig. 4 in their paper, as an example), while our model predicts a minimum longitude of about $-60°$. The exact comparison between these two works is however difficult, since the model of the Galactic potential, the distance to the Sun, proper motions and line-of-sight velocities of NGC 104 used in their study are different from ours. To date, clear tails around NGC 104 have not been found yet, with the most recent observational works pointing to the possibility of the presence of a diffuse extended halo-like structure around this cluster (see Piatti 2017). We note that we only find a more diffuse distribution of extra-tidal mate-

rial in the case of the PII-0.3-SLOW model. Additional work for comparing the current observational data with simulations will be needed to resolve this apparent discrepancy between theoretical predictions and observational findings.

Other shapes found in this category include "Easter eggs", which are generated by clusters whose orbits are confined to the innermost kpc of the Galaxy, and show significant variations in the z-coordinates—at least as large as those found in the radial direction. Among clusters whose extra-tidal material shows these peculiar shapes we find HP1, NGC 6093, NGC 6273, NGC 6293, NGC 6723, and NGC 6809.

3.3.3. Extra-tidal features originating from outer clusters: "canonical" tidal tails

Caveat: In this group, there are some elongated streams emanating from clusters as NGC 6715, Pal 12, Ter 7 and Ter 8, which are associated to the Sagittarius dwarf galaxy. We caution the reader that for these clusters the elongation and shape of the streams may be severely modified if the gravitational potential generated by the Sagittarius dwarf galaxy itself was included in the model. For completeness, we have decided to include these streams in the paper, and to report them in Appendix C. In future works, we plan to investigate how the inclusion of the Sagittarius dwarf may alter these streams, and possibly affect also those of other clusters, not necessarily associated to this dwarf galaxy.

Among the extra-tidal structures emanating from outer globular clusters, we find some of the most beautiful and elongated tidal tails, of which those associated to Pal 5 were the first to be discovered (Odenkirchen et al. 2001). In this category, we note the stream associated to the E 3 cluster that extends about 120° in longitude based on our models prediction; the thin stream emanating from IC 4499, which we predict to have an extension of about 150° in longitude. To list them, the finest and thinnest stellar streams are predicted from: AM 4, Arp 2, IC 4499, NGC 1261, NGC 3201, NGC 4590, NGC 5024, NGC 5053, NGC 5272, NGC 5466, NGC 5694, NGC 5824, NGC 5904, NGC 6101, NGC 6426, NGC 6584, NGC 6934, Pal 1, Pal 5, Pyxis, Rup 106, Sagittarius II, Ter 7, Ter 8, and Whiting 1.

Many of the above cited streams have been discovered and found also in observational data, but in many cases the extent of the tails, as predicted by our models, is larger. Of these observed streams, many tracks are available in the *galstreams* (Mateu 2022) library. In the following, we compare our model predictions to some of these tracks in the three different Galactic potentials adopted in this paper. More specifically, we compare the projected density distribution of the simulated stream to observations in the (ℓ, b), $(\ell, \mu_\ell \cos(b))$, (ℓ, μ_b) and (ℓ, D) planes. As for the projected density distributions derived from the models, we calculate them by taking into account all the 51 simulations realized for each cluster, that is both the reference simulation, and those realized by a Monte-Carlo sampling of the uncertainties. Overall, the agreement between models and observational data is excellent, in all Galactic models used. By looking at more extended regions in the sky than those covered by current observations, it should be however possible to better constrain the streams, and favor/disfavor some of these models.

NGC 3201: NGC 3201 is an outer cluster at a distance of about 4.7 kpc from the Sun. It has received much attention in the last couple of years, since the suggestion by Riley & Strigari (2020) that part of its tidal tails could be associated to the Gjöll stream, discovered by Ibata et al. (2019b). The association of Gjöll and NGC 3201 stream has been further confirmed by Hansen et al. (2020), on the basis of the similarity of the chemical abundances of stars in the Gjöll stream and in NGC 3201. More recently, Palau & Miralda-Escudé (2021) have conducted an extensive study of the tidal tails emanating from this cluster, discovering a long stream, which an overall length of 140° in the sky. Our models suggest that, in fact, the tails emanating from NGC 3201 may be even more extended than those found by Palau & Miralda-Escudé (2021). To further illustrate this point, in Fig. 10 we compare our model predictions to the tracks available for this stream in the *galstreams* library, and which are taken

from Ibata et al. (2021), from Palau & Miralda-Escudé (2021) and from the Gjöll stream, as reported by Ibata et al. (2021). All models represent very well the portion of the stream discovered so far, both in distribution of the stream in the sky, distance and proper motion spaces. Our models predict indeed that, for this cluster, the differences in the stream properties change very little with the mass model adopted. The most striking difference is found for the elongation of the stream at $\ell > 0$: in the case of the barred potential, the stream associated to NGC 3201 extends indeed to smaller values of ℓ (up to $\ell \sim 70°$) which are not reached in the case of the axisymmetric models. This portion of the stream is expected to be at distances greater than 20 kpc from the Sun (see bottom panels in Fig. 10).

NGC 4590: NGC 4590 (M 68) is an outer cluster at a current distance of about 10 kpc from the Sun. This cluster is surrounded by a very extended stream (Palau & Miralda-Escudé 2019; Ibata et al. 2021), a long portion of which is represented by the Fjörm stream discovered by Ibata et al. (2019b). The comparison between our model predictions and the tracks available in *galstreams* is shown in Fig. 11. Interestingly, and differently from the case of NGC 3201, not all the Galactic potentials adopted in this paper seem to represent equally well the stream distribution in the sky. While the axisymmetric models PI and PII predict generally a good match—with model PI describing the stream at positive longitudes even more accurately than model PII—the model PII-0.3-SLOW fails in reproducing the stream in its observed extension: the modeled stream in this case appears quite thick in the (ℓ, b) plane, and moreover much shorter than the stream found in the observational data. Interestingly, the axisymmetric models capture very well also the proper motions and distance-to-the-Sun trends as a function of longitude, as found by Ibata et al. (2021) (for Fjörm) and by Palau & Miralda-Escudé (2019), while the NGC 4590 as reported by Ibata et al. (2021) (and named "M68-I21" in Fig. 11) tends to be off in all models, and also off when compared to the other observational tracks. As suggested by Mateu (2022), it is possible that the stellar stream associated by Ibata et al. (2021) to NGC 4590 has indeed a different progenitor. Finally, the failure of the barred model to reproduce the extension of the NGC 4590 stream, and in particular Fjörm, can be due to the choice of the pattern speed adopted, or of the bar length. We will explore these topics in future work. Here we simply note that given the sensitivity of NGC 4590 stream to the choice of the barred potential, this stream is potentially very interesting for determining the parameters of this latter.

NGC 5466: NGC 5466 is another cluster known to be surrounded by a thin and very extended stream, as shown by Grillmair & Johnson (2006) and Belokurov et al. (2006). More recently, Jensen et al. (2021) have used Gaia DR2 data to study the stream, finding an extension of about 30 degrees on the sky and a somewhat different orientation than that suggested by Grillmair & Johnson (2006). Also Ibata et al. (2021) confirmed the existence of an elongated stream around this cluster, even if less extended than that found by Grillmair & Johnson (2006). In Fig. 12 we show the comparison of our model predictions to the tracks available in *galstreams*, taken from the works by Grillmair & Johnson (2006) and Ibata et al. (2021). The comparison is excellent for all the Galactic potentials used in this paper. We note that there is a slight offset between the modeled streams and the track by Ibata et al. (2021) in the $(\ell - D)$ plane (of about 1 kpc at a fixed longitude) which is maybe less evident for the case of
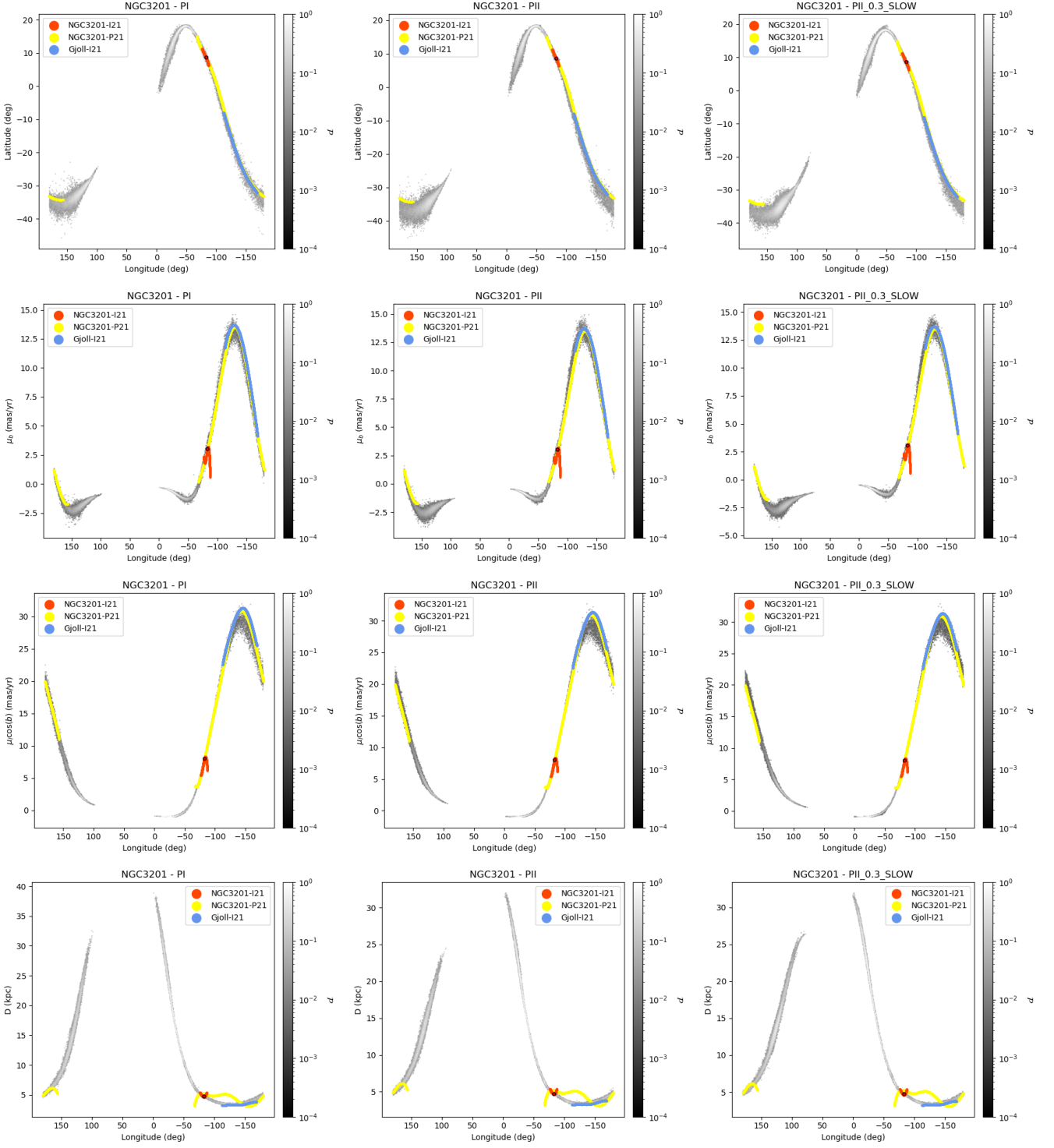
Fig. 10: *From top to bottom:* Projected density distribution of the NGC 3201 stream, as predicted by our simulations, in the (ℓ, b), (ℓ, μ_b), $(\ell, \mu_\ell \cos(b))$ and (ℓ, D) planes. The model predictions are shown for the three Galactic potentials PI (*left column*), PII (*middle column*), and PII-0.3-SLOW (*right column*) and are compared to the tracks available in the *galstreams* library for this cluster, and which are taken from Ibata et al. (2021) (NGC3201-I21, red lines), Palau & Miralda-Escudé (2021) (NGC3201-P21, yellow lines) and from Ibata et al. (2021), as for the Gjöll stream (Gjöll-I21, blue lines). For each panel, the color-bar indicates the two dimensional probability density quantified by taking into account all the particles from the 51 realizations which is then normalized to its maximum value. In all panels, the current position of the cluster is indicated by a red dot.

the PII-0.3-SLOW potential than in the axisymmetric cases. We emphasize that all our models predict that the stream should be more extended than that discovered so far in the observations: in particular, there is a portion of the leading tail at $0 < \ell < 42°$ not yet discovered, which lies at distances from the Sun closer or similar to that of the known stream.
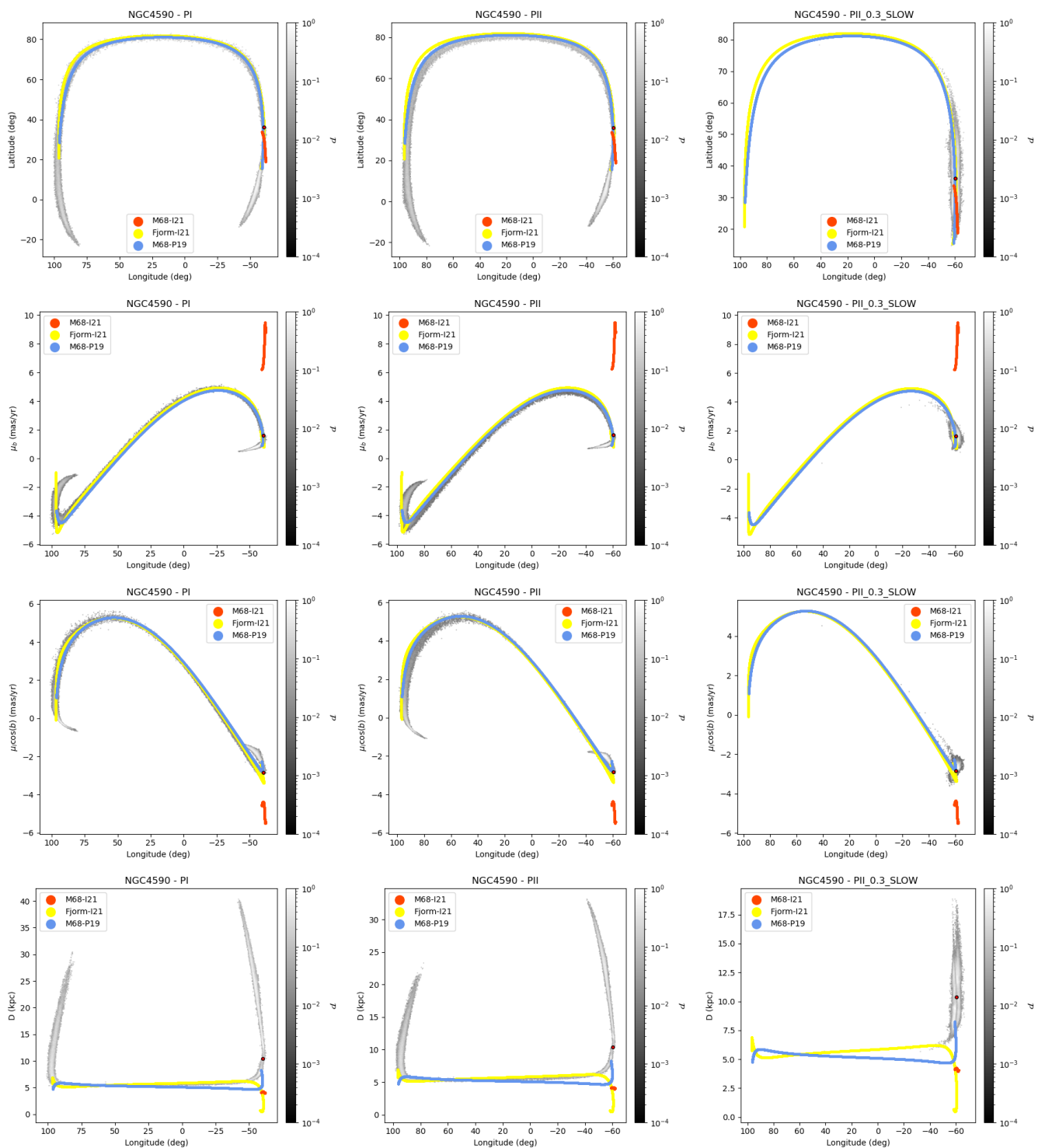
Fig. 11: Same as Fig. 10, for the NGC 4590 cluster. The tracks from come from the work by Palau & Miralda-Escudé (2019) (M68-P19, blue lines), Ibata et al. (2021) (M68-I21, red lines) and from Ibata et al. (2021) as for the Fjörm stream (Fjorm-I21, yellow lines).

Pal 5: After about 20 years from the discovery of its tidal tails (Odenkirchen et al. 2001, 2003), Pal 5 still represents the prototype cluster surrounded by thin and extended streams of stars. The extension, morphology, kinematics and chemical composition of its tails have been extensively studied, both observationally and numerically (Odenkirchen et al. 2002; Rockosi et al. 2002; Dehnen et al. 2004; Koch et al. 2004; Grillmair & Dionatos 2006a; Odenkirchen et al. 2009; Mastrobuono-Battisti et al. 2012; Küpper et al. 2015; Kuzma et al. 2015; Fritz & Kallivayalil 2015; Ibata et al. 2016; Ishigaki et al. 2016; Thomas et al. 2016; Koch & Côté 2017; Ibata et al. 2017; Pearson et al. 2017; Price-Whelan et al. 2019; Starkman et al. 2020; Bonaca et al. 2020b; Ibata et al. 2021; Phillips et al. 2022; Kuzma et al. 2022). In Fig. 13, we report the comparison of our model predictions to the tracks available for this cluster in *galstreams*, and which come from the work by Price-Whelan et al. (2019), Starkman
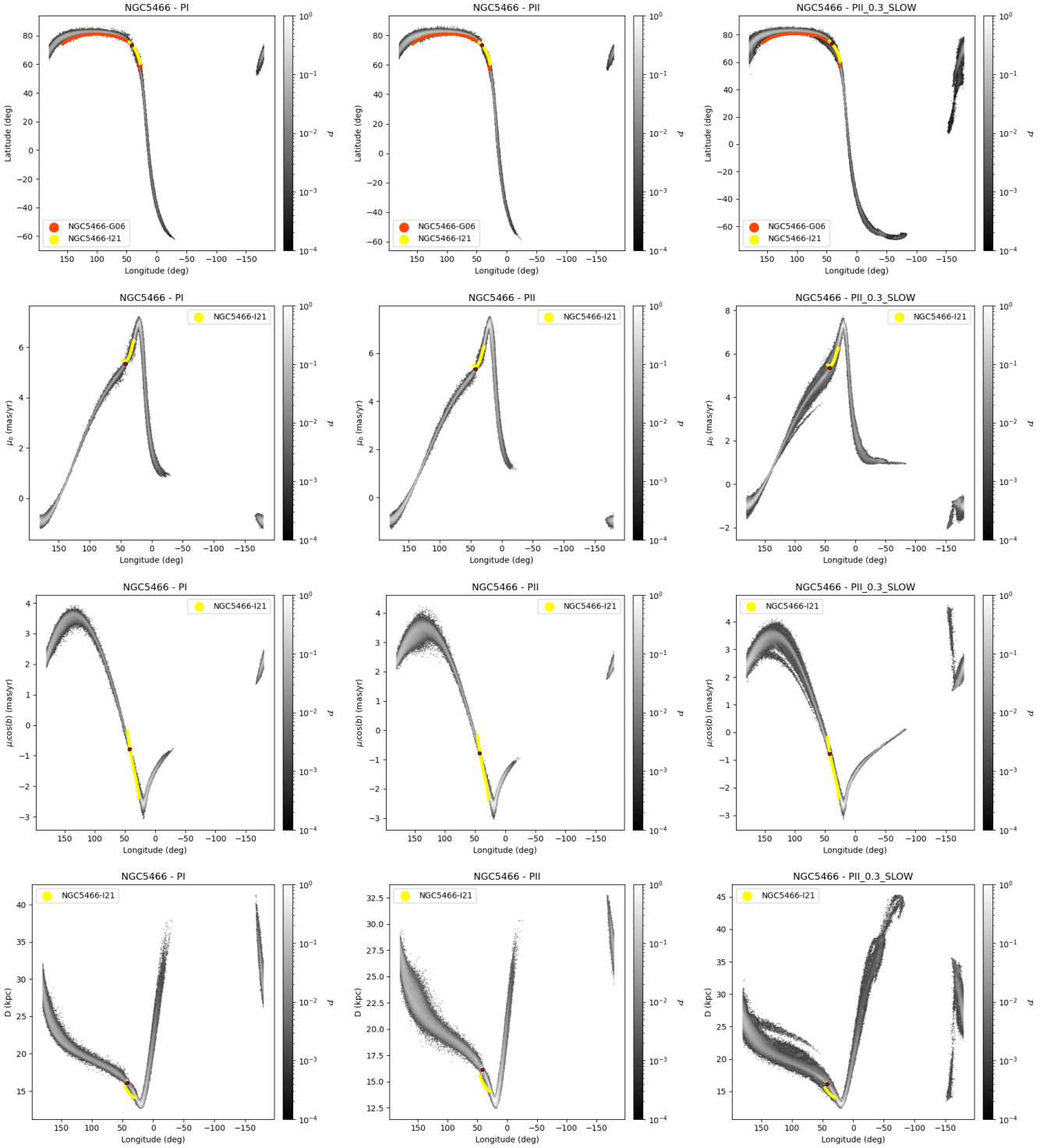
Fig. 12: Same as Figs. 10 and 11, for the case of the NGC 5466 cluster. Model predictions are compared to the tracks available in the *galstreams* library, and which come from the work by Grillmair & Johnson (2006) (red lines) and Ibata et al. (2021) (yellow lines). Note that proper motions and distances are available only for the NGC5466-I21 track. Notice that the variations in the streams, specifically the different stripes, originate from the errors considered in the simulations.

et al. (2020) and Ibata et al. (2021). Projected in the (ℓ, b) plane, the observed streams are in excellent agreement with the model predictions, for all the Galactic potentials adopted. Interestingly, all potentials suggest more extended streams than those discovered so far. In the case of the barred potential, we note that the prediction of the stream position in the sky at large angular dis-

tances from the cluster center is still highly uncertain. This is due to the uncertainties still affecting the current distance of Pal 5 to the Sun, combined with the impact of the rotating bar, which can be more or less efficient in perturbing the stream depending on the torques experienced by the latter at pericenter—which depend, in turn, on the orbital parameters of the cluster itself. Pear-

son et al. (2017) already explored the effect of a rotating bar on the extension and morphology of Pal 5 tails. While we can confirm the Pearson et al. (2017) findings, that both characteristics are affected by a rotating bar, we also emphasize that both the extension of the leading tail (i.e. portion of the stream at negative longitudes) and its morphology depend on the choice of the bar pattern speed. For example, we do not find a density drop in the leading tail as reported by Pearson et al. (2017). These authors adopted a higher bar pattern speed than the one adopted in this work ($\Omega_b = 60$ kms^{-1}kpc^{-1} for the example discussed in Fig. 2 of their work, right panel, while $\Omega_b = 38$ kms^{-1}kpc^{-1} in our PII-0.3-SLOW model). Additionally, taking into account the uncertainties in the cluster distance, proper motions and line-of-sight velocity is also important to have robust predictions on the stream characteristics. Some of our solutions, for example, predict a very extended leading tail, significantly more extended than those found for the axisymmetric potentials.

4. Conclusion

In this work, we have presented the first simulated catalogue of *all* Galactic globular clusters for which 6D phase space information, masses and sizes are available. A total of 159 globular clusters has been simulated in three Milky Way-like potentials, modeling the process of tidal stripping that these clusters have experienced over the past 5 Gyr. As a result, for all clusters we can predict the distribution of the extra-tidal material in the sky, their proper motions, distances to the Sun, and line-of-sight velocities. Errors on 6D-phase space information have been taken into account by generating, for each cluster, 50 complementary simulations, with a Monte-Carlo sampling of the uncertainties. This catalogue currently contains 24 327 simulations, for a total volume of about 370 Gb. It will be made publicly available[9], and it is intended to provide the community with an instrument to: have a complete view of the expected distribution of globular clusters tidal structures in the sky; to help the interpretation of recent and future discoveries; to support the search for new extra-tidal features in the data; to offer the community a repository of all these models to be compared to other theoretical and numerical predictions, which employ different Galactic potentials and/or gravity laws.

In this first paper, we have presented the distribution in the (ℓ, b) plane of all the simulated extra-tidal features. A striking result is the variety of extra-tidal shapes that globular clusters can give rise to. The canonical tidal tails "à la" Palomar 5 are only some of the multiple morphologies these structures can have. Ribbons, bow-ties, padlocks, halo-shapes are also common. This variety of shapes that these stripped stars can show in the sky depends on the characteristics of the cluster orbit, on its current position in the orbit itself and on distance of the extra-tidal material from the Sun. Any search for the left-overs of globular clusters in the field should take into account this richness of distributions and morphologies.

These simulations have also allowed us to derive an estimate of the expected mass of stars escaped from the clusters in the last 5 Gyr and now in the field. Although approximate, given the limitation of our models, our estimate of the mass lost from the Galactic globular cluster system over the last 5 Gyr is between $2-21\times10^6 M_\odot$ which is comparable to up to half of the total stellar mass found nowadays in the Galactic globular cluster system itself.

---

[9] All data will be available on a dedicated website (http://etidal-project.obspm.fr/)

This work is intended to be the first of a series which investigates the properties of globular clusters streams in a variety of realistic Galactic potentials, including the perturbations induced by close dwarf satellites (Sagittarius, Large and Small Magellanic Clouds), as well as more complex and time-varying distributions for the dark matter component.

References

Allen, C. & Santillan, A. 1991, Rev. Mexicana Astron. Astrofis., 22, 255
Amorisco, N. C., Gómez, F. A., Vegetti, S., & White, S. D. M. 2016, MNRAS, 463, L17
Astropy Collaboration, Price-Whelan, A. M., Sipőcz, B. M., et al. 2018, AJ, 156, 123
Astropy Collaboration, Robitaille, T. P., Tollerud, E. J., et al. 2013, A&A, 558, A33
Banik, N. & Bovy, J. 2019, MNRAS, 484, 2009
Banik, N., Bovy, J., Bertone, G., Erkal, D., & de Boer, T. J. L. 2021a, MNRAS, 502, 2364
Banik, N., Bovy, J., Bertone, G., Erkal, D., & de Boer, T. J. L. 2021b, J. Cosmology Astropart. Phys., 2021, 043
Baumgardt, H. & Hilker, M. 2018, MNRAS, 478, 1520
Baumgardt, H. & Sollima, S. 2017, MNRAS, 472, 744
Baumgardt, H. & Vasiliev, E. 2021, MNRAS, 505, 5957
Belokurov, V., Erkal, D., Evans, N. W., Koposov, S. E., & Deason, A. J. 2018, MNRAS, 478, 611
Belokurov, V., Evans, N. W., Irwin, M. J., Hewett, P. C., & Wilkinson, M. I. 2006, ApJ, 637, L29
Bianchini, P., Ibata, R., & Famaey, B. 2019, ApJ, 887, L12
Bland-Hawthorn, J. & Gerhard, O. 2016, ARA&A, 54, 529
Boldrini, P. & Vitral, E. 2021, MNRAS, 507, 1814
Bonaca, A., Conroy, C., Hogg, D. W., et al. 2020a, ApJ, 892, L37
Bonaca, A., Hogg, D. W., Price-Whelan, A. M., & Conroy, C. 2019, ApJ, 880, 38
Bonaca, A., Pearson, S., Price-Whelan, A. M., et al. 2020b, ApJ, 889, 70
Bovy, J. 2014, ApJ, 795, 95
Caldwell, N., Bonaca, A., Price-Whelan, A. M., Sesar, B., & Walker, M. G. 2020, AJ, 159, 287
Capuzzo Dolcetta, R., Di Matteo, P., & Miocchi, P. 2005, AJ, 129, 1906
Carlberg, R. G. 2018, ApJ, 861, 69
Carlberg, R. G. 2020, ApJ, 889, 107
Chemin, L., Renaud, F., & Soubiran, C. 2015, A&A, 578, A14
Chen, B., Stoughton, C., Smith, J. A., et al. 2001, ApJ, 553, 184
Combes, F., Leon, S., & Meylan, G. 1999, A&A, 352, 149
Dehnen, W., Odenkirchen, M., Grebel, E. K., & Rix, H.-W. 2004, AJ, 127, 2753
Di Matteo, P., Capuzzo Dolcetta, R., & Miocchi, P. 2005, Celestial Mechanics and Dynamical Astronomy, 91, 59
Di Matteo, P., Gómez, A., Haywood, M., et al. 2015, A&A, 577, A1
Di Matteo, P., Haywood, M., Lehnert, M. D., et al. 2019, A&A, 632, A4
Erkal, D., Belokurov, V., Bovy, J., & Sanders, J. L. 2016, MNRAS, 463, 102
Fall, S. M. & Zhang, Q. 2001, ApJ, 561, 751
Fritz, T. K. & Kallivayalil, N. 2015, ApJ, 811, 123
Gaia Collaboration, Brown, A. G. A., Vallenari, A., et al. 2018, A&A, 616, A1
Gaia Collaboration, Brown, A. G. A., Vallenari, A., et al. 2021a, A&A, 650, C3
Gaia Collaboration, Brown, A. G. A., Vallenari, A., et al. 2021b, A&A, 649, A1
Gaia Collaboration, Brown, A. G. A., Vallenari, A., et al. 2016, A&A, 595, A2
Gallart, C., Bernard, E. J., Brook, C. B., et al. 2019, Nature Astronomy, 3, 932
Garro, E., Minniti, D., Alessi, B., et al. 2022a, A&A, 659, A155
Garro, E., Minniti, D., Gómez, M., et al. 2022b, A&A, 658, A120
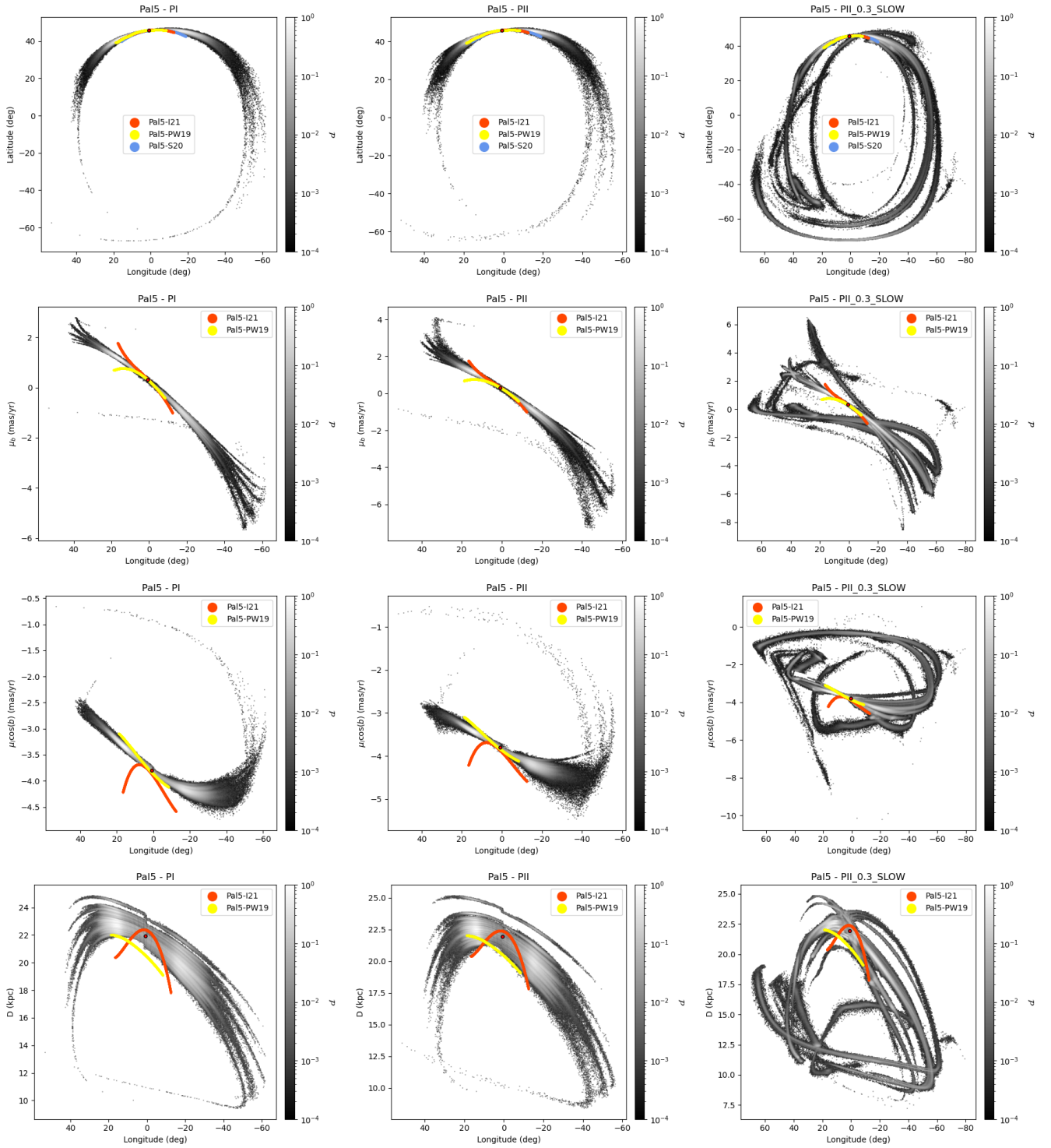
Fig. 13: Same as Figs. 10, 11 and 12, for the case of the Palomar 5 cluster. Model predictions are compared to the tracks available in the *galstreams* library, and which come from the work by Ibata et al. (2021) (red lines), Price-Whelan et al. (2019) (yellow-lines) and Starkman et al. (2020) (blue lines). Note that proper motions and distances are not available for the Pal5-S20 track.

Garro, E. R., Minniti, D., Gómez, M., et al. 2020, A&A, 642, L19
Garro, E. R., Minniti, D., Gómez, M., et al. 2021, A&A, 649, A86
Gnedin, O. Y. & Ostriker, J. P. 1997, ApJ, 474, 223
Gómez, A., Di Matteo, P., Schultheis, M., et al. 2018, A&A, 615, A100
Gran, F., Zoccali, M., Contreras Ramos, R., et al. 2019, A&A, 628, A45
Gran, F., Zoccali, M., Saviane, I., et al. 2022, MNRAS, 509, 4962
GRAVITY Collaboration, Abuter, R., Amorim, A., et al. 2018, A&A, 615, L15
Grillmair, C. J. 1998, in Astronomical Society of the Pacific Conference Series, Vol. 136, Galactic Halos, ed. D. Zaritsky, 45

Grillmair, C. J. 2022, ApJ, 929, 89
Grillmair, C. J. & Dionatos, O. 2006a, ApJ, 641, L37
Grillmair, C. J. & Dionatos, O. 2006b, ApJ, 643, L17
Grillmair, C. J., Freeman, K. C., Irwin, M., & Quinn, P. J. 1995, AJ, 109, 2553
Grillmair, C. J. & Johnson, R. 2006, ApJ, 639, L17
Hansen, T. T., Riley, A. H., Strigari, L. E., et al. 2020, ApJ, 901, 23
Harris, C. R., Millman, K. J., van der Walt, S. J., et al. 2020, Nature, 585, 357
Haywood, M., Di Matteo, P., Lehnert, M., et al. 2018, A&A, 618, A78

Heggie, D. & Hut, P. 2003, The Gravitational Million-Body Problem: A Multidisciplinary Approach to Star Cluster Dynamics (Cambridge University Press)

Helmi, A., Babusiaux, C., Koppelman, H. H., et al. 2018, Nature, 563, 85

Hunter, J. D. 2007, Computing in Science & Engineering, 9, 90

Ibata, R., Malhan, K., Martin, N., et al. 2021, ApJ, 914, 123

Ibata, R., Thomas, G., Famaey, B., et al. 2020, ApJ, 891, 161

Ibata, R. A., Bellazzini, M., Malhan, K., Martin, N., & Bianchini, P. 2019a, Nature Astronomy, 3, 667

Ibata, R. A., Lewis, G. F., Irwin, M. J., & Quinn, T. 2002, MNRAS, 332, 915

Ibata, R. A., Lewis, G. F., & Martin, N. F. 2016, ApJ, 819, 1

Ibata, R. A., Lewis, G. F., Thomas, G., Martin, N. F., & Chapman, S. 2017, ApJ, 842, 120

Ibata, R. A., Malhan, K., & Martin, N. F. 2019b, ApJ, 872, 152

Ibata, R. A., Malhan, K., Martin, N. F., & Starkenburg, E. 2018, ApJ, 865, 85

Irrgang, A., Wilcox, B., Tucker, E., & Schiefelbein, L. 2013, A&A, 549, A137

Ishigaki, M. N., Hwang, N., Chiba, M., & Aoki, W. 2016, ApJ, 823, 157

Jensen, J., Thomas, G., McConnachie, A. W., et al. 2021, MNRAS, 507, 1923

Johnston, K. V., Spergel, D. N., & Haydn, C. 2002, ApJ, 570, 656

Kaderali, S., Hunt, J. A. S., Webb, J. J., Price-Jones, N., & Carlberg, R. 2019, MNRAS, 484, L114

Katz, D., Sartoretti, P., Guerrier, A., et al. 2022, arXiv e-prints, arXiv:2206.05902

Keenan, D. W. & Innanen, K. A. 1975, AJ, 80, 290

Koch, A. & Côté, P. 2017, A&A, 601, A41

Koch, A., Grebel, E. K., Odenkirchen, M., Martínez-Delgado, D., & Caldwell, J. A. R. 2004, AJ, 128, 2274

Kruijssen, J. M. D., Pfeffer, J. L., Chevance, M., et al. 2020, MNRAS, 498, 2472

Kunder, A., Koch, A., Rich, R. M., et al. 2012, AJ, 143, 57

Kundu, R., Minniti, D., & Singh, H. P. 2019, MNRAS, 483, 1737

Küpper, A. H. W., Balbinot, E., Bonaca, A., et al. 2015, ApJ, 803, 80

Küpper, A. H. W., Kroupa, P., Baumgardt, H., & Heggie, D. C. 2010, MNRAS, 401, 105

Küpper, A. H. W., Lane, R. R., & Heggie, D. C. 2012, MNRAS, 420, 2700

Kuzma, P. B., Da Costa, G. S., Keller, S. C., & Maunder, E. 2015, MNRAS, 446, 3297

Kuzma, P. B., Ferguson, A. M. N., Varri, A. L., et al. 2022, MNRAS, 512, 315

Lane, R. R., Kiss, L. L., Lewis, G. F., et al. 2010, MNRAS, 406, 2732

Lane, R. R., Küpper, A. H. W., & Heggie, D. C. 2012, MNRAS, 423, 2845

Leon, S., Meylan, G., & Combes, F. 2000, A&A, 359, 907

Long, K. & Murali, C. 1992, ApJ, 397, 44

Malhan, K. & Ibata, R. A. 2019, MNRAS, 486, 2995

Malhan, K., Ibata, R. A., Carlberg, R. G., et al. 2019, ApJ, 886, L7

Malhan, K., Ibata, R. A., Goldman, B., et al. 2018a, MNRAS, 478, 3862

Malhan, K., Ibata, R. A., & Martin, N. F. 2018b, MNRAS, 481, 3442

Malhan, K., Yuan, Z., Ibata, R. A., et al. 2021, ApJ, 920, 51

Mancillas, B., Duc, P.-A., Combes, F., et al. 2019, A&A, 632, A122

Massari, D., Koppelman, H. H., & Helmi, A. 2019, A&A, 630, L4

Mastrobuono-Battisti, A., Di Matteo, P., Montuori, M., & Haywood, M. 2012, A&A, 546, L7

Mateu, C. 2022, arXiv e-prints, arXiv:2204.10326

Meylan, G. & Heggie, D. C. 1997, A&A Rev., 8, 1

Minniti, D., Fernández-Trincado, J. G., Gómez, M., et al. 2021a, A&A, 650, L11

Minniti, D., Geisler, D., Alonso-García, J., et al. 2017a, ApJ, 849, L24

Minniti, D., Hempel, M., Toledo, I., et al. 2011, A&A, 527, A81

Minniti, D., Palma, T., Camargo, D., et al. 2021b, A&A, 652, A129

Minniti, D., Palma, T., Dékány, I., et al. 2017b, ApJ, 838, L14

Minniti, D., Schlafly, E. F., Palma, T., et al. 2018, ApJ, 866, 12

Mirabal, N. & Bonaca, A. 2021, J. Cosmology Astropart. Phys., 2021, 033

Moni Bidin, C., Mauro, F., Geisler, D., et al. 2011, A&A, 535, A33

Montuori, M., Capuzzo-Dolcetta, R., Di Matteo, P., Lepinette, A., & Miocchi, P. 2007, ApJ, 659, 1212

Murali, C. & Weinberg, M. D. 1997a, MNRAS, 291, 717

Murali, C. & Weinberg, M. D. 1997b, MNRAS, 288, 749

Naik, A. P., Evans, N. W., Puchwein, E., Zhao, H., & Davis, A. C. 2020, Phys. Rev. D, 102, 084066

Navarrete, C., Belokurov, V., & Koposov, S. E. 2017, ApJ, 841, L23

Nie, J., Tian, H., Li, J., et al. 2022, ApJ, 930, 23

Odenkirchen, M., Grebel, E. K., Dehnen, W., Rix, H.-W., & Cudworth, K. M. 2002, AJ, 124, 1497

Odenkirchen, M., Grebel, E. K., Dehnen, W., et al. 2003, AJ, 126, 2385

Odenkirchen, M., Grebel, E. K., Kayser, A., Rix, H.-W., & Dehnen, W. 2009, AJ, 137, 3378

Odenkirchen, M., Grebel, E. K., Rockosi, C. M., et al. 2001, ApJ, 548, L165

Oh, K. S. & Lin, D. N. C. 1992, ApJ, 386, 519

Oh, K. S., Lin, D. N. C., & Aarseth, S. J. 1992, ApJ, 386, 506

Palau, C. G. & Miralda-Escudé, J. 2019, MNRAS, 488, 1535

Palau, C. G. & Miralda-Escudé, J. 2021, MNRAS, 504, 2727

Pearson, S., Price-Whelan, A. M., & Johnston, K. V. 2017, Nature Astronomy, 1, 633

Phillips, S. G., Schiavon, R. P., Mackereth, J. T., et al. 2022, MNRAS, 510, 3727

Piatti, A. E. 2017, ApJ, 846, L10

Piatti, A. E. 2018, MNRAS, 473, 492

Piatti, A. E. 2021, MNRAS, 505, 3033

Piatti, A. E. 2022, MNRAS, 509, 3709

Piatti, A. E. & Carballo-Bello, J. A. 2019, MNRAS, 485, 1029

Piatti, A. E. & Carballo-Bello, J. A. 2020, A&A, 637, L2

Piatti, A. E., Carballo-Bello, J. A., Mora, M. D., et al. 2020, A&A, 643, A15

Piatti, A. E. & Fernández-Trincado, J. G. 2020, A&A, 635, A93

Piatti, A. E., Mestre, M. F., Carballo-Bello, J. A., et al. 2021, A&A, 646, A176

Pouliasis, E., Di Matteo, P., & Haywood, M. 2017, A&A, 598, A66

Price-Whelan, A. M., Mateu, C., Iorio, G., et al. 2019, AJ, 158, 223

Reid, M. J., Menten, K. M., Brunthaler, A., et al. 2014, ApJ, 783, 130

Riley, A. H. & Strigari, L. E. 2020, MNRAS, 494, 983

Rockosi, C. M., Odenkirchen, M., Grebel, E. K., et al. 2002, AJ, 124, 349

Sanders, J. L. & Binney, J. 2013, MNRAS, 433, 1813

Sanders, J. L., Bovy, J., & Erkal, D. 2016, MNRAS, 457, 3817

Schönrich, R., Binney, J., & Dehnen, W. 2010, MNRAS, 403, 1829

Shen, J., Rich, R. M., Kormendy, J., et al. 2010, ApJ, 720, L72

Shipp, N., Drlica-Wagner, A., Balbinot, E., et al. 2018, ApJ, 862, 114

Shipp, N., Price-Whelan, A. M., Tavangar, K., Mateu, C., & Drlica-Wagner, A. 2020, AJ, 160, 244

Siegal-Gaskins, J. M. & Valluri, M. 2008, ApJ, 681, 40

Sofue, Y. 2012, PASJ, 64, 75

Sollima, A., Martínez-Delgado, D., Valls-Gabaud, D., & Peñarrubia, J. 2011, ApJ, 726, 47

Starkman, N., Bovy, J., & Webb, J. J. 2020, MNRAS, 493, 4978

Thomas, G. F., Famaey, B., Ibata, R., et al. 2018, A&A, 609, A44

Thomas, G. F., Ibata, R., Famaey, B., Martin, N. F., & Lewis, G. F. 2016, MNRAS, 460, 2711

Thomas, G. F., Jensen, J., McConnachie, A., et al. 2020, ApJ, 902, 89

Vasiliev, E. & Baumgardt, H. 2021, MNRAS, 505, 5978

Vasiliev, E., Belokurov, V., & Erkal, D. 2021, MNRAS, 501, 2279

Vesperini, E. & Heggie, D. C. 1997, MNRAS, 289, 898

Vitral, E. & Boldrini, P. 2022, A&A, 667, A112

Webb, J. J. & Bovy, J. 2019, MNRAS, 485, 5929

Wegg, C. & Gerhard, O. 2013, MNRAS, 435, 1874

Wegg, C., Gerhard, O., & Portail, M. 2015, MNRAS, 450, 4050

Yim, K.-J. & Lee, H. M. 2002, Journal of Korean Astronomical Society, 35, 75

Yuan, Z., Malhan, K., Sestito, F., et al. 2022, The Astrophysical Journal, 930, 103

Zhang, S., Mackey, D., & Da Costa, G. S. 2022, MNRAS[arXiv:2111.09072]

Appendix A: Additional Table

Table A.1: Current positions in the sky, proper motions, line-of-sight velocities, distances and relative uncertainties, masses and half-mass radii of all globular clusters analyzed in this study.

Cluster	D kpc	err D kpc	α degrees	δ degrees	μ_α mas/yr	err μ_α mas/yr	μ_δ mas/yr	err μ_δ mas/yr	v$_{\ell os}$ km/s	err v$_{\ell os}$ km/s	M_{GC} $M_\odot$	r_h pc
2MASS-GC01	3.37	0.62	272.0909	-19.8297	-1.121	0.296	-1.881	0.235	-31.28	0.50	35100	4.70
2MASS-GC02	5.50	0.44	272.4021	-20.7789	4.000	0.900	-4.700	0.800	-237.75	10.10	15800	2.85
AM1	118.91	3.40	58.7596	-49.6153	0.291	0.107	-0.177	0.086	118.00	14.14	19200	19.86
AM4	29.01	0.94	209.0891	-27.1652	-0.291	0.445	-2.512	0.344	151.19	2.85	756	15.00
Arp2	28.73	0.34	292.1838	-30.3556	-2.331	0.031	-1.475	0.029	122.64	0.29	37000	18.45
BH140	4.81	0.25	193.4729	-67.1773	-14.848	0.024	1.224	0.024	90.30	0.35	59900	9.53
BH261	6.12	0.26	273.5275	-28.6350	3.566	0.043	-3.590	0.037	-45.00	15.00	22000	4.66
Crater	147.23	4.27	174.0687	-10.8771	-0.059	0.125	-0.116	0.116	148.10	0.65	10800	25.74
Djor1	9.88	0.65	266.8696	-33.0664	-4.693	0.046	-8.468	0.041	-359.18	1.64	79700	5.57
Djor2	8.76	0.18	270.4544	-27.8258	0.662	0.042	-2.983	0.037	-149.75	1.10	125000	5.16
E3	7.88	0.25	140.2378	-77.2819	-2.727	0.027	7.083	0.027	11.71	0.34	2890	6.14
ESO280-SC06	20.95	0.65	272.2750	-46.4233	-0.688	0.039	-2.777	0.033	93.20	0.34	7800	9.65
ESO452-SC11	7.39	0.20	249.8542	-28.3992	-1.423	0.031	-6.472	0.030	16.37	0.44	8260	3.68
Eridanus	84.68	2.89	66.1856	-21.1868	0.510	0.039	-0.301	0.041	-23.15	0.73	11600	17.91
FSR1716	7.43	0.27	242.6250	-53.7489	-4.354	0.033	-8.832	0.031	-30.70	0.98	64300	5.16
FSR1735	9.08	0.53	253.0442	-47.0581	-4.439	0.054	-1.534	0.048	-69.85	4.88	72300	2.97
FSR1758	11.09	0.74	262.8000	-39.8080	-2.881	0.026	2.519	0.025	227.31	0.59	628000	17.04
HP1	7.00	0.14	262.7717	-29.9817	2.523	0.039	-10.093	0.037	39.76	1.22	124000	3.74
IC1257	26.59	1.43	261.7854	-7.0931	-1.007	0.040	-1.492	0.032	-137.97	2.04	18100	5.54
IC1276	4.55	0.25	272.6844	-7.2076	-2.553	0.026	-4.568	0.026	155.06	0.69	73900	5.21
IC4499	18.89	0.25	225.0772	-82.2138	0.466	0.025	-0.489	0.025	38.41	0.31	155000	14.96
Laevens3	61.77	1.65	316.7267	14.9805	0.172	0.101	-0.666	0.080	-70.30	0.82	2120	9.46
Liller1	8.06	0.34	263.3523	-33.3896	-5.403	0.109	-7.431	0.077	60.36	2.44	915000	2.01
Lynga7	7.90	0.16	242.7652	-55.3178	-3.851	0.027	-7.050	0.027	17.86	0.83	79600	5.16
NGC104	4.52	0.03	6.0238	-72.0813	5.252	0.021	-2.551	0.021	-17.45	0.16	895000	6.30
NGC1261	16.40	0.19	48.0675	-55.2162	1.596	0.025	-2.064	0.025	71.34	0.21	182000	5.23
NGC1851	11.95	0.13	78.5282	-40.0466	2.145	0.024	-0.650	0.024	321.40	1.55	318000	2.90
NGC1904	13.08	0.18	81.0458	-24.5244	2.469	0.025	-1.594	0.025	205.76	0.20	139000	3.21
NGC2298	9.83	0.17	102.2475	-36.0053	3.320	0.025	-2.175	0.026	147.15	0.57	55800	3.31
NGC2419	88.47	2.40	114.5353	38.8819	0.007	0.028	-0.523	0.026	-21.10	0.31	971000	26.50
NGC2808	10.06	0.11	138.0129	-64.8635	0.994	0.024	0.273	0.024	103.57	0.27	864000	3.89
NGC288	8.99	0.09	13.1885	-26.5826	4.164	0.024	-5.705	0.024	-44.45	0.13	93400	8.37
NGC3201	4.74	0.04	154.4034	-46.4125	8.348	0.022	-1.958	0.022	493.65	0.21	160000	6.78
NGC362	8.83	0.10	15.8094	-70.8488	6.694	0.025	-2.535	0.024	223.12	0.28	284000	3.79
NGC4147	18.54	0.21	182.5263	18.5426	-1.707	0.027	-2.090	0.027	179.35	0.31	39000	4.03
NGC4372	5.71	0.21	186.4391	-72.6591	-6.409	0.024	3.297	0.024	75.59	0.30	198000	8.53
NGC4590	10.40	0.10	189.8666	-26.7441	-2.739	0.024	1.779	0.024	-93.11	0.18	122000	7.58
NGC4833	6.48	0.08	194.8913	-70.8765	-8.377	0.025	-0.963	0.025	201.99	0.40	206000	4.76
NGC5024	18.50	0.18	198.2302	18.1682	-0.133	0.024	-1.331	0.024	-63.37	0.25	455000	10.18
NGC5053	17.54	0.23	199.1129	17.7003	-0.329	0.025	-1.213	0.025	42.82	0.25	74200	17.31
NGC5139	5.43	0.05	201.6970	-47.4795	-3.250	0.022	-6.746	0.022	232.78	0.21	3640000	10.36
NGC5272	10.18	0.08	205.5484	28.3773	-0.152	0.023	-2.670	0.022	-147.20	0.27	406000	6.34
NGC5286	11.10	0.14	206.6117	-51.3742	0.198	0.025	-0.153	0.025	62.38	0.40	353000	3.79
NGC5466	16.12	0.16	211.3637	28.5344	-5.342	0.025	-0.822	0.024	106.82	0.20	59800	14.03
NGC5634	25.96	0.62	217.4053	-5.9764	-1.692	0.027	-1.478	0.026	-16.07	0.60	228000	7.39
NGC5694	34.84	0.74	219.9012	-26.5388	-0.464	0.029	-1.105	0.029	-139.55	0.49	317000	4.86
NGC5824	31.71	0.60	225.9942	-33.0681	-1.189	0.026	-2.234	0.026	-25.24	0.52	762000	6.51
NGC5897	12.55	0.24	229.3517	-21.0101	-5.422	0.025	-3.393	0.025	101.31	0.22	157000	10.99
NGC5904	7.48	0.06	229.6384	2.0810	4.086	0.023	-9.870	0.023	53.50	0.25	394000	5.68
NGC5927	8.27	0.11	232.0029	-50.6730	-5.056	0.025	-3.217	0.025	-104.09	0.28	275000	5.28
NGC5946	9.64	0.51	233.8691	-50.6597	-5.331	0.028	-1.657	0.027	137.60	0.94	93100	2.59
NGC5986	10.54	0.13	236.5125	-37.7864	-4.192	0.026	-4.568	0.026	101.18	0.43	334000	4.25
NGC6093	10.34	0.12	244.2600	-22.9761	-2.934	0.027	-5.578	0.026	10.93	0.39	338000	2.62
NGC6101	14.45	0.19	246.4505	-72.2022	1.756	0.024	-0.258	0.025	366.33	0.32	178000	14.06
NGC6121	1.85	0.02	245.8967	-26.5257	-12.514	0.023	-19.022	0.023	71.21	0.15	87100	3.69
NGC6139	10.04	0.45	246.9185	-38.8488	-6.081	0.027	-2.711	0.026	24.41	0.95	323000	2.47
NGC6144	8.15	0.13	246.8078	-26.0235	-1.744	0.026	-2.607	0.026	194.79	0.58	79200	4.91
NGC6171	5.63	0.08	248.1328	-13.0538	-1.939	0.025	-5.979	0.025	-34.71	0.18	74900	3.94
NGC6205	7.42	0.08	250.4218	36.4599	-3.149	0.023	-2.574	0.023	-244.90	0.30	545000	5.26
NGC6218	5.11	0.05	251.8091	-1.9485	-0.191	0.024	-6.802	0.024	-41.67	0.14	107000	4.05
NGC6229	30.11	0.47	251.7452	47.5278	-1.171	0.026	-0.467	0.027	-137.89	0.71	286000	4.41
NGC6235	11.94	0.38	253.3557	-22.1774	-3.931	0.027	-7.587	0.027	126.68	0.33	107000	4.78
NGC6254	5.07	0.06	254.2877	-4.1003	-4.758	0.024	-6.597	0.024	74.21	0.23	205000	4.81
NGC6256	7.24	0.29	254.8861	-37.1210	-3.715	0.031	-1.637	0.030	-99.75	0.66	125000	4.82
NGC6266	6.41	0.10	255.3042	-30.1134	-4.978	0.026	-2.947	0.026	-73.98	0.67	610000	2.43
NGC6273	8.34	0.16	255.6575	-26.2680	-3.249	0.026	1.660	0.025	145.54	0.59	697000	4.21
NGC6284	14.21	0.42	256.1201	-24.7648	-3.200	0.029	-2.002	0.028	28.62	0.73	129000	3.78
NGC6287	7.93	0.37	256.2889	-22.7080	-5.010	0.029	-1.883	0.028	-294.74	1.65	145000	3.65
NGC6293	9.19	0.28	257.5425	-26.5821	0.870	0.028	-4.326	0.028	-143.66	0.39	205000	4.05
NGC6304	6.15	0.15	258.6344	-29.4620	-4.070	0.029	-1.088	0.028	-108.62	0.39	126000	4.26
NGC6316	11.15	0.39	259.1554	-28.1401	-4.969	0.031	-4.592	0.030	99.65	0.84	318000	4.77
NGC6325	7.53	0.32	259.4963	-23.7677	-8.289	0.030	-9.000	0.029	29.54	0.58	58900	2.05

Table A.1: continued.

Cluster	D kpc	err D kpc	α degrees	δ degrees	μ_α mas/yr	err μ_α mas/yr	μ_δ mas/yr	err μ_δ mas/yr	$v_{\ell os}$ km/s	err $v_{\ell os}$ km/s	M $M_\odot$	r_h pc
NGC6333	8.30	0.14	259.7991	-18.5163	-2.180	0.026	-3.222	0.026	310.75	2.12	323000	4.17
NGC6341	8.50	0.07	259.2808	43.1359	-4.935	0.024	-0.625	0.024	-120.55	0.27	352000	4.49
NGC6342	8.01	0.23	260.2916	-19.5877	-2.903	0.027	-7.116	0.026	115.75	0.90	42200	2.06
NGC6352	5.54	0.07	261.3713	-48.4222	-2.158	0.025	-4.447	0.025	-125.63	1.01	64700	4.56
NGC6355	8.65	0.22	260.9935	-26.3528	-4.738	0.031	-0.572	0.030	-195.85	0.55	101000	3.55
NGC6356	15.66	0.92	260.8958	-17.8130	-3.750	0.026	-3.392	0.026	48.18	1.82	600000	6.86
NGC6362	7.65	0.07	262.9791	-67.0483	-5.506	0.024	-4.763	0.024	-14.58	0.18	127000	7.23
NGC6366	3.44	0.05	261.9344	-5.0799	-0.332	0.025	-5.160	0.024	-120.65	0.19	37600	5.56
NGC6380	9.61	0.30	263.6186	-39.0695	-2.183	0.031	-3.233	0.030	-1.48	0.73	334000	4.40
NGC6388	11.17	0.16	264.0718	-44.7355	-1.316	0.026	-2.709	0.026	83.11	0.45	1250000	4.34
NGC6397	2.48	0.02	265.1754	-53.6743	3.260	0.023	-17.664	0.022	18.51	0.08	96600	3.90
NGC6401	8.06	0.24	264.6522	-23.9096	-2.748	0.035	1.444	0.034	-105.44	2.50	145000	3.28
NGC6402	9.14	0.25	264.4007	-3.2459	-3.590	0.025	-5.059	0.025	-60.71	0.45	592000	5.14
NGC6426	20.71	0.35	266.2280	3.1701	-1.828	0.026	-2.999	0.026	-210.51	0.51	71700	8.00
NGC6440	8.25	0.24	267.2202	-20.3604	-1.187	0.036	-4.020	0.035	-69.39	0.93	489000	2.14
NGC6441	12.73	0.16	267.5544	-37.0514	-2.551	0.028	-5.348	0.028	18.47	0.56	1320000	3.47
NGC6453	10.07	0.22	267.7155	-34.5985	0.203	0.036	-5.934	0.037	-99.23	1.24	165000	3.85
NGC6496	9.64	0.15	269.7654	-44.2659	-3.060	0.027	-9.271	0.026	-134.72	0.26	68900	6.42
NGC6517	9.23	0.56	270.4608	-8.9588	-1.551	0.029	-4.470	0.028	-35.06	1.65	195000	2.29
NGC6522	7.29	0.21	270.8920	-30.0340	2.566	0.039	-6.438	0.036	-15.23	0.49	211000	3.08
NGC6528	7.83	0.24	271.2067	-30.0558	-2.157	0.043	-5.649	0.039	211.86	0.43	56700	2.73
NGC6535	6.36	0.12	270.9604	-0.2976	-4.214	0.027	-2.939	0.026	-214.85	0.46	21900	3.65
NGC6539	8.16	0.39	271.2073	-7.5859	-6.896	0.026	-3.537	0.026	35.19	0.50	209000	5.18
NGC6540	5.91	0.27	271.5357	-27.7653	-3.702	0.032	-2.791	0.032	-16.50	0.78	34500	5.32
NGC6541	7.61	0.10	272.0098	-43.7149	0.287	0.025	-8.847	0.025	-163.97	0.46	293000	4.34
NGC6544	2.58	0.06	271.8338	-24.9982	-2.304	0.031	-18.604	0.030	-38.46	0.67	91400	2.07
NGC6553	5.33	0.13	272.3153	-25.9078	0.344	0.030	-0.454	0.029	-0.27	0.34	285000	4.56
NGC6558	7.47	0.29	272.5740	-31.7645	-1.720	0.036	-4.144	0.034	-195.12	0.73	26500	1.70
NGC6569	10.53	0.26	273.4117	-31.8269	-4.125	0.028	-7.354	0.028	-49.83	0.50	236000	3.85
NGC6584	13.61	0.17	274.6566	-52.2158	-0.090	0.026	-7.202	0.025	260.64	1.58	102000	5.37
NGC6624	8.02	0.11	275.9188	-30.3610	0.124	0.029	-6.936	0.029	54.79	0.40	156000	3.69
NGC6626	5.37	0.10	276.1370	-24.8698	-0.278	0.028	-8.922	0.028	11.11	0.60	299000	2.26
NGC6637	8.90	0.10	277.8463	-32.3481	-5.034	0.028	-5.832	0.028	47.48	1.00	155000	3.69
NGC6638	9.78	0.34	277.7337	-25.4975	-2.518	0.029	-4.076	0.029	8.63	2.00	118000	2.20
NGC6642	8.05	0.20	277.9760	-23.4756	-0.173	0.030	-3.892	0.030	-60.61	1.35	34400	1.51
NGC6652	9.46	0.14	278.9401	-32.9907	-5.484	0.027	-4.274	0.027	-95.37	0.86	48100	1.96
NGC6656	3.30	0.04	279.0998	-23.9047	9.851	0.023	-5.617	0.023	-148.72	0.78	476000	5.29
NGC6681	9.36	0.11	280.8032	-32.2921	1.431	0.027	-4.744	0.026	216.62	0.84	116000	2.89
NGC6712	7.38	0.24	283.2680	-8.7060	3.363	0.027	-4.436	0.027	-107.45	0.29	96300	3.21
NGC6715	26.28	0.33	283.7639	-30.4799	-2.679	0.025	-1.387	0.025	143.13	0.43	1780000	5.20
NGC6717	7.52	0.13	283.7752	-22.7015	-3.125	0.027	-5.008	0.027	30.25	0.90	35800	4.23
NGC6723	8.27	0.10	284.8881	-36.6322	1.028	0.025	-2.418	0.025	-94.39	0.26	177000	5.06
NGC6749	7.59	0.21	286.3141	1.8998	-2.829	0.028	-6.006	0.027	-58.44	0.96	211000	7.09
NGC6752	4.12	0.04	287.7171	-59.9846	-3.161	0.022	-4.027	0.022	-26.01	0.12	276000	5.27
NGC6760	8.41	0.43	287.8003	1.0305	-1.107	0.026	-3.615	0.026	-2.37	1.27	269000	5.22
NGC6779	10.43	0.14	289.1482	30.1835	-2.018	0.025	1.618	0.025	-136.97	0.45	186000	4.51
NGC6809	5.35	0.05	294.9988	-30.9647	-3.432	0.024	-9.311	0.024	174.70	0.17	193000	6.95
NGC6838	4.00	0.05	298.4437	18.7792	-3.416	0.025	-2.656	0.024	-22.72	0.20	65600	6.57
NGC6864	20.52	0.45	301.5198	-21.9212	-0.598	0.026	-2.810	0.026	-189.08	1.12	370000	2.96
NGC6934	15.72	0.17	308.5474	7.4045	-2.655	0.026	-4.689	0.026	-406.22	0.73	136000	5.16
NGC6981	16.66	0.18	313.3654	-12.5373	-1.274	0.026	-3.361	0.026	-331.39	1.47	68900	5.96
NGC7006	39.32	0.56	315.3726	16.1873	-0.128	0.027	-0.633	0.027	-383.47	0.73	136000	6.99
NGC7078	10.71	0.10	322.4930	12.1670	-0.659	0.024	-3.803	0.024	-106.84	0.30	633000	4.30
NGC7089	11.69	0.11	323.3626	-0.8233	3.435	0.025	-2.159	0.024	-3.78	0.30	620000	4.77
NGC7099	8.46	0.09	325.0921	-23.1799	-0.737	0.025	-7.299	0.024	-185.19	0.17	143000	4.99
NGC7492	24.39	0.57	347.1112	-15.6115	0.756	0.028	-2.320	0.028	-176.70	0.27	26600	9.89
Pal1	11.18	0.32	53.3335	79.5811	-0.252	0.034	0.007	0.037	-75.72	0.29	1030	3.56
Pal10	8.94	1.18	289.5069	18.5790	-4.322	0.029	-7.173	0.029	-31.70	0.23	162000	6.33
Pal11	14.02	0.51	296.3100	-8.0072	-1.766	0.030	-4.971	0.028	-67.64	0.76	11900	7.72
Pal12	18.49	0.30	326.6618	-21.2526	-3.220	0.029	-3.333	0.028	27.91	0.28	6270	10.52
Pal13	23.48	0.40	346.6852	12.7715	1.748	0.049	0.104	0.047	25.30	0.22	3020	16.95
Pal14	73.58	1.63	242.7525	14.9578	-0.463	0.038	-0.413	0.038	72.30	0.14	18900	36.70
Pal15	44.10	1.14	254.9626	-0.5390	-0.592	0.037	-0.901	0.034	72.27	1.74	50900	26.86
Pal2	26.17	1.28	71.5246	31.3815	1.045	0.034	-1.522	0.031	-135.97	1.55	231000	8.06
Pal3	94.84	3.23	151.3816	0.0717	0.086	0.060	-0.148	0.071	94.04	0.80	18900	27.44
Pal4	101.39	2.57	172.3183	28.9734	-0.188	0.042	-0.476	0.041	72.40	0.24	12900	21.30
Pal5	21.94	0.51	229.0192	-0.1210	-2.730	0.028	-2.654	0.027	-58.61	0.15	9980	27.64
Pal6	7.05	0.45	265.9258	-26.2250	-9.222	0.038	-5.347	0.036	177.00	1.35	94500	2.89
Pal8	11.32	0.63	280.3773	-19.8289	-1.987	0.027	-5.694	0.027	-31.54	0.21	67400	5.86
Pyxis	36.53	0.66	136.9869	-37.2266	1.030	0.032	0.138	0.035	40.46	0.21	24600	22.83
Rup106	20.71	0.36	189.6675	-51.1503	-1.254	0.026	0.401	0.026	-38.36	0.26	34200	11.57
SagittariusII	66.53	1.56	298.1647	-22.0653	-0.804	0.044	-0.882	0.028	-175.73	0.37	18500	39.31
Ter1	5.67	0.17	263.9467	-30.4818	-2.806	0.055	-4.861	0.055	56.75	1.61	150000	2.15
Ter10	10.21	0.40	270.7408	-26.0669	-6.827	0.059	-2.588	0.050	211.37	2.27	302000	4.60

Table A.1: continued.

Cluster	D kpc	err D kpc	α degrees	δ degrees	μ_α mas/yr	err μ_α mas/yr	μ_δ mas/yr	err μ_δ mas/yr	$v_{\ell os}$ km/s	err $v_{\ell os}$ km/s	M $M_\odot$	r_h pc
Ter12	5.17	0.38	273.0658	-22.7419	-6.222	0.037	-3.052	0.034	95.61	1.21	87200	3.28
Ter2	7.75	0.33	261.8879	-30.8023	-2.170	0.041	-6.263	0.038	134.56	0.96	136000	4.16
Ter3	7.64	0.31	247.1625	-35.3398	-5.577	0.027	-1.760	0.026	-135.76	0.57	40400	7.19
Ter4	7.59	0.31	262.6625	-31.5955	-5.462	0.060	-3.711	0.048	-48.96	1.57	200000	6.06
Ter5	6.62	0.15	267.0202	-24.7791	-1.989	0.068	-5.243	0.066	-82.57	0.73	935000	3.77
Ter6	7.27	0.35	267.6932	-31.2754	-4.979	0.048	-7.431	0.039	136.45	1.50	104000	1.33
Ter7	24.28	0.49	289.4330	-34.6577	-3.002	0.029	-1.651	0.029	159.85	0.14	24000	13.21
Ter8	27.54	0.42	295.4350	-33.9995	-2.496	0.027	-1.581	0.026	148.43	0.17	62100	21.53
Ter9	5.77	0.34	270.4117	-26.8397	-2.121	0.052	-7.763	0.049	68.49	0.56	120000	1.90
Ton2	6.99	0.34	264.0393	-38.5409	-5.904	0.031	-0.755	0.029	-184.72	1.12	69100	4.60
UKS1	15.58	0.56	268.6133	-24.1453	-2.040	0.095	-2.754	0.063	59.38	2.63	77000	3.84
VVV-CL001	8.08	1.48	268.6771	-24.0147	-3.487	0.144	-1.652	0.107	-327.28	0.90	135000	2.94
Whiting1	30.59	1.17	30.7375	-3.2528	-0.228	0.065	-2.046	0.056	-130.41	1.79	1970	15.49

Appendix B: Choice of the time-step for orbit integration

To choose the optimal time-step Δt for the simulations, we quantified the energy conservation of the orbit integration, in the case where the 159 clusters evolve in isolation, that is in the case where each test-particle in a cluster feels the gravitational attraction of the cluster itself, but not that of the Galaxy. Since in the case of an isolated cluster, the gravitational potential is time-independent, the total energy E_i of each particle in the system (sum of the particle kinetic and potential energy) must be conserved. Any departure from energy conservation is thus a check of the quality of the integration and in particular of the choice of the adopted time-step.

For the isolated simulations, we thus proceeded as follows. We modeled each cluster as a set of $N=100\,000$ test-particles, subject to the cluster potential, only. To model this latter, for each cluster we adopted the same Plummer sphere distribution, with same characteristic radius r_c and total masse M_{GC}, as those adopted for the simulations described in Sect. 2 (see in particular Sect. 2.2). A first set of 159 isolated simulations was run adopting a $\Delta t = 10^5$ yr and a total number of steps $N_{steps} = 50000$ for all clusters, for a total simulated time interval of 5 Gyr. We then quantified the energy conservation by calculating the median error per time-step, m_{err}, of $(\Delta E/E)_i = |(E_{fin,i} - E_{ini,i})/E_{ini,i}|$, where $E_{ini,i}$ and $E_{fin,i}$ are, respectively, the initial (time $t = 0$) and final (time t=5 Gyr) energy of each particle in the system. While for most of the simulated clusters (109 over 159), this choice of the time-step was sufficient to guarantee an excellent energy conservation (with m_{err} typically of the order of $10^{-11}-10^{-12}$), for 50 clusters the corresponding m_{err} values were found to be above 10^{-10}. This was the case for all clusters with crossing times $t_{cross} = \sqrt{r_c^3/GM_{GC}}$ lower than 2×10^5 yr, that is about twice the time-step. For these clusters, we hence reduced the Δt of a factor 10, rerunning the simulations with $\Delta t = 10^4$ yr and $N_{steps} = 500000$. With such a choice, the corresponding energy conservation turned out to be excellent (below 10^{-10} per step). In Table B.1, we summarize the result of this study, reporting the cluster name, crossing time, and median error, m_{err}, in energy conservation obtained for all isolated cluster simulations. Clusters for which a $\Delta t = 10^4$ yr, and a corresponding number N_{steps} have been used, are indicated in the Table with an asterisk. The values of Δt adopted for the isolated simulations, and the associated number of time steps, N_{steps}, are also those used to run the simulations of the same clusters orbiting in the gravitational field of the Milky Way.

Appendix C: Extra-tidal features generated by all the simulated clusters

In this section, we report all the extra-tidal features as predicted by our models. For each cluster, we show (from Figs. C.1 to C.20) the probability density of finding associated extra-tidal features in the sky, by calculating the 2D histogram of the escaped particles. Each particle per cluster is present, that is all 100,000 particles originating each of the 50 Monte-Carlo realizations plus the case with the best values (see Sect. 2.1). Thus, each map is a 500x500 histogram that bins 5.1×10^6 particles. The retrieved cumulative 2D histogram is then normalized to its maximum value and plotted in the following figures, in logarithmic scale.

Appendix D: Globular clusters classification

Fig. D.1 (top panel) shows the distribution of the arctangent of the z_{max}/R_{max} ratio, with z_{max} and R_{max} being respectively the maximum height above or below the Galactic plane and their maximum in-plane distance from the Galactic center, reached in the past 5 Gyr of orbital evolution in the Galactic potential adopted in this paper (see Sect. 2.3). As already noticed for field stars (see Haywood et al. 2018), also the GCs distribution shows a dip at about 10°, which separates clusters with flattened orbits ($\arctan(z_{max}/R_{max}) \leq 10°$) from thicker ones. We thus define a first set of clusters (the *disk GCs*) as that containing all globular clusters with $\arctan(z_{max}/R_{max}) \leq 10°$. This first set contains 21 clusters. Of the remaining 138, we distinguish between a *inner GCs* sample, and a *outer GCs* sample, on the basis of the maximum 3D distance (r_{max}) that the cluster reaches from the Galactic center. Inner GCs are those with $r_{max} \leq 10$ kpc and outer GCs are those with $r_{max} > 8.34$ kpc, which is the value of the distance of the Sun to the Galactic Center used in this experiment. Such a value allows to discriminate between two classes of tidal debris, for inner clusters are necessarily restricted in latitude and longitude whereas outer cluster can fill the sky.

Finally the third and bottom panels of Fig. D.1 show the distribution of these three defined groups in the $R_{max} - z_{max}$ and $E - L_z$ planes. We note that, since disk clusters are uniquely defined on the basis of the ratio between the maximum vertical and in-plane orbital excursion, and not on the circularity of their orbits (as done, for example, by Massari et al. 2019), some of our disk GCs have elongated (i.e. radial) orbits ($L_z \sim 0$) or even retrograde ones ($L_z > 0$). Our definition of disk clusters is purely related to a morphological criterium: disk GCs are those whose orbits are confined close to the Galactic plane, independently on their eccentricity.

Table B.1: Crossing time, t_{cross}, and median error in energy conservation, m_{err}, for all 159 clusters evolved in isolation. All "isolated" simulations have been run with a $\Delta t = 10^5$ yr, and for a total of $N_{steps} = 50000$ steps, except for clusters marked with (*), for which a $\Delta t = 10^4$ yr and a a total of $N_{steps} = 500000$ steps have been used.

| Cluster	t_{cross}	m_{err}	Cluster	t_{cross}	m_{err}	Cluster	t_{cross}	m_{err}
2MASS-GC01	5.6×10^5	2.1×10^{-12}	2MASS-GC02	3.9×10^5	4.4×10^{-12}	AM1	6.5×10^6	5.4×10^{-13}
AM4	2.2×10^7	8.6×10^{-13}	Arp2	4.2×10^6	6.1×10^{-13}	BH140	1.2×10^6	5.3×10^{-13}
BH261	6.9×10^5	1.7×10^{-12}	Crater	1.3×10^7	4.4×10^{-13}	Djor1	4.8×10^5	1.0×10^{-12}
Djor2	3.4×10^5	3.9×10^{-12}	E3	2.9×10^6	3.3×10^{-14}	ESO280-SC06	3.5×10^6	1.1×10^{-13}
ESO452-SC11	7.9×10^5	7.9×10^{-13}	Eridanus	7.2×10^6	1.3×10^{-12}	FSR1716	4.7×10^5	3.4×10^{-13}
FSR1735	1.9×10^5	4.9×10^{-11}	FSR1758	9.1×10^5	7.4×10^{-13}	HP1	2.1×10^5	4.0×10^{-11}
IC1257	9.9×10^5	1.5×10^{-14}	IC1276	4.5×10^5	3.4×10^{-12}	IC4499	1.5×10^6	9.0×10^{-13}
Laevens3	6.5×10^6	4.7×10^{-13}	Liller1 (*)	3.0×10^4	6.0×10^{-13}	Lynga7	4.2×10^5	2.3×10^{-13}
NGC104 (*)	1.7×10^5	2.4×10^{-13}	NGC1261	2.96×10^5	1.4×10^{-11}	NGC1851 (*)	9.0×10^4	3.8×10^{-13}
NGC1904 (*)	1.6×10^5	6.8×10^{-10}	NGC2298	2.6×10^5	1.2×10^{-11}	NGC2419	1.4×10^6	1.2×10^{-12}
NGC2808 (*)	8.4×10^4	1.6×10^{-12}	NGC288	8.1×10^5	6.5×10^{-13}	NGC3201	4.5×10^5	1.6×10^{-12}
NGC362 (*)	1.4×10^5	1.9×10^{-13}	NGC4147	4.2×10^5	5.2×10^{-14}	NGC4372	5.7×10^5	4.8×10^{-13}
NGC4590	6.1×10^5	4.3×10^{-13}	NGC4833	2.3×10^5	1.8×10^{-12}	NGC5024	4.9×10^5	3.0×10^{-12}
NGC5053	2.7×10^6	4.4×10^{-13}	NGC5139 (*)	1.8×10^5	1.1×10^{-12}	NGC5272	2.6×10^5	2.0×10^{-12}
NGC5286 (*)	1.3×10^5	1.5×10^{-13}	NGC5466	2.2×10^6	1.0×10^{-12}	NGC5634	4.3×10^5	4.6×10^{-12}
NGC5694	1.9×10^5	6.9×10^{-11}	NGC5824	1.9×10^5	5.2×10^{-11}	NGC5897	9.4×10^5	2.5×10^{-13}
NGC5904	2.2×10^5	8.3×10^{-12}	NGC5927	2.4×10^5	1.9×10^{-11}	NGC5946 (*)	1.4×10^5	1.1×10^{-12}
NGC5986 (*)	1.5×10^5	7.7×10^{-13}	NGC6093 (*)	7.5×10^4	7.9×10^{-13}	NGC6101	1.3×10^6	3.5×10^{-13}
NGC6121	2.5×10^5	9.1×10^{-12}	NGC6139 (*)	7.0×10^4	3.9×10^{-13}	NGC6144	4.0×10^5	3.9×10^{-12}
NGC6171	2.9×10^5	1.7×10^{-12}	NGC6205 (*)	1.7×10^5	1.7×10^{-13}	NGC6218	2.5×10^5	3.0×10^{-12}
NGC6229 (*)	1.8×10^5	2.5×10^{-14}	NGC6235	3.3×10^5	3.1×10^{-12}	NGC6254	2.4×10^5	9.0×10^{-12}
NGC6256	3.1×10^5	7.1×10^{-12}	NGC6266 (*)	5.0×10^4	1.1×10^{-13}	NGC6273 (*)	1.1×10^5	8.0×10^{-13}
NGC6284	2.1×10^5	1.3×10^{-11}	NGC6287	1.9×10^5	3.1×10^{-11}	NGC6293	1.8×10^5	9.9×10^{-11}
NGC6304	2.5×10^5	5.9×10^{-12}	NGC6316 (*)	1.9×10^5	1.3×10^{-13}	NGC6325 (*)	1.2×10^5	4.4×10^{-13}
NGC6333 (*)	1.5×10^5	2.2×10^{-13}	NGC6341 (*)	1.6×10^5	5.6×10^{-13}	NGC6342 (*)	1.5×10^5	3.4×10^{-13}
NGC6352	3.9×10^5	2.2×10^{-12}	NGC6355	2.2×10^5	4.8×10^{-11}	NGC6356	2.4×10^5	3.0×10^{-11}
NGC6362	5.6×10^5	8.1×10^{-13}	NGC6366	6.9×10^5	4.0×10^{-13}	NGC6380 (*)	1.6×10^5	2.1×10^{-13}
NGC6388 (*)	8.3×10^4	6.0×10^{-13}	NGC6397	2.5×10^5	4.1×10^{-12}	NGC6401 (*)	1.6×10^5	6.5×10^{-13}
NGC6402 (*)	1.5×10^5	9.7×10^{-13}	NGC6426	8.6×10^5	8.6×10^{-13}	NGC6440 (*)	4.6×10^4	1.1×10^{-13}
NGC6441 (*)	5.7×10^4	2.6×10^{-14}	NGC6453	1.9×10^5	5.2×10^{-11}	NGC6496	6.3×10^5	2.7×10^{-13}
NGC6517 (*)	8.0×10^4	3.8×10^{-13}	NGC6522 (*)	1.2×10^5	5.9×10^{-12}	NGC6528	1.9×10^5	5.7×10^{-11}
NGC6535	4.8×10^5	2.9×10^{-12}	NGC6539	2.6×10^5	2.5×10^{-12}	NGC6540	6.8×10^5	2.0×10^{-12}
NGC6541 (*)	1.7×10^5	6.1×10^{-13}	NGC6544 (*)	1.0×10^5	6.4×10^{-13}	NGC6553	1.9×10^5	7.8×10^{-11}
NGC6558 (*)	1.4×10^5	7.0×10^{-13}	NGC6569 (*)	1.6×10^5	1.5×10^{-13}	NGC6584	4.0×10^5	4.7×10^{-13}
NGC6624 (*)	1.8×10^5	4.3×10^{-13}	NGC6626 (*)	6.4×10^4	2.5×10^{-12}	NGC6637	1.8×10^5	5.4×10^{-11}
NGC6638 (*)	9.7×10^4	7.8×10^{-13}	NGC6642 (*)	1.0×10^5	1.3×10^{-12}	NGC6652 (*)	1.3×10^5	3.3×10^{-13}
NGC6656 (*)	1.8×10^5	1.5×10^{-13}	NGC6681 (*)	1.5×10^5	4.3×10^{-13}	NGC6712	1.9×10^5	4.5×10^{-11}
NGC6715 (*)	9.1×10^4	1.4×10^{-12}	NGC6717	4.7×10^5	7.4×10^{-13}	NGC6723	2.8×10^5	2.1×10^{-11}
NGC6749	4.2×10^5	7.0×10^{-13}	NGC6752	2.4×10^5	2.9×10^{-11}	NGC6760	2.4×10^5	6.7×10^{-12}
NGC6779	2.3×10^5	1.3×10^{-11}	NGC6809	4.3×10^5	1.7×10^{-12}	NGC6838	6.7×10^5	7.0×10^{-14}
NGC6864 (*)	8.6×10^4	9.1×10^{-13}	NGC6934	3.2×10^5	6.4×10^{-12}	NGC6981	5.7×10^5	7.0×10^{-13}
NGC7006	5.1×10^5	9.1×10^{-13}	NGC7078 (*)	1.1×10^5	4.1×10^{-13}	NGC7089 (*)	1.4×10^5	1.3×10^{-13}
NGC7099	3.0×10^5	5.2×10^{-14}	NGC7492	1.9×10^5	6.0×10^{-13}	Pal1	2.1×10^6	3.0×10^{-13}
Pal10	4.0×10^5	4.6×10^{-13}	Pal11	2.0×10^6	3.5×10^{-13}	Pal12	4.4×10^6	1.1×10^{-12}
Pal13	1.3×10^7	3.0×10^{-13}	Pal14	1.7×10^7	7.4×10^{-13}	Pal15	6.3×10^6	9.2×10^{-14}
Pal2	4.9×10^5	4.1×10^{-13}	Pal3	1.1×10^7	8.1×10^{-13}	Pal4	8.8×10^6	6.6×10^{-13}
Pal5	1.5×10^7	6.2×10^{-13}	Pal6 (*)	1.6×10^5	1.0×10^{-12}	Pal8	5.6×10^5	1.1×10^{-12}
Pyxis	7.2×10^6	6.0×10^{-13}	Rup106	2.2×10^6	9.4×10^{-13}	SagittariusII	1.9×10^7	7.3×10^{-13}
Ter1 (*)	8.3×10^4	7.1×10^{-13}	Ter10	1.8×10^5	7.3×10^{-11}	Ter12	2.1×10^5	3.1×10^{-11}
Ter2	2.4×10^5	1.2×10^{-11}	Ter3	9.8×10^5	1.2×10^{-12}	Ter4	3.4×10^5	5.9×10^{-12}
Ter5 (*)	7.7×10^4	3.5×10^{-13}	Ter6 (*)	4.9×10^4	1.5×10^{-12}	Ter7	3.2×10^6	7.4×10^{-13}
Ter8	4.1×10^6	9.4×10^{-13}	Ter9 (*)	7.7×10^4	4.7×10^{-13}	Ton2	3.8×10^5	1.1×10^{-13}
UKS1	2.8×10^5	2.0×10^{-12}	VVV-CL001 (*)	1.4×10^5	1.1×10^{-12}	Whiting1	1.4×10^7	1.6×10^{-13}
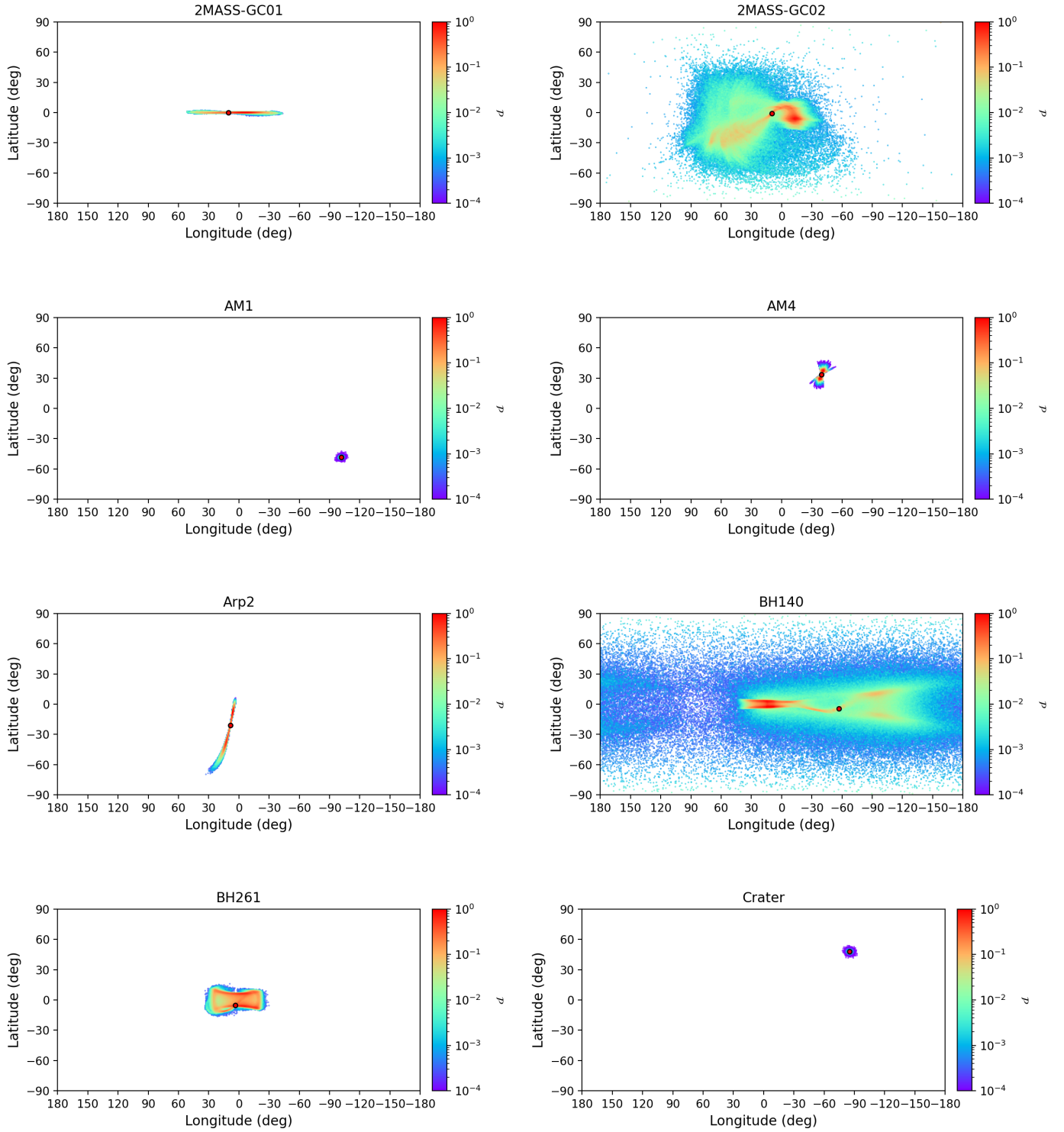
Fig. C.1: Projected density distribution in the (ℓ, b) plane of a subset of simulated globular clusters, as indicated at the top of each panel. In each panel, the red circle indicates the current position of the cluster. The densities have been normalized to their maximum value.
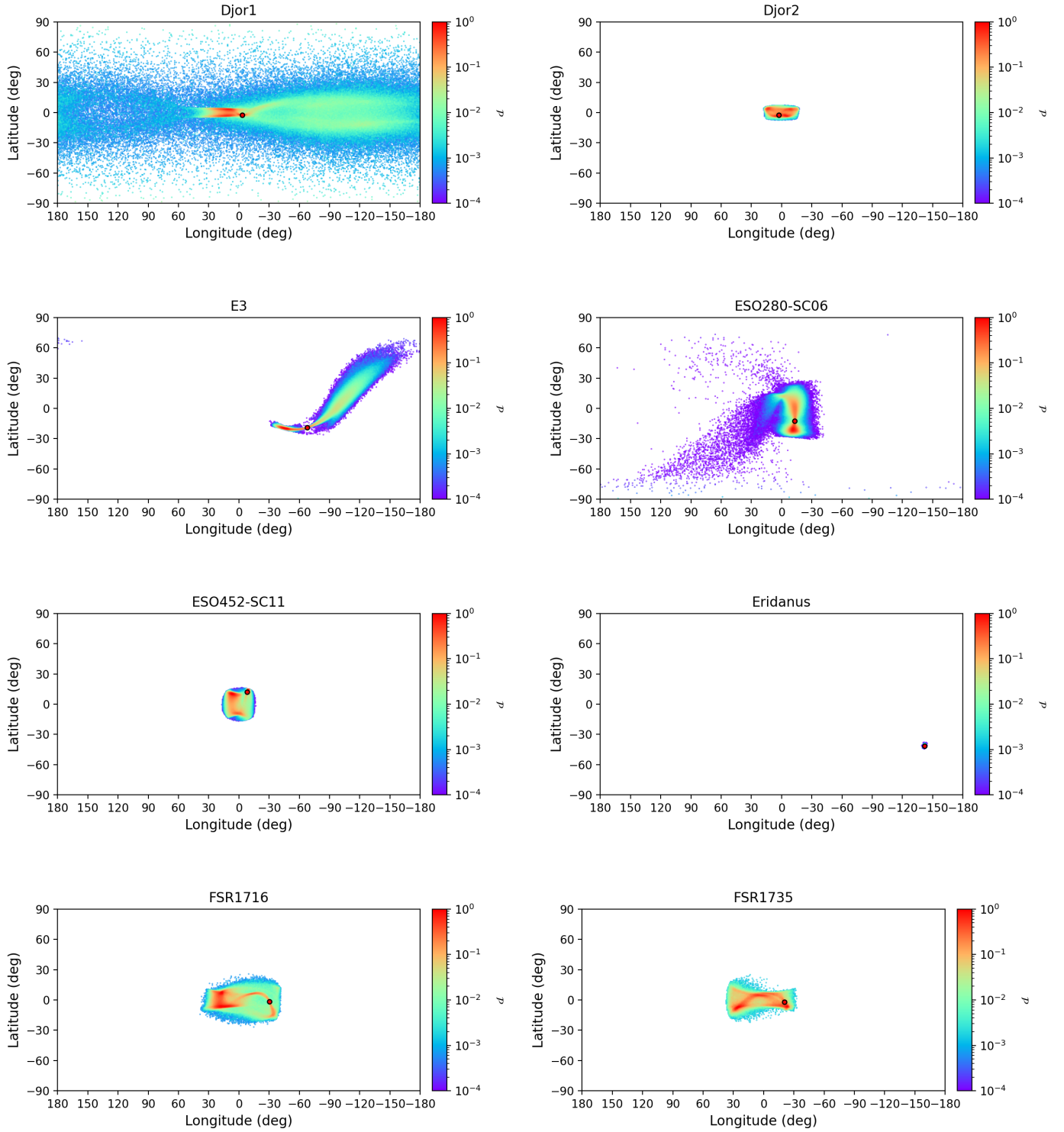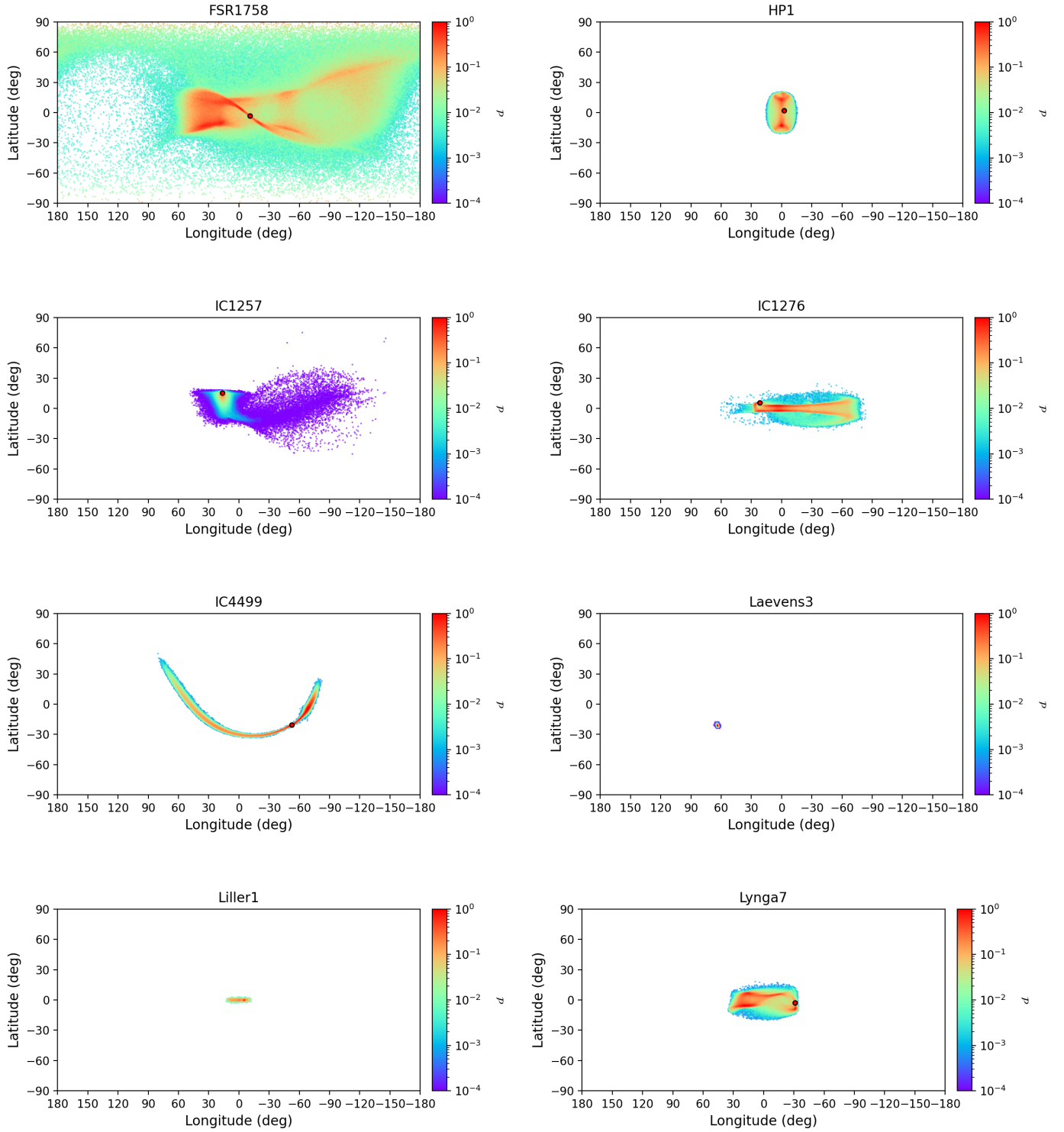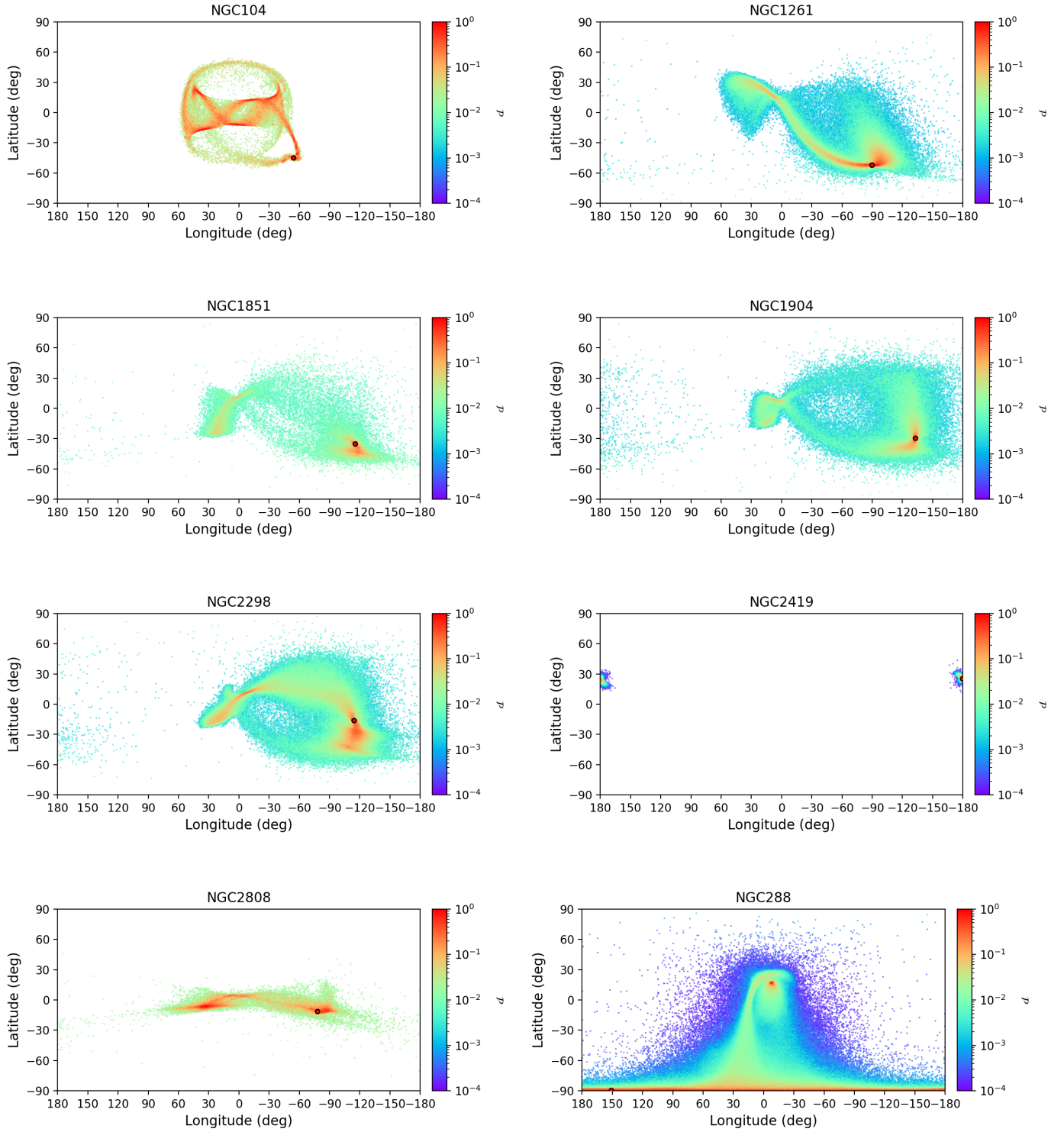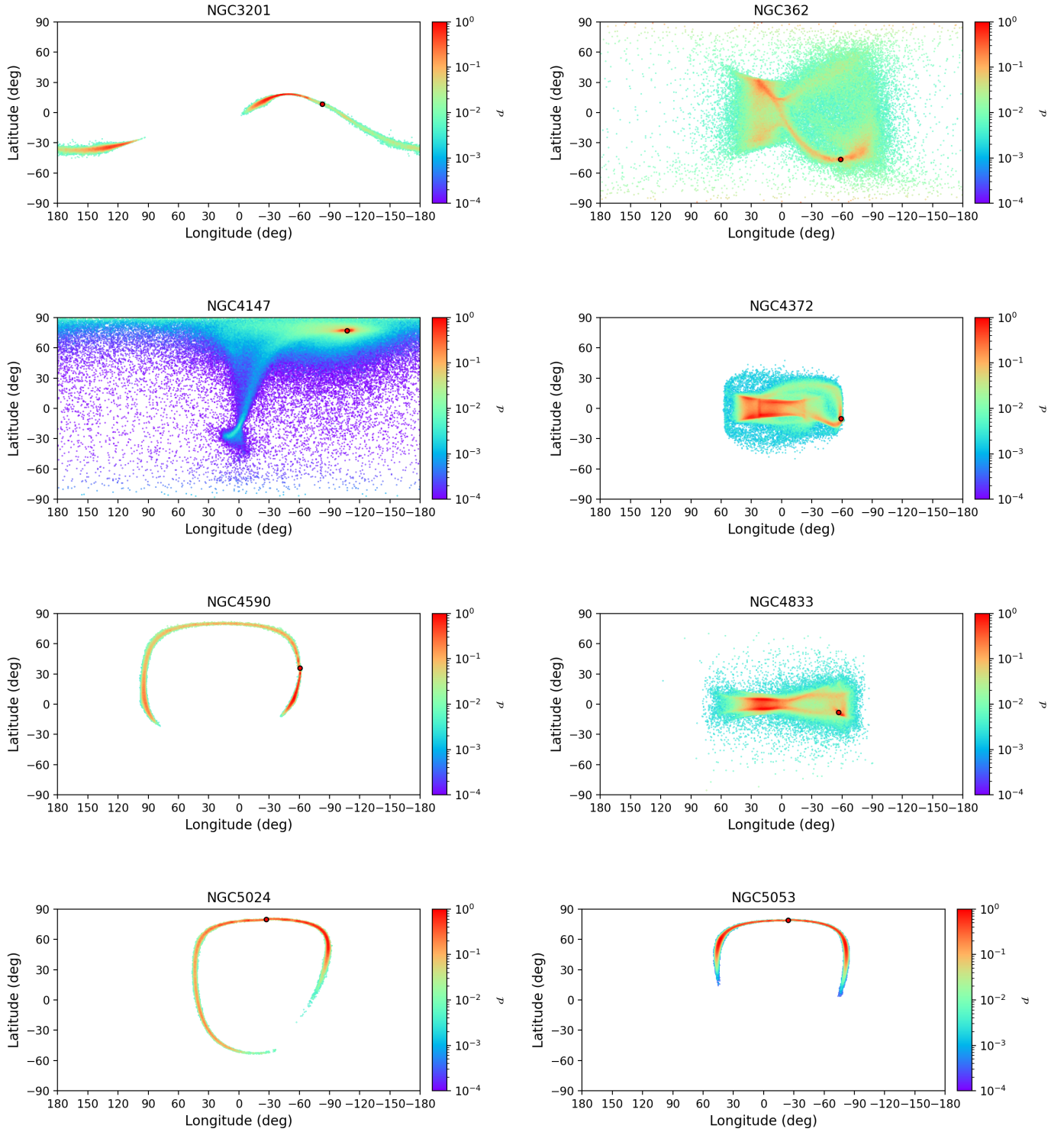
Fig. C.2: Projected density distribution in the (ℓ, b) plane of a subset of simulated globular clusters, as indicated at the top of each panel. In each panel, the red circle indicates the current position of the cluster. The densities have been normalized to their maximum value.
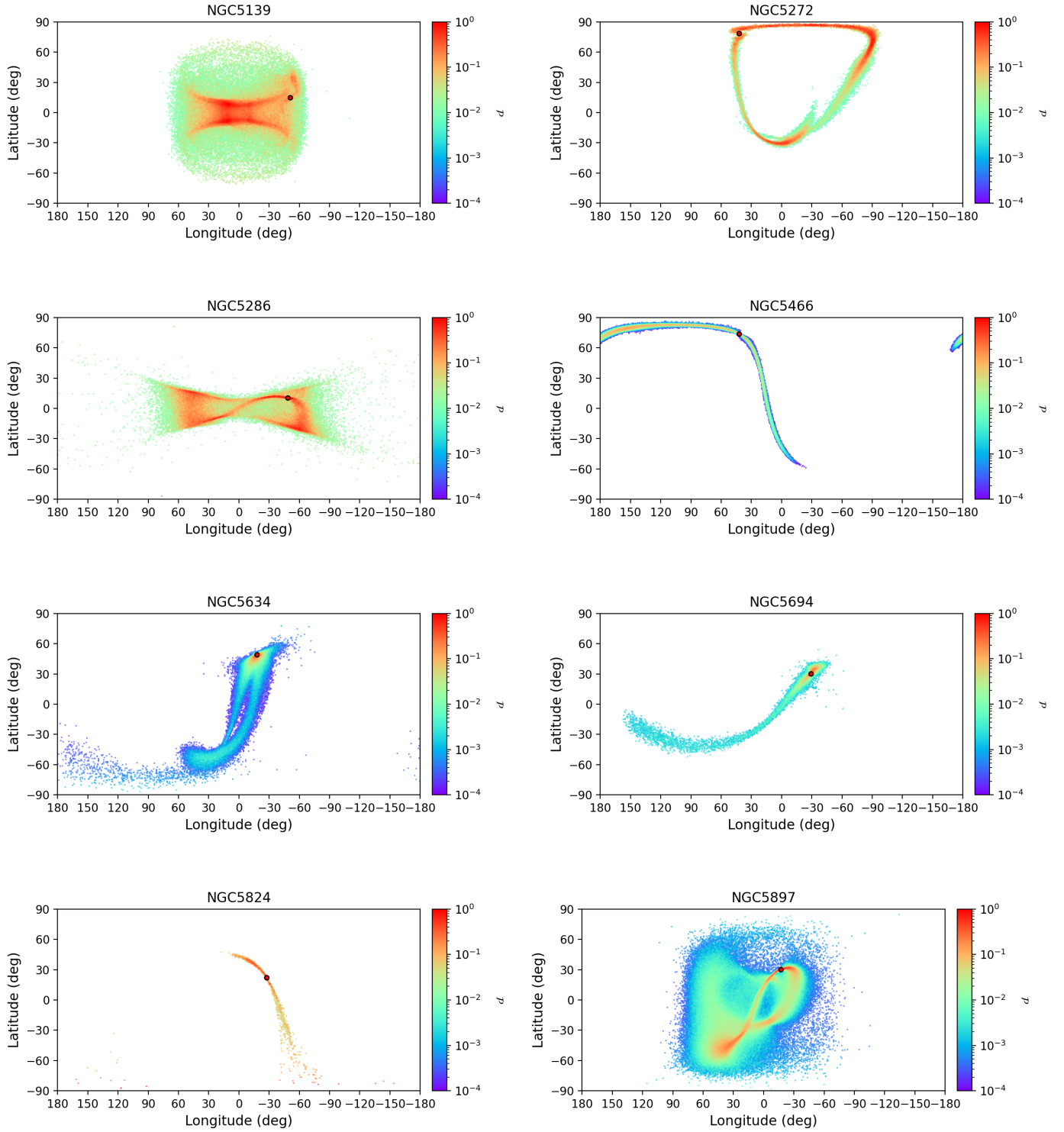
Fig. C.3: Projected density distribution in the (ℓ, b) plane of a subset of simulated globular clusters, as indicated at the top of each panel. In each panel, the red circle indicates the current position of the cluster. The densities have been normalized to their maximum value.
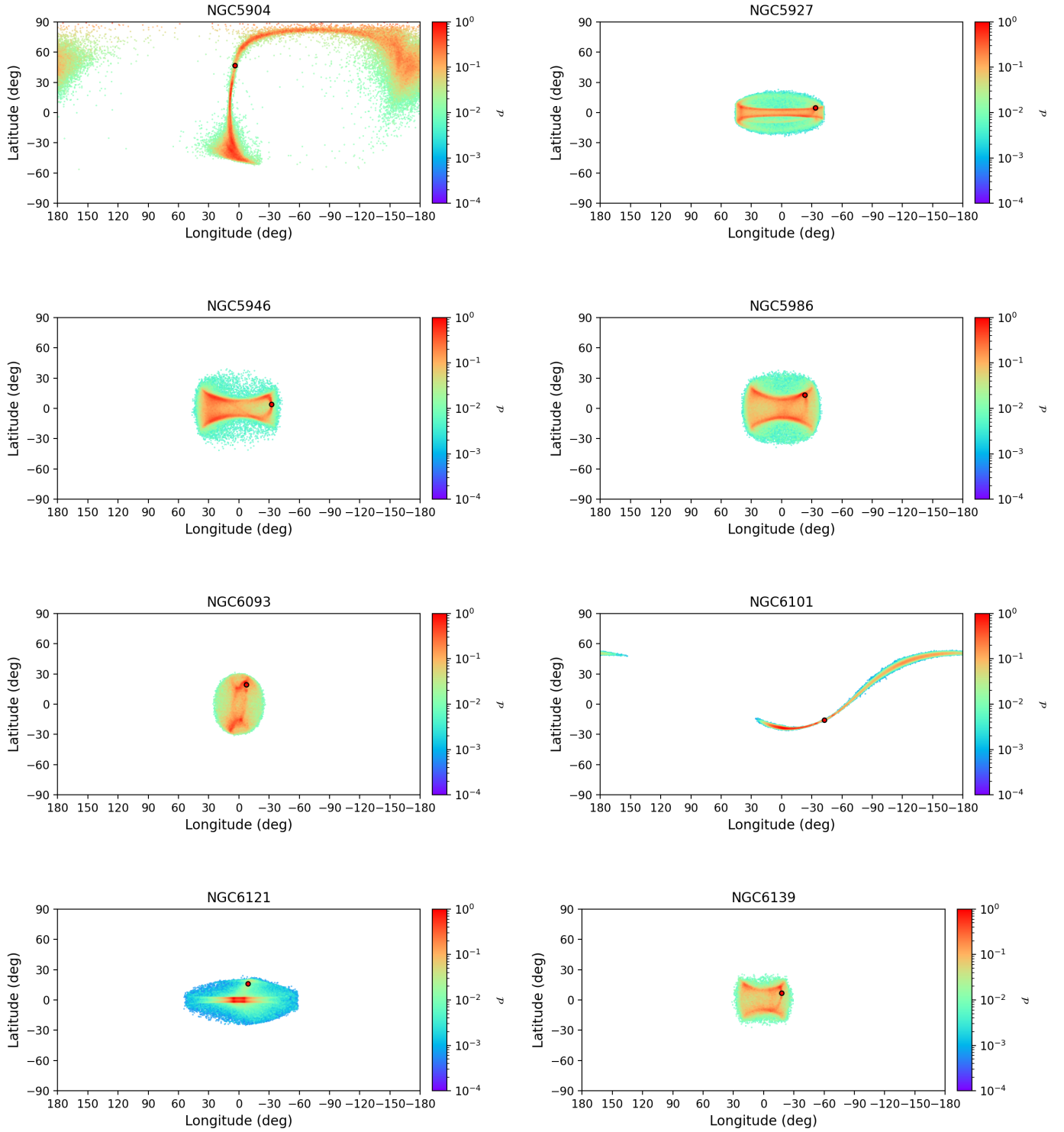
Fig. C.4: Projected density distribution in the (ℓ, b) plane of a subset of simulated globular clusters, as indicated at the top of each panel. In each panel, the red circle indicates the current position of the cluster. The densities have been normalized to their maximum value.

Fig. C.5: Projected density distribution in the (ℓ, b) plane of a subset of simulated globular clusters, as indicated at the top of each panel. In each panel, the red circle indicates the current position of the cluster. The densities have been normalized to their maximum value.
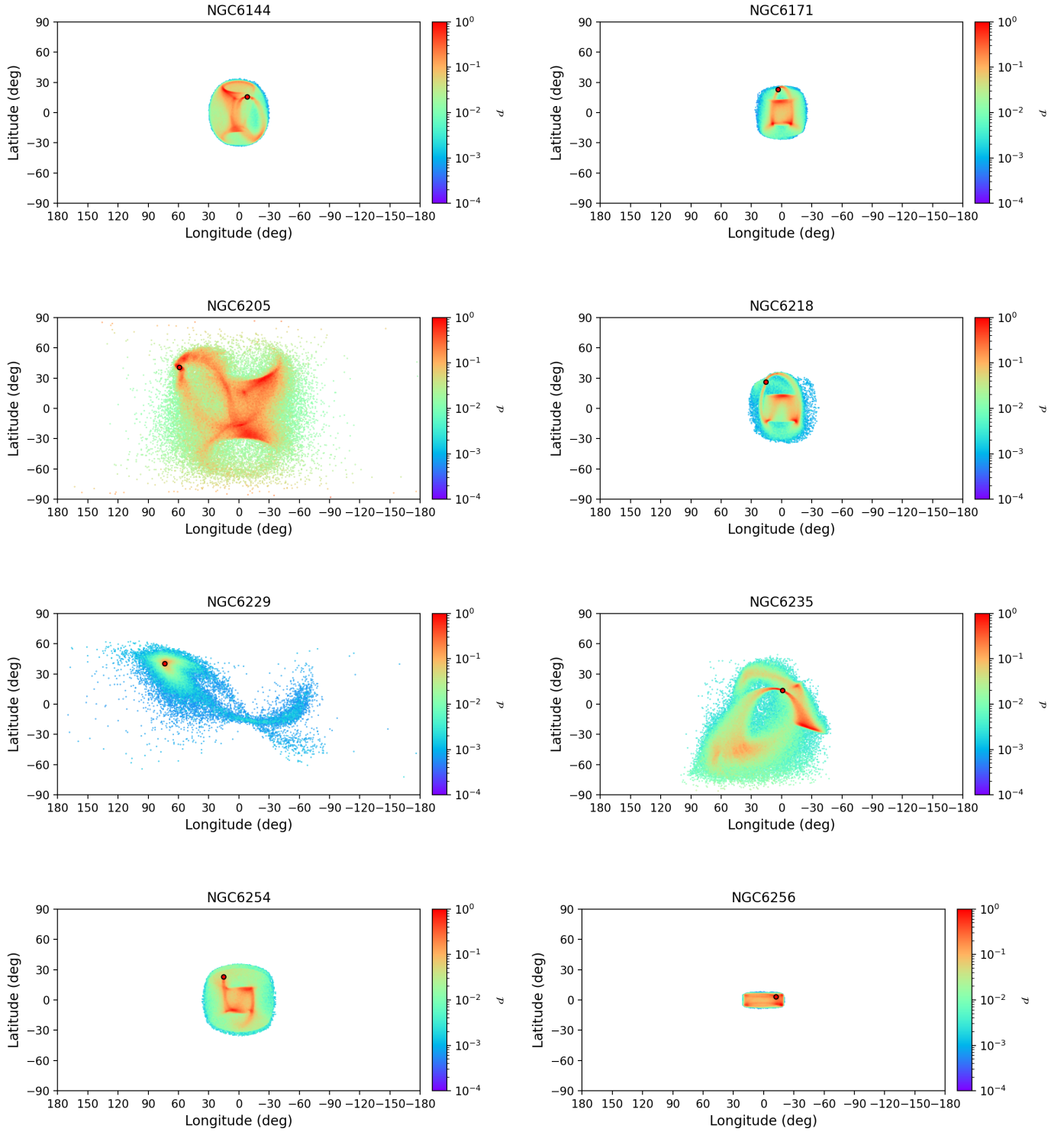
Fig. C.6: Projected density distribution in the (ℓ, b) plane of a subset of simulated globular clusters, as indicated at the top of each panel. In each panel, the red circle indicates the current position of the cluster. The densities have been normalized to their maximum value.
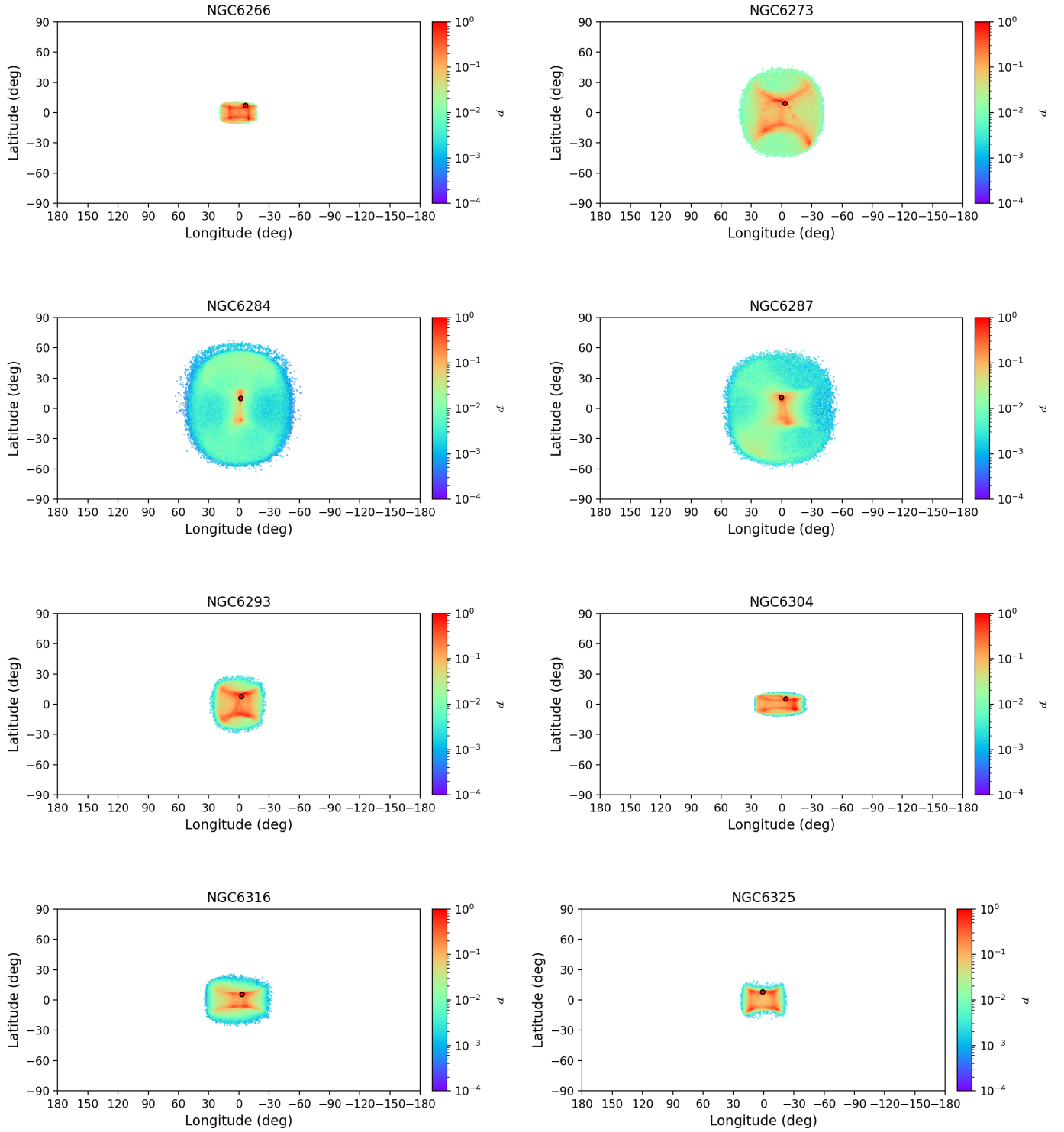
Fig. C.7: Projected density distribution in the (ℓ, b) plane of a subset of simulated globular clusters, as indicated at the top of each panel. In each panel, the red circle indicates the current position of the cluster. The densities have been normalized to their maximum value.

Fig. C.8: Projected density distribution in the (ℓ, b) plane of a subset of simulated globular clusters, as indicated at the top of each panel. In each panel, the red circle indicates the current position of the cluster. The densities have been normalized to their maximum value.
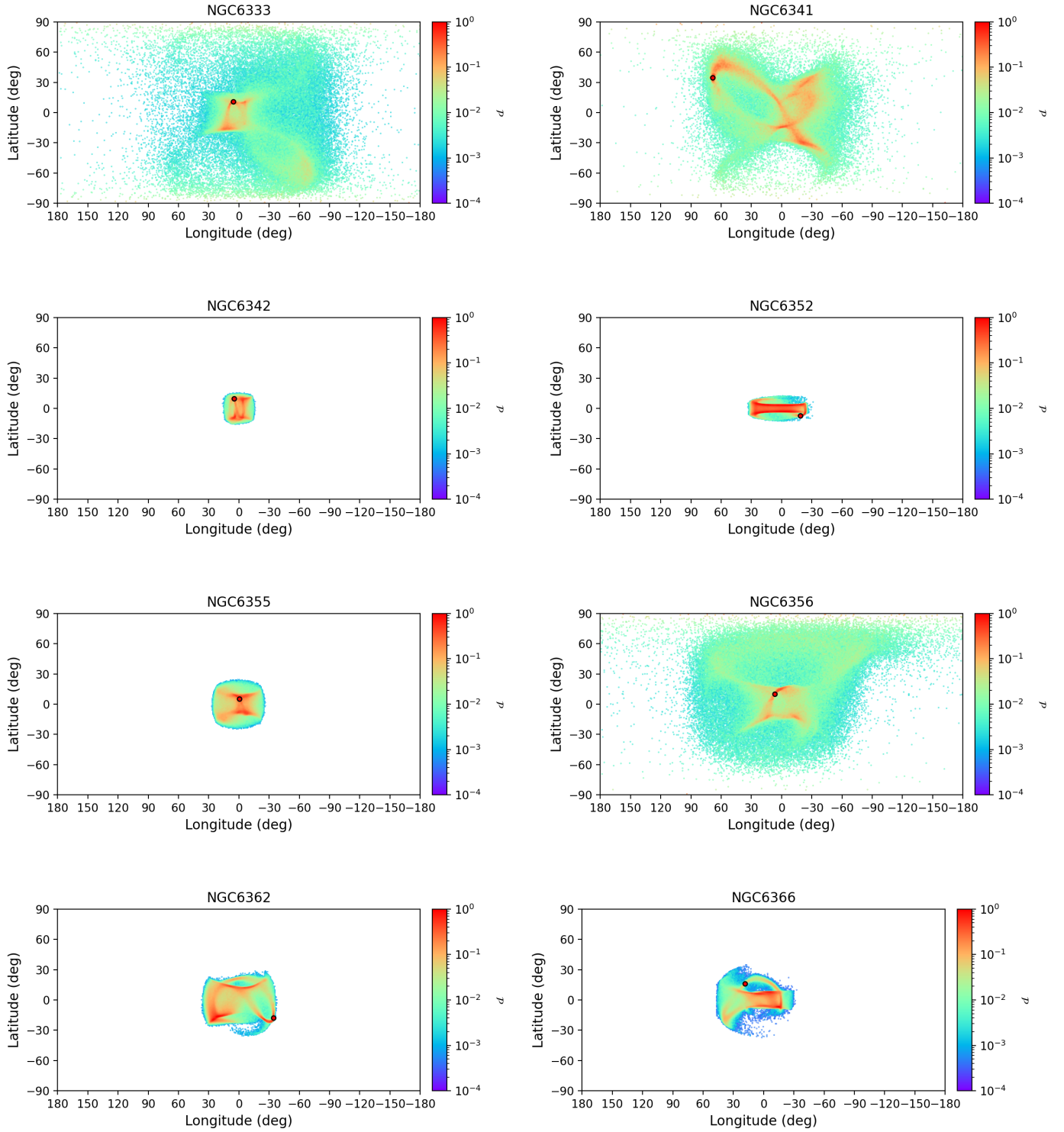
Fig. C.9: Projected density distribution in the (ℓ, b) plane of a subset of simulated globular clusters, as indicated at the top of each panel. In each panel, the red circle indicates the current position of the cluster. The densities have been normalized to their maximum value.

Fig. C.10: Projected density distribution in the (ℓ, b) plane of a subset of simulated globular clusters, as indicated at the top of each panel. In each panel, the red circle indicates the current position of the cluster. The densities have been normalized to their maximum value.
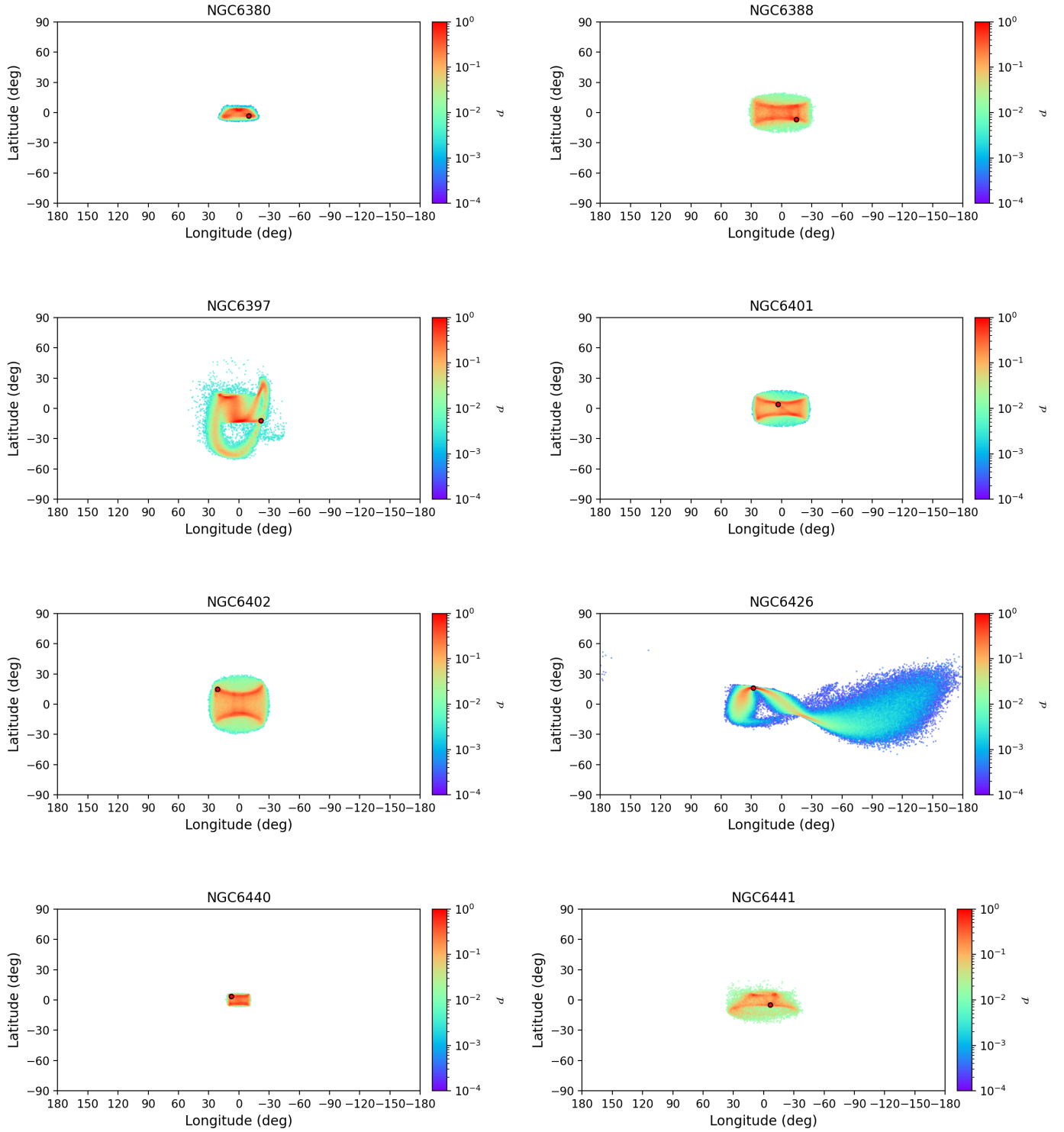
Fig. C.11: Projected density distribution in the (ℓ, b) plane of a subset of simulated globular clusters, as indicated at the top of each panel. In each panel, the red circle indicates the current position of the cluster. The densities have been normalized to their maximum value.
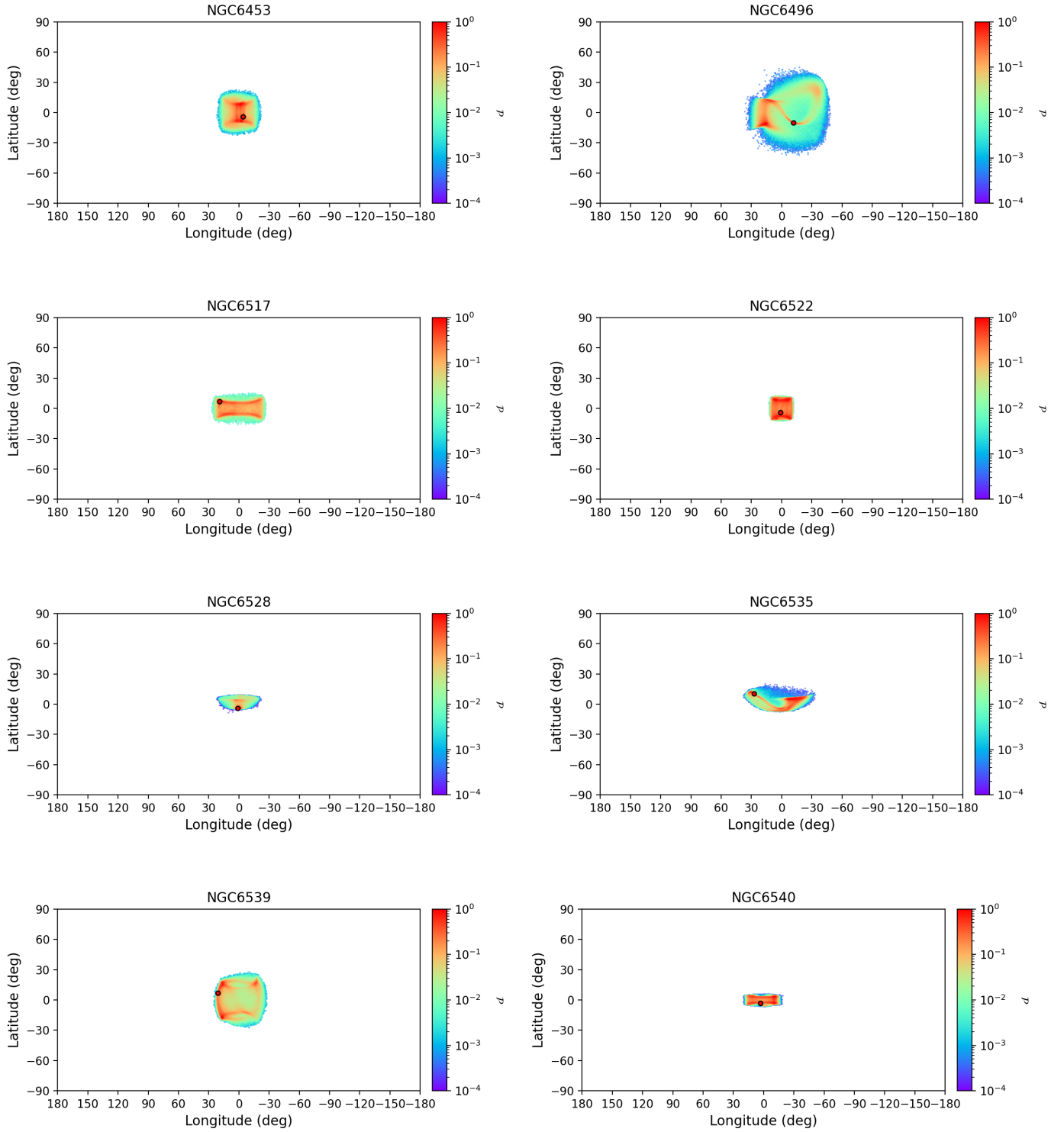
Fig. C.12: Projected density distribution in the (ℓ, b) plane of a subset of simulated globular clusters, as indicated at the top of each panel. In each panel, the red circle indicates the current position of the cluster. The densities have been normalized to their maximum value.
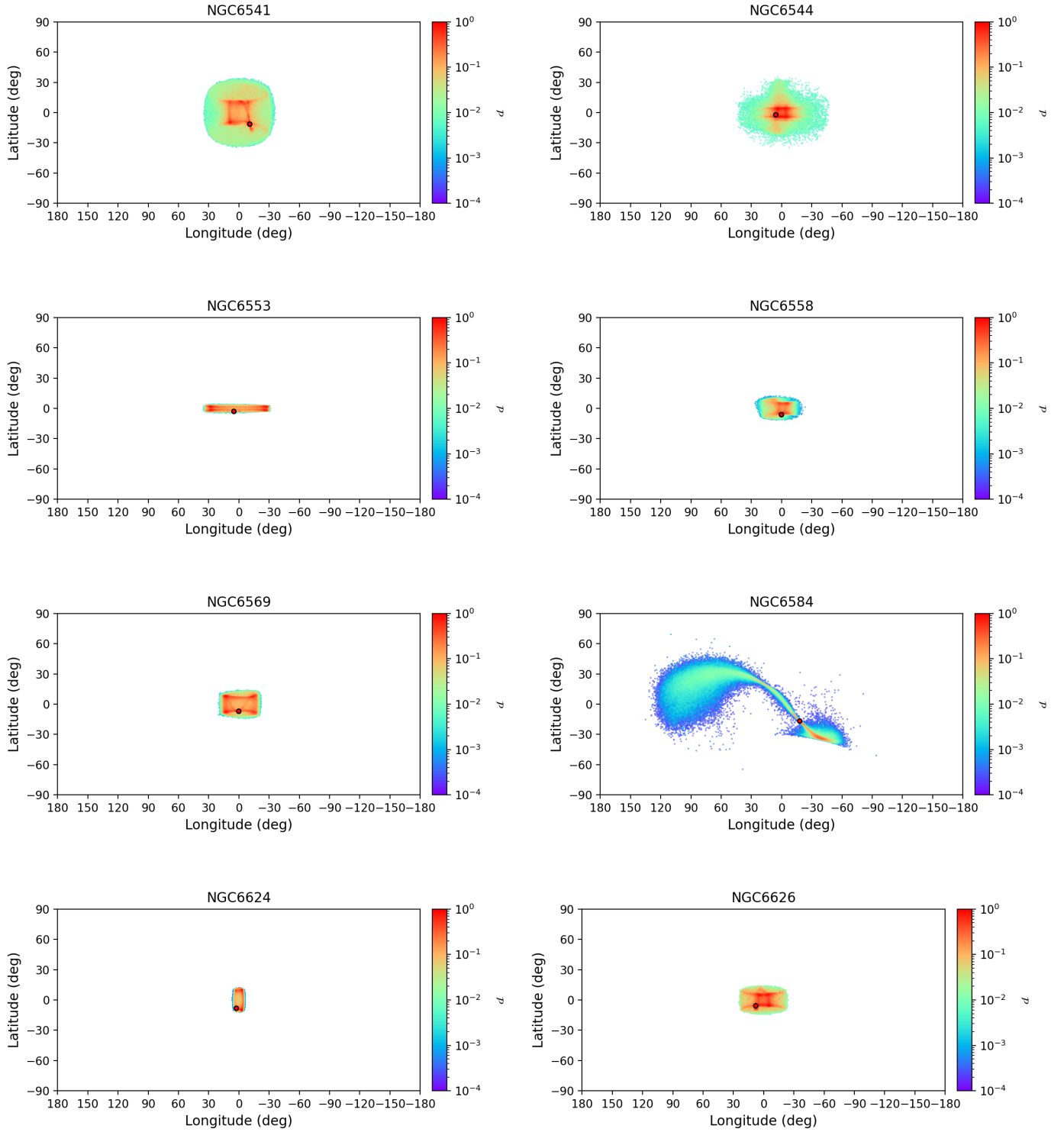
Fig. C.13: Projected density distribution in the (ℓ, b) plane of a subset of simulated globular clusters, as indicated at the top of each panel. In each panel, the red circle indicates the current position of the cluster. The densities have been normalized to their maximum value.

Fig. C.14: Projected density distribution in the (ℓ, b) plane of a subset of simulated globular clusters, as indicated at the top of each panel. In each panel, the red circle indicates the current position of the cluster. The densities have been normalized to their maximum value.
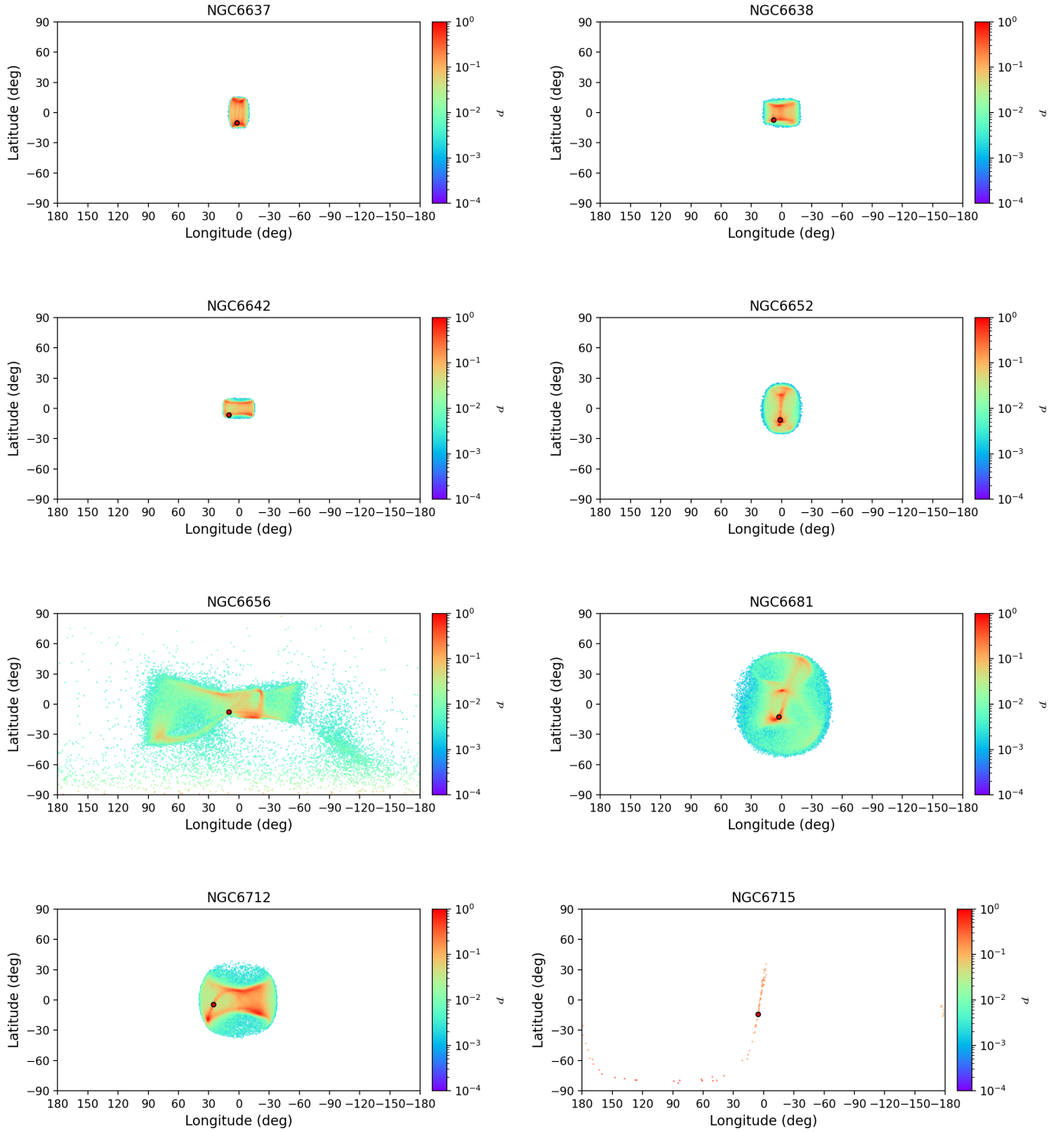
Fig. C.15: Projected density distribution in the (ℓ, b) plane of a subset of simulated globular clusters, as indicated at the top of each panel. In each panel, the red circle indicates the current position of the cluster. The densities have been normalized to their maximum value.

Fig. C.16: Projected density distribution in the (ℓ, b) plane of a subset of simulated globular clusters, as indicated at the top of each panel. In each panel, the red circle indicates the current position of the cluster. The densities have been normalized to their maximum value.
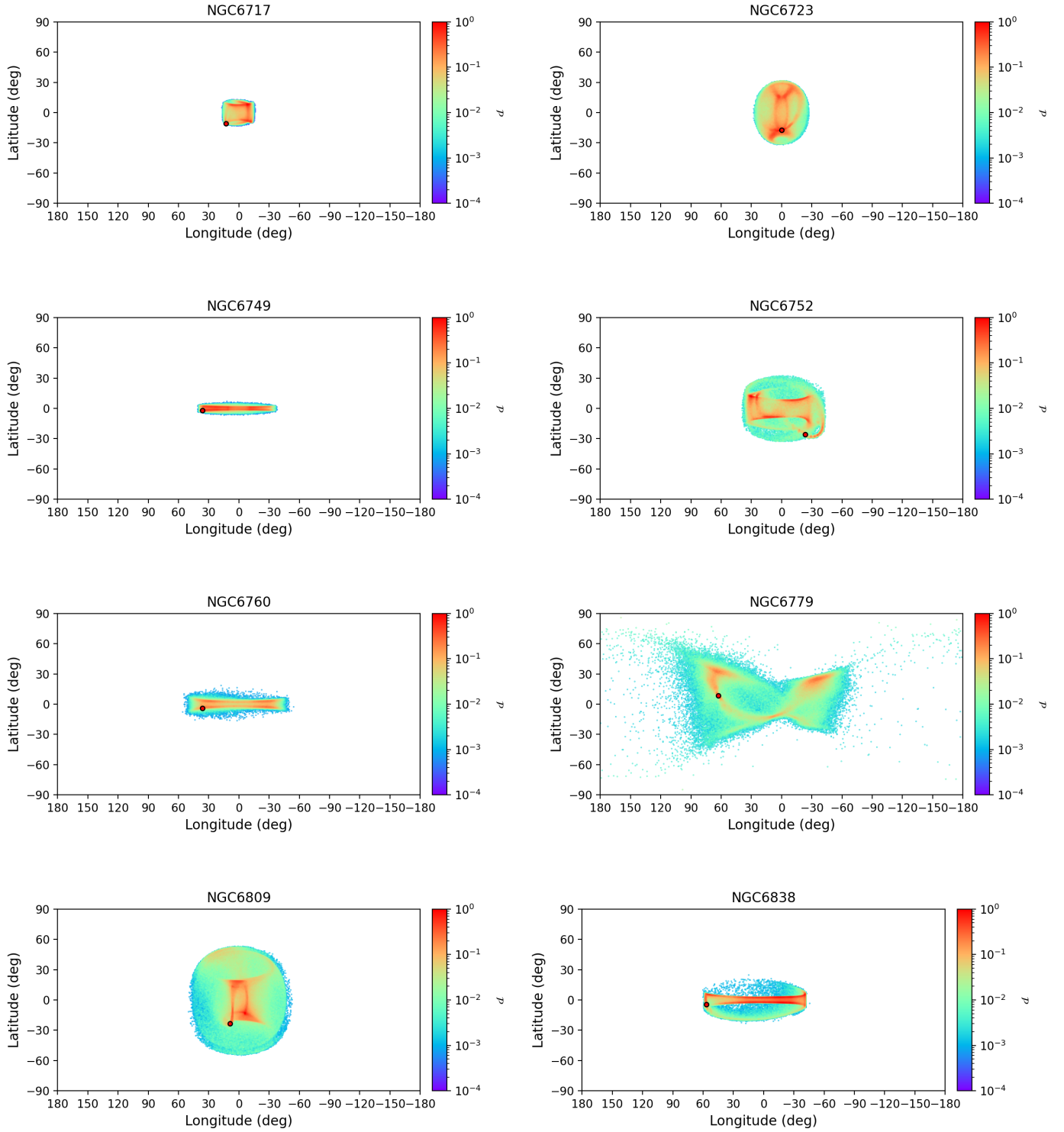
Fig. C.17: Projected density distribution in the (ℓ, b) plane of a subset of simulated globular clusters, as indicated at the top of each panel. In each panel, the red circle indicates the current position of the cluster. The densities have been normalized to their maximum value.
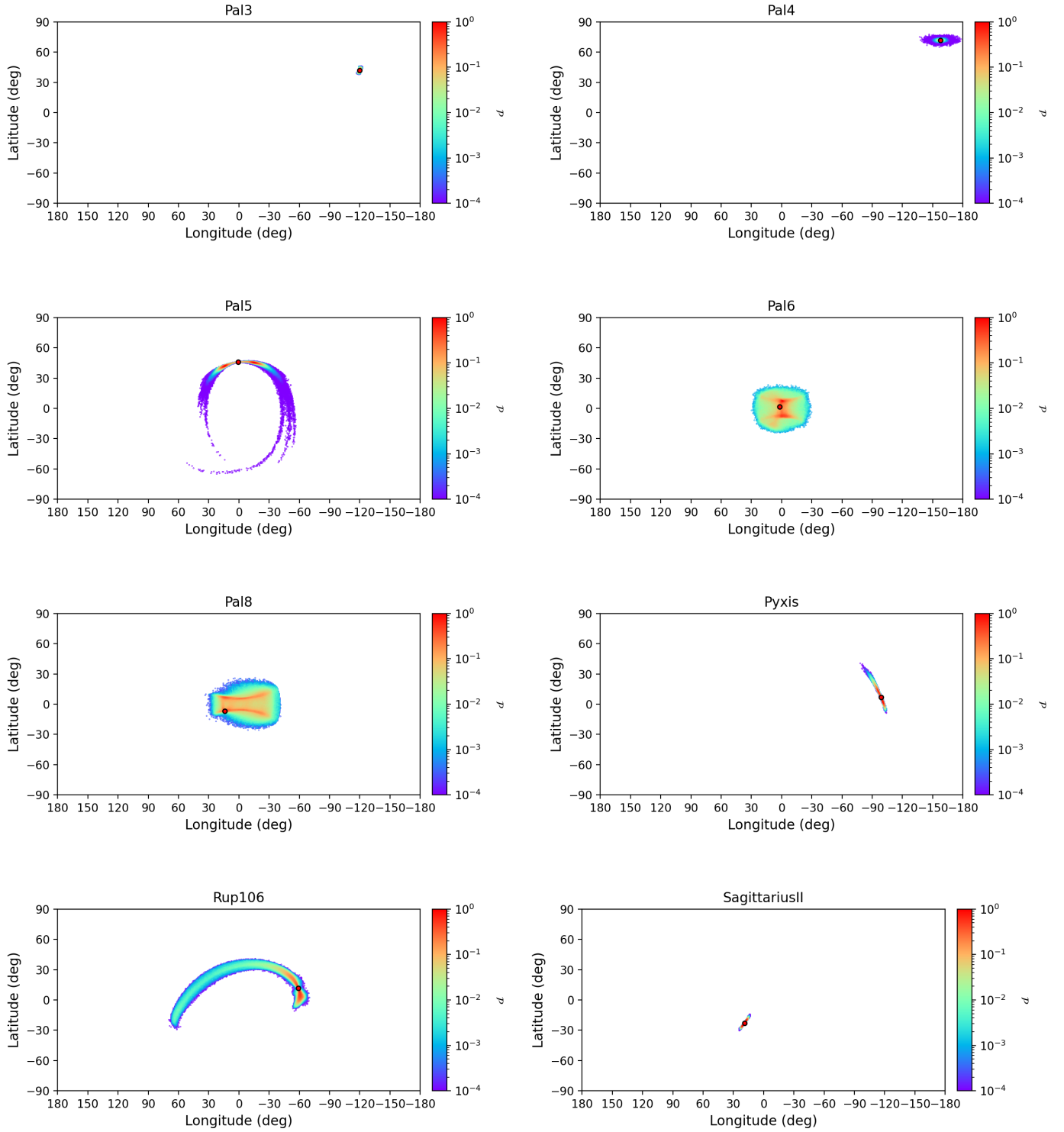
Fig. C.18: Projected density distribution in the (ℓ, b) plane of a subset of simulated globular clusters, as indicated at the top of each panel. In each panel, the red circle indicates the current position of the cluster. The densities have been normalized to their maximum value.
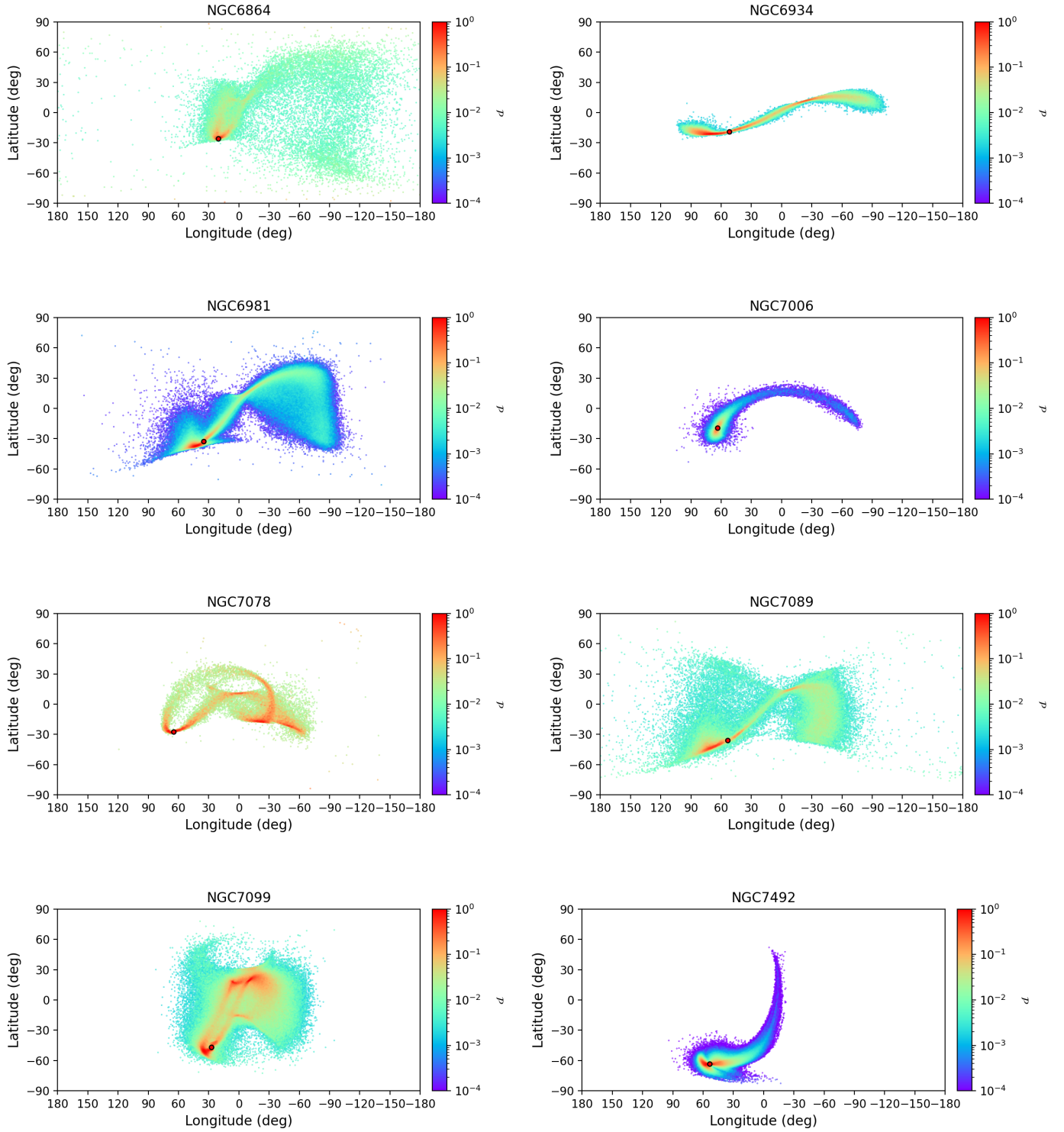
Fig. C.19: Projected density distribution in the (ℓ, b) plane of a subset of simulated globular clusters, as indicated at the top of each panel. In each panel, the red circle indicates the current position of the cluster. The densities have been normalized to their maximum value.
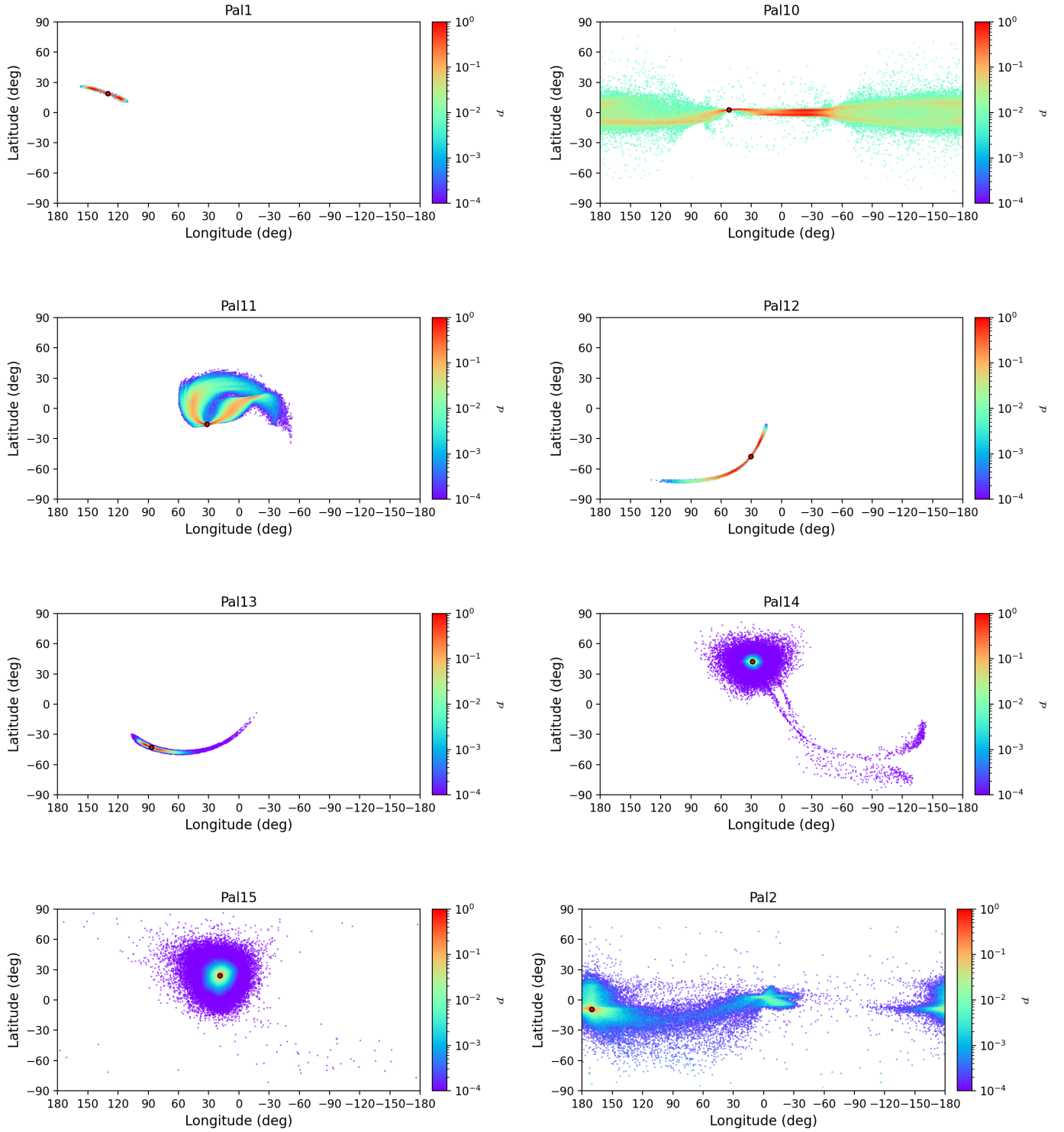
Fig. C.20: Projected density distribution in the (ℓ, b) plane of a subset of simulated globular clusters, as indicated at the top of each panel. In each panel, the red circle indicates the current position of the cluster. The densities have been normalized to their maximum value.
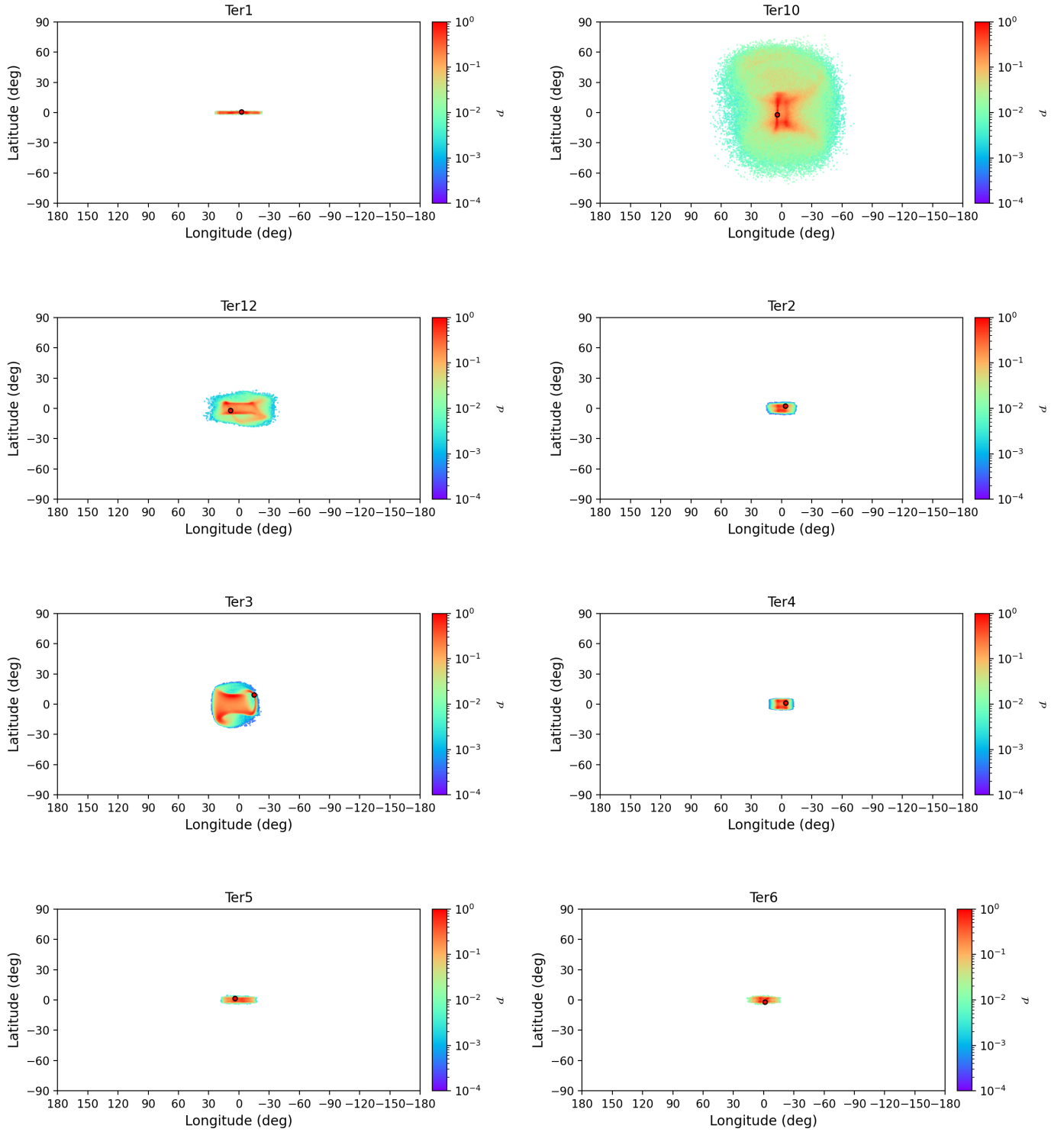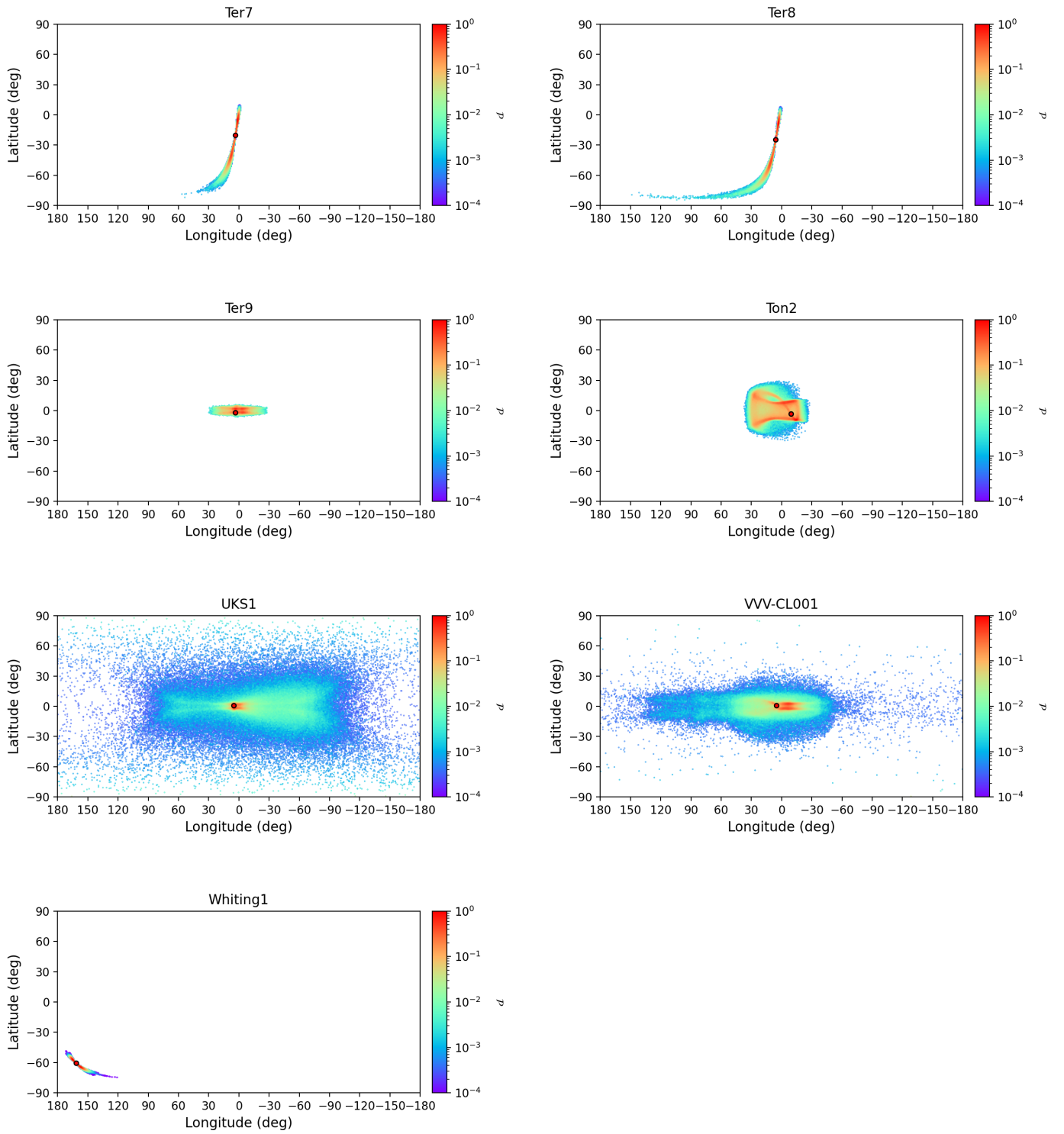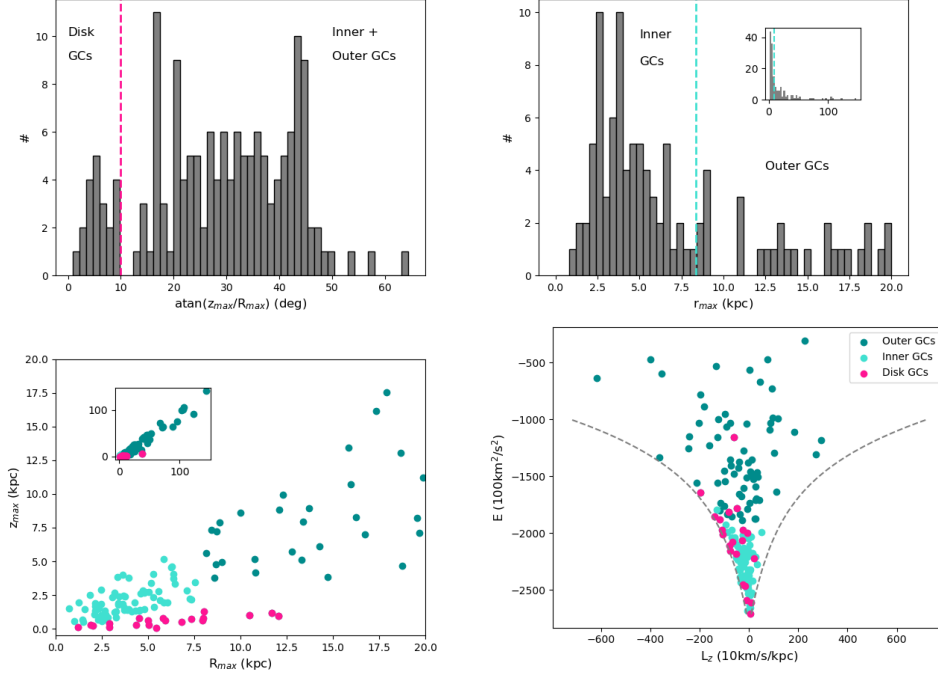
Fig. D.1: *From the top left to the bottom right:* (*First panel*) Distribution of the arctangent of the z_{max}/R_{max} ratio for all simulated GCs. The values are expressed in degrees. The vertical dashed line at 10° separates disk clusters (arctan(z_{max}/R_{max}) ≤ 10°) from the rest of the population of GCs; (*Second panel*) Distribution of the maximum 3D distance, r_{max}, from the Galactic center, reached by the GCs orbits in the last 5 Gyr. The main plot shows this distribution for r_{max} ≤ 20 kpc, where as the inset shows the whole distribution, which extends at r_{max} > 100 kpc. In both panels the vertical dashed line, at the solar radius $r_\odot$, separates the group of inner GCs from the group of outer GCs. Note that the clusters in one of these two groups which also satisfy the criterion to be disk clusters are classified as disk GCs, and are not in the inner/outer GCs groups. (*Third panel*) Distribution of disk GCs (magenta points), inner GCs (turquoise points), and outer GCs (dark turquoise points) in the $R_{max} - z_{max}$ plane. The main panel shows the distribution of the GCs having R_{max} ≤ 20 kpc, the inset the distribution of the whole GC sample. (*Fourth panel*) Distribution of the disk GCs (magenta points), inner GCs (turquoise points), and outer GCs (dark turquoise points) in the $E - L_z$ plane. The dashed grey lines correspond, for any given energy E, to the angular momentum of the corresponding circular orbit. Prograde orbits correspond to negative L_z values, retrograde orbits to positive L_z.

Table D.1: Classification of the 159 globular clusters studied in this paper in disk clusters ("D"), inner clusters ("I") and outer clusters ("O"). The values of r_{max} and the angle in degrees of the $arctan(z_{max}/R_{max})$ are also given.

Cluster	r_{max}	angle	class	Cluster	r_{max}	angle	class	Cluster	r_{max}	angle	class
2MASS-GC01	5.45	0.85	D	2MASS-GC02	7.38	17.15	I	AM1	123.19	36.56	O
AM4	26.97	43.53	O	Arp2	42.44	44.54	O	BH140	10.52	5.54	D
BH261	3.83	21.02	I	Crater	147.37	44.46	O	Djor1	11.74	5.77	D
Djor2	2.39	16.74	I	E3	12.91	24.07	O	ESO280-SC06	13.82	33.04	O
ESO452-SC11	2.53	41.47	I	Eridanus	109.07	44.83	O	FSR1716	5.46	17.07	I
FSR1735	4.43	17.10	I	FSR1758	14.35	23.13	O	HP1	2.70	53.56	I
IC1257	19.69	19.93	O	IC1276	7.98	5.71	D	IC4499	27.17	42.77	O
Laevens3	70.74	41.35	O	Liller1	1.20	5.84	D	Lynga7	4.69	17.18	I
NGC104	7.71	24.70	I	NGC1261	20.99	36.68	O	NGC1851	19.94	29.46	O
NGC1904	19.57	22.81	O	NGC2298	16.69	26.93	O	NGC2419	96.76	38.13	O
NGC2808	14.92	14.57	O	NGC288	12.50	39.00	O	NGC3201	25.53	22.62	O
NGC362	12.27	36.03	O	NGC4147	24.90	45.18	O	NGC4372	7.36	16.30	I
NGC4590	27.99	32.55	O	NGC4833	8.13	9.07	D	NGC5024	22.32	44.24	O
NGC5053	18.08	44.39	O	NGC5139	7.14	21.89	I	NGC5272	16.02	40.27	O
NGC5286	13.32	21.11	O	NGC5466	41.16	43.51	O	NGC5634	22.18	43.13	O
NGC5694	51.29	35.50	O	NGC5824	32.44	40.00	O	NGC5897	9.18	41.61	O
NGC5904	24.76	42.83	O	NGC5927	5.83	7.91	D	NGC5946	5.31	23.80	I
NGC5986	5.00	29.36	I	NGC6093	4.04	49.12	I	NGC6101	32.24	30.56	O
NGC6121	6.84	4.48	D	NGC6139	3.72	34.95	I	NGC6144	4.41	43.66	I
NGC6171	3.95	33.40	I	NGC6205	8.96	39.68	O	NGC6218	4.95	31.01	I
NGC6229	30.26	37.44	O	NGC6235	8.37	34.55	O	NGC6254	4.98	29.32	I
NGC6256	2.68	14.83	I	NGC6266	2.57	21.99	I	NGC6273	5.56	37.78	I
NGC6284	6.51	36.21	I	NGC6287	6.50	30.33	I	NGC6293	3.40	37.21	I
NGC6304	3.38	14.75	I	NGC6316	3.80	22.98	I	NGC6325	2.57	32.34	I
NGC6333	9.07	28.89	O	NGC6341	10.90	40.72	O	NGC6342	2.48	38.09	I
NGC6352	4.53	9.72	D	NGC6355	3.55	29.38	I	NGC6356	8.83	28.77	O
NGC6362	5.41	33.16	I	NGC6366	6.04	17.80	I	NGC6380	2.35	16.74	I
NGC6388	3.91	19.73	I	NGC6397	6.61	27.48	I	NGC6401	3.70	21.02	I
NGC6402	3.99	32.64	I	NGC6426	16.84	22.68	O	NGC6440	1.53	25.31	I
NGC6441	4.67	16.48	I	NGC6453	2.71	36.68	I	NGC6496	5.71	26.65	I
NGC6517	3.31	21.34	I	NGC6522	1.97	42.54	I	NGC6528	2.89	16.38	I
NGC6535	4.92	16.72	I	NGC6539	3.64	39.67	I	NGC6540	2.54	12.61	I
NGC6541	4.78	29.39	I	NGC6544	5.93	18.30	I	NGC6553	4.36	4.14	D
NGC6558	2.75	21.35	I	NGC6569	2.85	26.50	I	NGC6584	20.31	35.07	O
NGC6624	1.61	64.40	I	NGC6626	3.22	20.88	I	NGC6637	2.11	56.81	I
NGC6638	2.34	31.98	I	NGC6642	2.20	26.61	I	NGC6652	3.15	49.58	I
NGC6656	10.87	21.01	O	NGC6681	6.33	41.70	I	NGC6712	5.15	28.49	I
NGC6715	38.71	45.11	O	NGC6717	2.48	33.11	I	NGC6723	4.26	47.80	I
NGC6749	5.05	3.24	D	NGC6752	5.72	20.72	I	NGC6760	5.95	6.19	D
NGC6779	13.46	30.72	O	NGC6809	6.50	36.15	I	NGC6838	7.34	5.82	D
NGC6864	16.06	33.89	O	NGC6934	37.41	20.95	O	NGC6981	21.54	35.97	O
NGC7006	47.26	32.50	O	NGC7078	10.86	25.72	O	NGC7089	18.77	34.91	O
NGC7099	8.76	40.99	O	NGC7492	25.78	45.99	O	Pal1	18.77	13.96	O
Pal10	12.06	4.56	D	Pal11	8.69	23.83	O	Pal12	41.33	42.80	O
Pal13	49.09	42.54	O	Pal14	88.95	35.97	O	Pal15	46.62	44.52	O
Pal2	38.20	8.94	D	Pal3	104.49	43.88	O	Pal4	105.89	43.58	O
Pal5	17.54	42.94	O	Pal6	3.53	27.77	I	Pal8	3.99	20.14	I
Pyxis	73.65	47.40	O	Rup106	32.08	31.98	O	SagittariusII	75.32	41.80	O
Ter1	2.92	2.13	D	Ter10	6.55	32.40	I	Ter12	4.23	17.31	I
Ter2	1.49	18.30	I	Ter3	3.81	26.97	I	Ter4	1.11	28.72	I
Ter5	2.04	7.10	D	Ter6	1.93	8.77	D	Ter7	41.39	45.10	O
Ter8	47.16	45.55	O	Ter9	2.92	7.94	D	Ton2	4.39	24.81	I
UKS1	7.95	4.51	D	VVV-CL001	5.04	7.09	D	Whiting1	52.30	43.09	O